공학박사 학위논문

Optofluidic System for Microlens and Plasmonic Applications

광유체 시스템에 기반한 마이크로 렌즈 및 플라즈모닉 응용

2019년 2월

서울대학교 대학원

재료공학부

이 소 윤

Doctoral Dissertation in Engineering

Optofluidic System for Microlens and Plasmonic Applications

by

So Yun Lee

Advisor: Prof. Jae Ryoun Youn

February 2019

Department of Materials Science and Engineering

Graduate School

Seoul National University

Abstract

Optofluidic System for Microlens and Plasmonic Application

So Yun Lee

Department of Materials Science and Engineering

The Graduate School

Seoul National University

Optofluidics is an interdisciplinary research of optics and microfluidics, which enables flexible optical functions by using microfluidic system or enables manipulation of small amounts of fluids (or sample solution) by using optics. Therefore, on the one hand, deformable fluids make it possible to easily reconfigure the optical system such as microlens, waveguides, etc. by simply replacing the liquid material or deforming the fluid interface. On the other hand, the microfluidic system coupled to optical components can provide beneficial platform for handling and analyzing only small amounts of interesting fluid samples at microscale. In this regard, optofluidics is being rapidly developed in various applications such as optical component construction, biological analysis, energy harvesting, chemical sensing, etc.

In Chapter 2, a tunable optofluidic microlens is demostrated by using a hydrodynamically controllable gas-liquid interface. The relevant physics governing the interface formation are exploited through numerical and theoretical analyses as well. Understanding the physics is important to fabricate the stable multiphasic interface which determines the performance of the lens. We show that non-linear surface tension effect at the gas- liquid interface significantly affects the lens shape

and is dependent on the values of fluid parameters. Since our in-plane microlens is based on the gas-liuquid multiphase, a relatively short focal lenth can be obtained due to the intrinsically large distinction of the refractive indices across the gas-liquid interface. This short focal length would then contribute to realization of more miniatureized optofluidic system for a ‘lab on a chip‘ application.

In chapter 3, an enhanced plasmonic tweezer is suggested by designing and fabricating the metal-dielectric hybrid plasmonic substrate for trapping polystyrene particles or E.coli cells. Localized surface plasmon resonance (LSPR) is an emerging optical phenomenon as a promising tool for near-field energy enhancement. Therefore we utilize the LSPR-induced heating effect for fabricating an efficient microscale trapping system. The synergistic effects of the hybrid plasmonic structure are explored through numerical and experimental analyses. In order to more intensify the LSPR-induced plasmonic effects, we simply introduce the hybrid structure which consists of zinc oxide nanorods (ZnONRs) and gold nanoparticles (AuNPs). We show that ZnONRs transfer the amplified light energy to AuNPs at the interfaces between the ZnONRs and the AuNPs via leaky wave guide modes. Thus, the ZnONRs enhance the LSPR of the AuNPs as well as the trapping performance outstandingly. Our hybrid plasmonic substrate and in-depth analyses would contribute to the construction of an effective optofluidic biological analysis platform through the efficient trapping/manipulation of the fluid-based sample.

In chapter 4, a plasmon-enhanced light harvesting system is developed by introducing a hybrid plasmonic photoelectrode as a photoanode of our bio-photovoltaic system. The solar energy conversion is based on the photosynthesis of cells (Synechocystis sp.) and the photoexcitation, scattering and plasmonic effects of the hybrid plasmonic photoanode (ZnONRs/AuNPs) under the irradiation. The system contains only small amount of cell solution for the current production. Moreover, the plasmonic photoanode enables the efficient light harvesting in broadband of the light source by not only generating electrons itself but also

stimulating the photosynthetic activity of the cells through the LSPR-induced effects. An anomalous power improvement about 17.3-fold can be obtained from the plasmon-enhanced bio-photovoltaic system, compared to the control system of which photoanode is the bare ITO glass. In this respect, our plasmonic photoanode platform would give an inspiration for fabricating an efficient energy harvesting system based on the optofluidic device.

Keywords: Optofluidics, microfluidics, plasmonics, localized surface plasmon resonance, tunable microlens, plasmonic tweezer, plasmonic photoanode, numerical analysis

Student Number: 2014-21429

Contents

List of Figures

List of Tables

Chapter 1.
Introduction

1.1. Optofluidics

Optofluidic system defines a combined system of optics and microfluidics to create versatile application by taking advantages of each area [1]. In that, the optofluidics is a research field where the deformable fluid and microscale chip system are utilized to introduce the reconfigurable optical components such as microlens, waveguide, aperture, etc. or where the small amount of fluid-based sample is manipulated, sensed, analyzed, etc. by the coupled optical components [2]. In a broad sense, the optofluidic system can refer to a simply integrated system with the optical elements and microfluidic system (or microscale fluid sample). The optical element contains optical fibers, lasers, waveguides, plasmonic nanostructure, etc. [3]

Ever since the lab-on-a-chip got attention as an attractive platform for handling and analyzing the biological materials, various potential applications has been developed by using the optofluidic system to achieve the cost-effective and easy operating assays especially in biological fields. For example, biological analysis, bio-sensing, imaging, particle manipulation techniques has been improved by taking advantage of the synergistic combination of optics and microfluidics [3].

Diverse optical elements have been also demonstrated to realize the more functional and compact optofluidic devices [1]. Among them, tunable microlens and plasmonic component are interesting elements due to their abundant potentials for constructing the miniaturized functional systems. Since the optofluidic microlens is based on the fluid-fluid interfaces, the microlens gives certain advantages such as wide tunability of focal length and optically smooth interfaces over the

conventional solid lens [4]. On the other hand, the plasmonic components such as plasmonic substrate, plasmonic nanoparticles, and plasmonic photoelectrode can provide significant improvements of the functional devices for biological analysis, sensing and even for energy harvesting [5].

1.2. Research background

1.2.1. Microfluidics

The microfluidics, one of the main contribution of the optofluidic system, can be defined as a discipline which handles small amount of fluid on the order of microliter or deals with a system of which dimension is microscale [6]. The first applications of microfluidic technologies was used in analysis, since the microfluidic system offers numerous advantages such as requirement of only small quantities of samples and reagents, high resolution and sensitivity of separations and detections, low cost, easy fabrication and short times for analysis [7]. Due to the tremendous benefits of the microfluidic device, diverse miniaturized systems have been developed for biological, chemical, and medical applications as well.

Especially, the fabrication process of the microfluidic chip benefits from soft lithography technique, which is non-photolithographic methods for replicating a pattern [8]. The soft lithography process is simply based on rapid prototyping and replica molding of microfluidic devices in soft material (Fig. 1.2.1). For the soft material, poly(dimethylsiloxane) (PDMS) is a widely used because of its attractive physical, optical, and chemical properties such as elasticity, optical transparency low permeability to water, etc. [9] As a result, the convenient method combined with the soft material facilitates a simple and less expensive fabrication process of the microfluidic chip contrary to the expensive photolithographic methods.

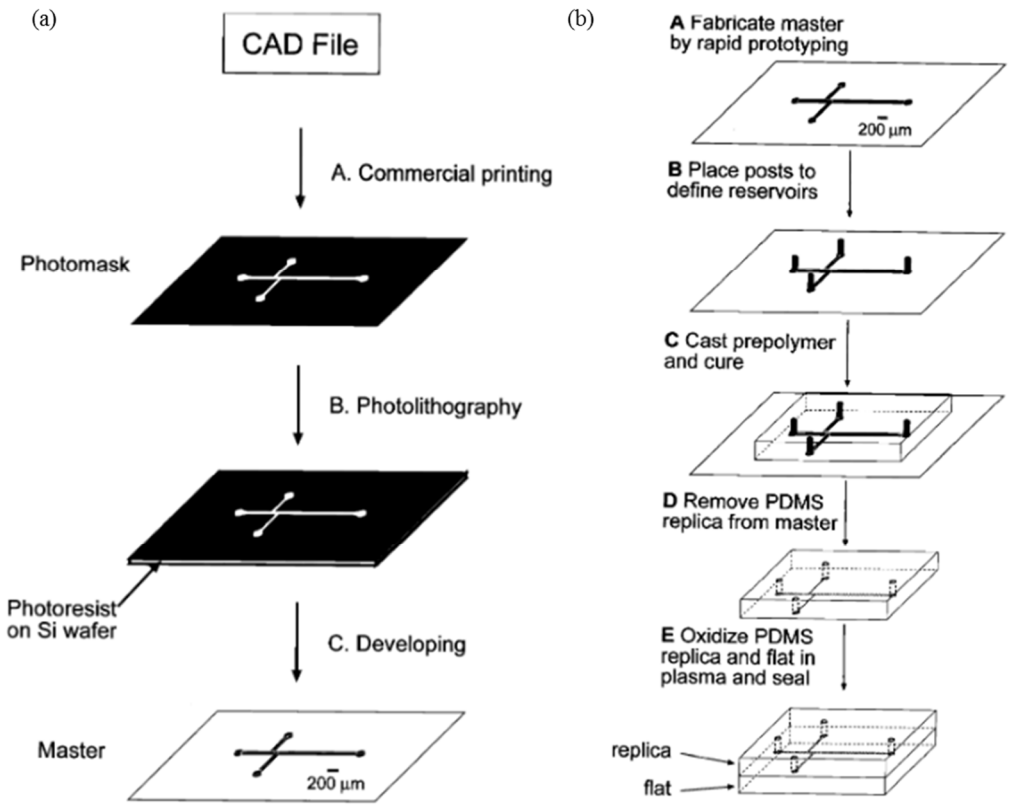

Figure 1.2.1. Schematic illustration of soft lithography process : (a) rapid prototyping for fabricating a master and (b) replica molding of microfludic devices [8].

1.2.2. Plasmonics

Plasmonics is a discipline which takes advantage of the coupling of light to free electrons in metals. When the light resonantly interacts with the conduction electrons at metallic interfaces or in metallic nanostructures, collective oscillations of the electrons occur near the surface of the noble metallic structures [10]. Here, the collective oscillations of the electrons at the surface are referred to surface plasmons (SPs). This SPs results in the strong near-field enhancement near the metallic structure, so the light can be confined in nanoscale space. Therefore, the plasmonic phenomenon allows to break the diffraction limit into subwavelength scale, which is unexpected behavior.

Depending on the metallic structure, two different surface plasmon modes can exist which are distinguished by whether the SPs propagate or are localized as described in Fig. 1.2.2 [11]. For the extended metallic interfaces, the resonant oscillations bring surface plasmon polaritons (SPPs), which are propagating SPs at the metal–dielectric interface. On the other hand, for metal nanoparticles, the resonant oscillations bring localized surface plasmons (LSPs), which are non-propagating SPs and localized near the metal nanostructure surface. The resonance of LSPs mode sensitively depend on the size and shape of the nanostructure [12]. In order to generate SPPs excitation, phase-matching techniques have to be employed by using prism coupling or grating coupling. On the contrary to SPPs, LSPs can be easily excited by direct light illumination. In this sense, the localized surface plasmon resonance (LSPR) is widely used in various fields such as bio-sensing, energy harvesting, light emission, medical diagnosis etc. to enhance the performance in a facile way.

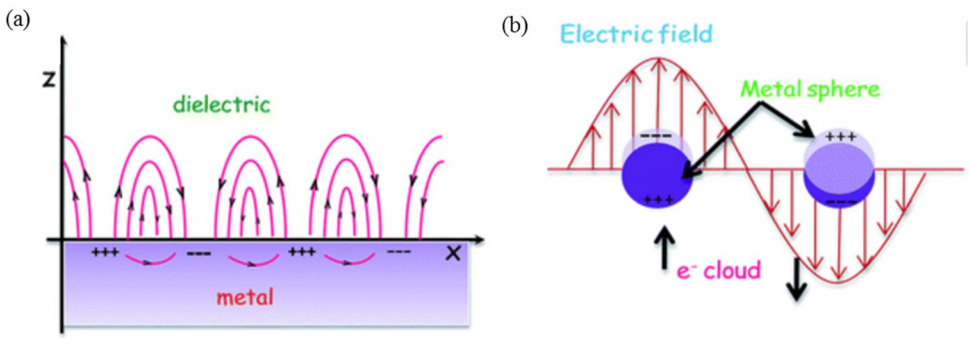

Figure 1.2.2. Schematic illustration of two different surface plasmon resonance modes: (a) Propagating surface plasmons and (b) localized surface plasmons [11].

1.2.3. Localized surface plasmon resonance (LSPR)

LSPR is the localized resonant oscillation of plasmon arose from a strong coupling between light and the abundant free electrons in the metal nanoparticle as described in Fig. 1.2.3(a) [13]. The localized resonant oscillation driven by the incident electromagnetic field (light) with frequency (ω) and amplitude ($\vec{E}$) brings periodic charge separation in metal nanoparticle and consequently arises an induced dipole superposed on it. The resulting dipole ($\vec{p}$) is defined as following equation,

$$\vec{p} = \varepsilon_m \alpha \vec{E} \tag{1-1}$$

$$\alpha = 4\pi\varepsilon_0 a^3 \frac{\varepsilon(\omega) - \varepsilon_m}{\varepsilon(\omega) + 2\varepsilon_m} \tag{1-2}$$

where ε_m is the permittivity of the surrounding medium, α is the polarizability of the metal nanoparticle (according to the Drude model), ε_0 and $\varepsilon(\omega)$ are permittivity of vacuum and metal, respectively and a is radius of the metal nanoparticle. Then the enhanced local field ($\vec{E}_{out}$) in the vicinity of the nanoparticle can be explained by following equation,

$$\vec{E}_{out} = \vec{E} + \frac{3\hat{n}(\hat{n}\cdot\hat{p}) - \hat{p}}{4\pi\varepsilon_0\varepsilon_m}\frac{1}{r^3} \tag{1-3}$$

where r is the distance away from the nanoparticle center. The second term on the right side of the equation (1-3) indicates the induced electric field through the resonant oscillation.

This localized phenomenon has a great potential due to its characteristic decay mechanisms which include near-field enhancement, far-field scattering, hot-electron injection (or plasmonic induced charge separation, PICS), plasmon-induced resonant energy transfer and plasmonic heating (Fig. 1.2.3(b)) [14-16]. The excited LSPs can be decayed in radiative ways or non-radiative ways. Radiative

decay includes near-field enhancement and far-field scattering whereas non-radiative decay includes hot-electron generation, plasmon-induced resonant energy transfer and plasmonic heating. Especially, when the metal nanostructures are in contact with semiconductor, the generated energetic hot-electrons can be transferred to the conduction band of the semiconductor.

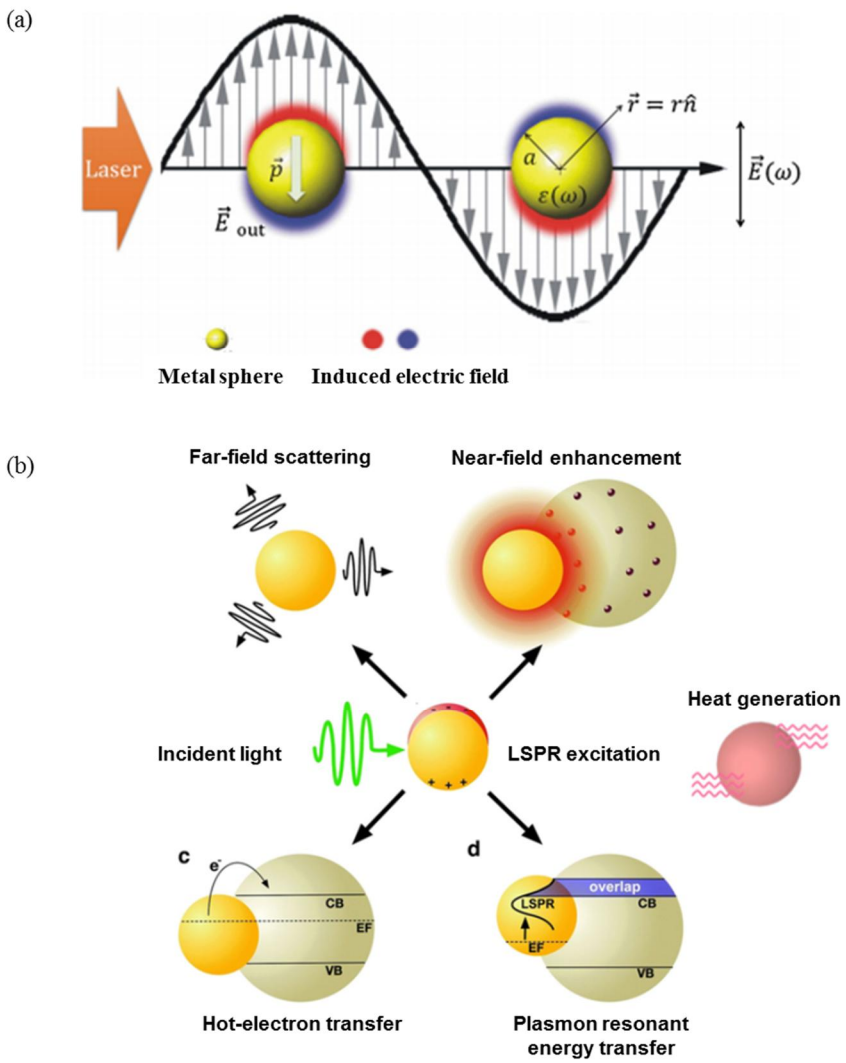

Figure 1.2.3. Schematic illustration of (a) localized surface plasmon resonance [13] and (b) different LSPR decay mechanisms [14,16].

1.3. Objectives of present work

In the dissertation, three specific applications of optofluidics will be introduced. All the works are aimed to suggest potential platforms for realizing efficient optofluidic systems, by taking advantages of small amount of fluids or plasmonic phenomena arose from ZnONRs/AuNPs hybrid plasmonic nanostructure. Furthermore, numerical analyses are performed in each research for designing, improving, or analyzing the suggested optofluidic device. Then the results of numerical prediction and analyses are verified by comparing with the experimentally obtained results.

In chapter 2, the tunable multiphase microlens is demonstrated by utilizing gas-liquid interface and hydrodynamic mechanism. Here, a problem associating to asymmetric microlens shape is investigated by conducting two-phase flow simulation based on the phase-field physics.

In chapter 3, LSPR-induced effects such as near-field enhancement, plasmonic heating, heat-induced natural convection are predicted for two different plasmonic nanostructures (ZnONRs/AuNPs and bare AuNPs) in order to design the enhanced plasmonic tweezer. The simulation was based on the multiscale modeling for solving different physics relating to electromagnetic field, temperature field, and velocity field. Moreover, the synergistic effects of the hybrid plasmonic nanostructure is verified through the simulation results.

In chapter 4, far-field scattering effects, which is one of the LSPR-induced effects, are predicted to design the plasmonically enhanced energy harvesting system. The scattering effects are investigated with respect to various control factors including nanostructure geometry, AuNPs size, and light source direction for the efficient energy conversion.

1.4. References

1 Monat, C., Domachuk, P. & Eggleton, B. Integrated optofluidics: A new river of light. *Nature photonics* **1**, 106 (2007).

2 Song, C. & Tan, S. H. A Perspective on the Rise of Optofluidics and the Future. *Micromachines* **8**, 152 (2017).

3 Erickson, D., Sinton, D. & Psaltis, D. Optofluidics for energy applications. *Nature Photonics* **5**, 583 (2011).

4 Lee, S., Wee, D., Youn, J. & Song, Y. Manipulation and analysis of an optofluidic multiphase microlens. *RSC Advances* **7**, 35827-35831 (2017).

5 Bragheri, F., Osellame, R. & Ramponi, R. Optofluidics for biophotonic applications. *IEEE Photonics Journal* **4**, 596-600 (2012).

6 Yang, Z., Matsumoto, S., Goto, H., Matsumoto, M. & Maeda, R. Ultrasonic micromixer for microfluidic systems. *Sensors and Actuators A: Physical* **93**, 266-272 (2001).

7 Whitesides, G. M. The origins and the future of microfluidics. *Nature* **442**, 368 (2006).

8 McDonald, J. C. *et al.* Fabrication of microfluidic systems in poly (dimethylsiloxane). *ELECTROPHORESIS: An International Journal* **21**, 27-40 (2000).

9 Ng, J. M., Gitlin, I., Stroock, A. D. & Whitesides, G. M. Components for integrated poly (dimethylsiloxane) microfluidic systems. *Electrophoresis* **23**, 3461-3473 (2002).

10 Maier, S. A. *Plasmonics: fundamentals and applications*. (Springer Science & Business Media, 2007).

11 Jana, J., Ganguly, M. & Pal, T. Enlightening surface plasmon resonance effect of metal nanoparticles for practical spectroscopic application. *RSC Advances* **6**, 86174-86211 (2016).

12 Kauranen, M. & Zayats, A. V. Nonlinear plasmonics. *nature photonics* **6**,

737 (2012).

13 Chen, X.-J., Cabello, G., Wu, D.-Y. & Tian, Z.-Q. Surface-enhanced Raman spectroscopy toward application in plasmonic photocatalysis on metal nanostructures. *Journal of Photochemistry and Photobiology C: Photochemistry Reviews* **21**, 54-80 (2014).

14 Zhang, N., Han, C., Fu, X. & Xu, Y.-J. Function-Oriented Engineering of Metal-Based Nanohybrids for Photoredox Catalysis: Exerting Plasmonic Effect and Beyond. *Chem* (2018).

15 Cushing, S. K. & Wu, N. Plasmon-enhanced solar energy harvesting. *The Electrochemical Society Interface* **22**, 63-67 (2013).

16 Ghobadi, T. G. U., Ghobadi, A., Ozbay, E. & Karadas, F. Strategies for Plasmonic Hot-Electron-Driven Photoelectrochemical Water Splitting. *ChemPhotoChem* **2**, 161-182 (2018).

Chapter 2.

Tunable Multiphase Microlens

2.1. Introduction

Optofluidic microlens has emerged as a promising optical component due to its advantages over the solid microlens, e.g., wide tunable range and optically smooth interfaces by means of the hydrodynamic tuning mechanism, the ease in changing optical properties with different lens materials, and the simple fabrication and integration of the device. Recently, a few studies have demonstrated the tunable optofluidic microlens using liquid-liquid [1-5] or gas-liquid interfaces [6,7]. They have shown considerable performance in experiments and carried out fluid simulation to analyze the lens shape according to the microchannel geometry or flow conditions. For instance, Seow et al. simulated the stream flow with different aspect ratios of the expansion chamber to obtain an optimum design of the chamber for a stable lens interface [3]. Rosenauer et al. predicted the lens shape with symmetric and asymmetric expansion chambers at different flow rate conditions to verify that the fabricated chamber achieved the symmetric lens shape [4]. However, theoretical studies of the optofluidic microlens generated by the interface formation under the multiphase flow are still limited.

In this letter, a tunable optofluidic microlens that utilizes the gas-liquid flow in a symmetric expansion chamber is reported. The characteristics of the lens are analyzed by controlling the inlet pressures of the liquid flow and gas flow. Moreover, numerical and theoretical analyses are conducted to figure out the formation mechanism of asymmetric and symmetric lens surfaces and relevant physics governing the interface formation. For the theoretical model, the Stokes-Cahn-Hilliard equation is non-dimensionalized, and material and operational parameters, such as the average flow rate , dynamic viscosity , density , surface tension coefficient , and characteristic length , are

analyzed based on the theoretical evaluation. In addition, the lens characteristics such as the lens curvature, thickness, and focal length in the microfluidic device are examined by performing optical observation and ray-tracing simulation. The schematic geometry and dimensions of the optofluidic chip is described in Fig. 2.1.1 and the configuration of the optofluidic device and the experimental set-up are shown in Fig. 2.1.2 and Fig. 2.1.3, respectively.

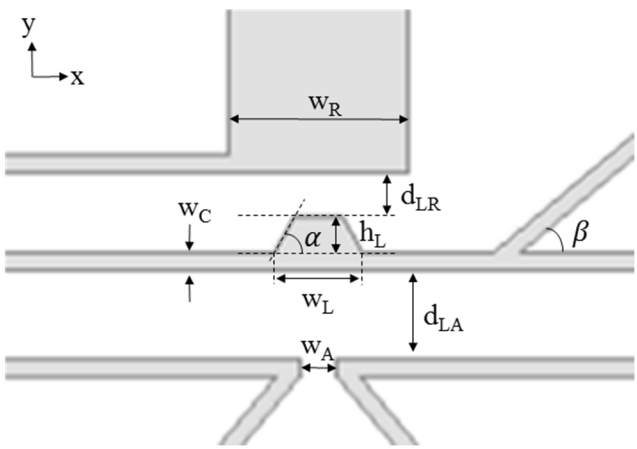

Fig. 2.1.1 Schematic geometry and dimensions of the optofluidic chip used for experiment and simulation. The inclination angle of the chamber wall (α) is 60°, the angle between the main channel and the sub-channel (β) is 40°, the angle channel width (w_C) is 200 μm, the width of the expansion chamber (w_L) and the aperture (w_A) are 1000 μm and 400 μm respectively, the height of the expansion chamber (h_L) is 400 μm, d_{LA} is 1000 μm, d_{LR} is 500 μm.

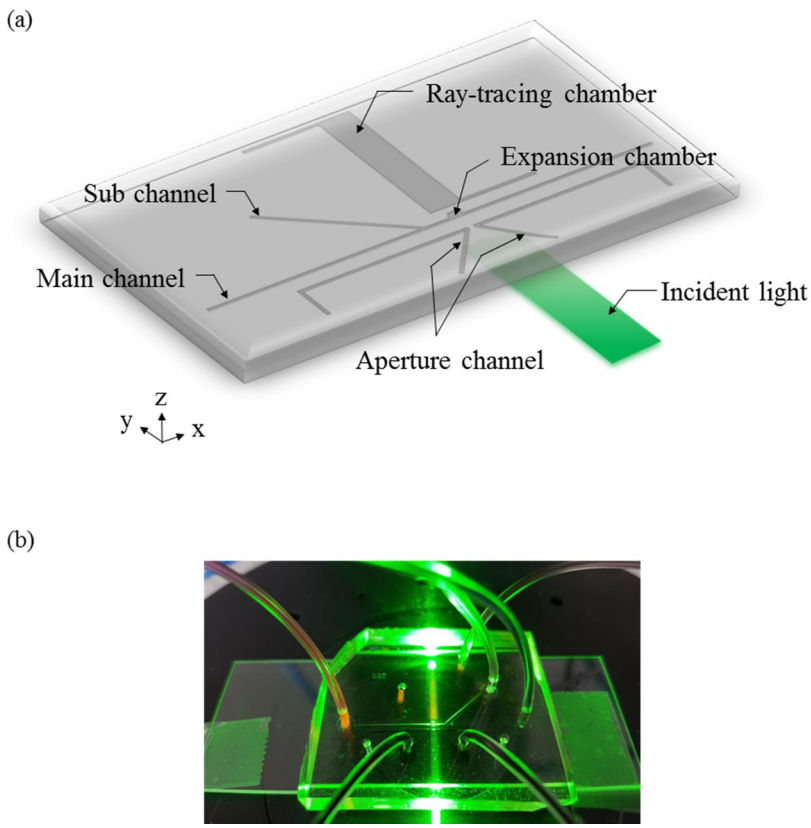

Fig. 2.1.2 Schematic configuration and real image of the optofluidic device.

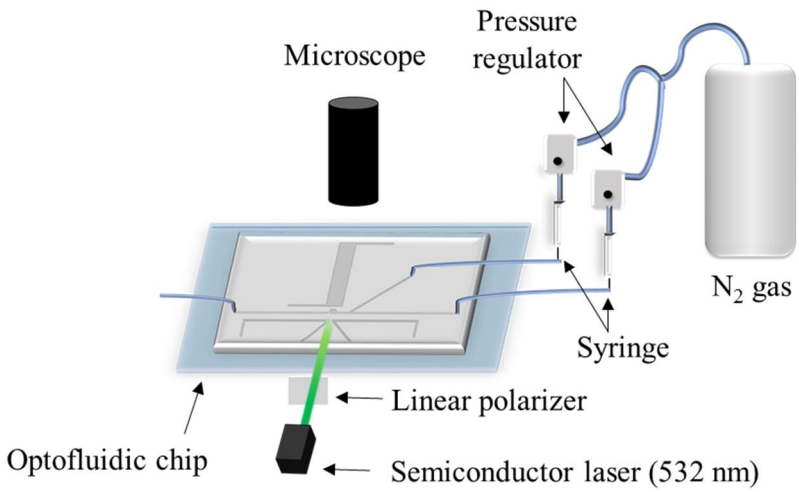

Fig. 2.1.3 Schematic configuration of the experimental set-up for optical observation.

2.2. Experimental section

2.2.1. Design and fabrication of the optofluidic chip

An optofluidic device was fabricated using a soft-lithography process with polydimethyl-siloxane (PDMS, Sylgard 184, Dow Corning, Midland, U.S.A.). A detailed process of fabricating a master is explained elsewhere [5], and a cured PDMS replica from the master was attached to the glass substrate by corona treatment. The device consisted of a flow channel, aperture channels, and a ray-tracing chamber. The flow channel was composed of a main channel, sub-channel, and symmetric expansion chamber as shown in Fig. 2.1.2.

2.2.2. Materials

The aperture channels were filled with black ink, and a fluorescent dye solution, 3 μmol L^{-1} of rhodamine B (Sigma-Aldrich) dissolved in ethylene glycol, was used for the ray-tracing chamber to observe the ray-path. In the experiments, isopropyl alcohol (IPA) and nitrogen gas (N_2) were injected through the main channel and sub-channel, respectively, to form the symmetric microlens in the expansion chamber. Two other liquids, benzyl alcohol (BA) and ethylene glycol (EG), were also tested as the main fluid to find a proper lens material, but both liquids showed an asymmetric lens shape. The material properties are listed in Table 2.2.1.

Table 2.2.1. Material properties of N2, IPA, BA, EG, and PDMS.

Property / Material	Dynamic viscosity $(\mu, \times 10^{-3}\ \mathrm{Pa \cdot s})$	Density $(\rho, \mathrm{kg/m^2})$	Surface tension $(\sigma, \mathrm{mN/m})$	Refractive index (n)
N_2	0.01747	1.2754	-	1.0003
IPA	1.96	786	23	1.3776
BA	5.474	1044	39	1.5396
EG	16.2	1110	47	1.43
PDMS	-	-	-	1.4

2.2.3. Experimental set-up

The inlet pressure of the main fluids (P_{main}) was varied from 20 kPa to 26 kPa, whereas that of the sub-fluid (P_{sub}) was fixed at 20 kPa using a digital pressure regulator (DPG8001-60, OMEGA, Stamford, U.S.A.). The light source was a semiconductor laser (PGL-FS-532, CNI Optoelectronics Technology CO., Ltd, Jilin, China) with a 532 nm wavelength, and a dichroic linear polarizer was employed for polarization of the light. The lens interface and ray-path were observed using optical microscopy [5].

2.3. Numerical analysis

Two-dimensional numerical simulation of the two phase flow is conducted for the numerical modeling of the gas-liquid interface of the lens. The coupled Navier-Stokes-Cahn-Hilliard equations are solved using COMSOL Multiphysics® [4,8-11]. The two phases are separated by a diffuse interface, and the interface position is tracked by solving two additional transport equations for the phase field. The fluids are assumed to be incompressible. The inertia and gravity effects are neglected for the fluid flow in the microchannel. The surface tension at the gas-liquid interface is considered in the momentum equation as shown below,

$$0 = \nabla \cdot \left[-p\mathbf{I} + \mu(\nabla \mathbf{u} + (\nabla \mathbf{u})^T \right] + \mathbf{F}_{st} \tag{2-2}$$

$$\mathbf{F}_{st} = G\nabla\phi \tag{2-3}$$

$$G = \lambda\left[-\nabla^2\phi + \frac{\phi(\phi^2 - 1)}{\varepsilon^2} \right] \tag{2-4}$$

$$\lambda = \frac{3\varepsilon\sigma}{\sqrt{8}} \tag{2-5}$$

$$\frac{\partial\phi}{\partial t} + \mathbf{u} \cdot \nabla\phi = \nabla \cdot \frac{\gamma\lambda}{\varepsilon^2}\nabla\psi \tag{2-6}$$

$$\psi = -\nabla \cdot \varepsilon^2\nabla\phi + \left(\phi^2 - 1\right)\phi \tag{2-7}$$

where $\mathbf{F}_{st}$ is the surface tension force, ∇ is the del operator, p is the pressure, $\mathbf{I}$ is the identity tensor, μ is the dynamic viscosity, $\mathbf{u}$ is the flow velocity, ϕ is the dimensionless phase field variable, ψ is the phase field help variable, λ is the mixing energy density, and ε is the interface thickness parameter. The Stokes equation is coupled with the convective Cahn-Hilliard equation. The convective Cahn-Hilliard equations track a diffuse interface, which is defined as the region where the phase field ϕ is varied from -1 to 1. The dynamic viscosity is determined by the calculated ϕ .

2.4. Theoretical analysis

Theoretical analysis is carried out to provide in-depth understanding of the multiphasic microlens formation. The Stokes equation and the convective Cahn-Hilliard equation are nonlinear due to the surface tension force term $\mathbf{F}_{st}$ and the inertia term $\mathbf{u}\cdot\nabla\phi$ respectively. The characteristics of the microlens is determined by the combination of the non-linear equations (2-1) and (2-5). Since the value of ϕ of the convective Cahn-Hilliard equation interactively changes the surface tension force of the Stokes equation, the microlens formation is affected. Basically, the shape and position of the lens interface are determined from the hydrodynamic force balance of fluid. In this regard, the Stokes equation, equation (2-1), is non-dimensionalized using the dimensionless differential operator and variables: $\nabla^* = L\nabla$, $p^* = (p - p_\infty)/(p_0 - p_\infty)$, and $\mathbf{u}^* = \mathbf{u}/u_{avg}$.

$$0 = -\frac{p_0 - p_\infty}{L}\nabla^* p^* + \frac{\mu u_{avg}}{L^2}\nabla^{*2}\mathbf{u}^* + \frac{3L\sigma}{\sqrt{8}}\left[-\frac{1}{L^2}\nabla^{*2}\phi + \frac{\phi(\phi^2 - 1)}{L^2}\right]\frac{1}{L}\nabla^*\phi \tag{2-7}$$

where L is the characteristic length, $p_0 - p_\infty$ is the reference pressure difference and u_{avg} is the average flow velocity. Equation (2-7) still has a dimension of $mL^{-2}t^{-2}$, where m, L and t represent the mass, length, and time, respectively. Therefore, the equation is multiplied by $L\rho^{-1}u_{avg}{}^{-2}$, and ρ was replaced with μ/v.

$$0 = -\frac{p_0 - p_\infty}{\rho u_{avg}{}^2}\nabla^* p^* + \frac{\mu}{\rho u_{avg} L}\nabla^{*2}\mathbf{u}^* + \frac{3}{\sqrt{8}}\frac{\sigma}{\mu u_{avg}}\frac{\mu}{\rho u_{avg} L}\left[-\nabla^{*2}\phi + \phi(\phi^2 - 1)\right]\nabla^*\phi \tag{2-8}$$

The final non-dimensionalized equation is as follows.

$$0 = -[\mathrm{Eu}]\nabla^* p^* + \left[\frac{1}{\mathrm{Re}}\right]\nabla^{*2}\mathbf{u}^* + \frac{3}{\sqrt{8}}\left[\frac{1}{\mathrm{Ca}}\right]\left[\frac{1}{\mathrm{Re}}\right]\left[-\nabla^{*2}\phi + \phi(\phi^2 - 1)\right]\nabla^*\phi \tag{2-9}$$

where the dimensionless numbers, the Euler number (Eu), Reynolds number (Re), and

capillary number (Ca), are expressed as $\mathrm{Eu} = (p_0 - p_\infty) / \rho u_{avg}^{\ 2}$, $\mathrm{Re} = \rho u_{avg} L / \mu$, and $\mathrm{Ca} = \mu u_{avg} / \sigma$, respectively. As mentioned above, the last term of equation (2-9) offers the nonlinearity of the Stokes equation. Thus, the nonlinear phenomena of multiphase fluid, such as asymmetry and singularity, rely upon Ca and Re. This implies that the resulting nonlinearity decreases as product of Ca and Re increases. It is, therefore, expected that a liquid with a high product value of Ca and Re would generate a symmetric microlens interface in the symmetric expansion chamber.

2.5. Results and discussion

2.5.1. Lens shape

The lens shape was examined experimentally and numerically for three different liquids as shown in Fig. 2.5.1 and Fig. 2.5.2, respectively. The main stream and sub-stream flowed in the left-hand direction. It was found that the experimental and numerical results were in good agreement for the three liquids. The interface between the streams of N_2 and IPA was nearly symmetric but the interfaces between the streams of N_2 and BA, and of N_2 and EG were asymmetric. The asymmetry of the interface also increased in the order of IPA, BA, and EG at all the pressure levels. The lens thickness increased as the pressure applied to the main fluid increased. Generation of the symmetric lens is of great importance to secure a high performance. Furthermore, it is essential to fabricate a microlens with a longitudinally tunable focal length. For these reasons, IPA was selected in this study as the main liquid to form the symmetric microlens.

2.5.2. Non-linear surface tension effect on the lens shape

To understand the lens formation in a more systematic manner, the asymmetry of lens was evaluated using the dimensionless numbers presented above. Ca and Re values were calculated from the experimental conditions for the three liquids at each pressure level. It was inferred that the product value of Ca and Re significantly affected the shape formation of the lens. Fig. 2.5.3(a) shows the measured average velocities used for the calculation. The dimensionless numbers, Ca and Re, were found quite small at all the pressure levels as presented in Fig. 2.5.3(b) and (c). The small values of Re ($Re \ll 1$) indicate the laminar flow in the microchannel (Fig. 2.5.3(b)), and the small values of Ca ($Ca \ll 1$) for all the liquids imply that the surface tension effect is dominant over the viscous effect at the gas-liquid interface (Fig. 2.5.3(c)) [12]. The results of $Ca \cdot Re$ are plotted in Fig. 2.5.3(d). It was shown that IPA offered the most symmetric lens shape with the largest value of $Ca \cdot Re$ in all the pressure levels, which could explain the lens shape obtained both experimentally and numerically. In short, as the product value of Ca and Re

increases, the interface becomes more symmetric. This quantitative analysis revealed that the Ca·Re, i.e., $\rho u_{avg}{}^2 L/\sigma$ acts as a key factor for determining the shape of microlens in the microfluidic device. Since the Ca·Re depends on the dynamic viscosity and u_{avg} is a function of the viscosity, the shape formation of the lens is affected by the fluid parameters, such as the density, dynamic viscosity, and surface tension of the main fluid as well as the imposed pressure. To the best of our knowledge, this is the first report to explore the shape formation of optofluidic microlens in the microfluidic channel by considering quantitative theoretical and numerical evaluation.

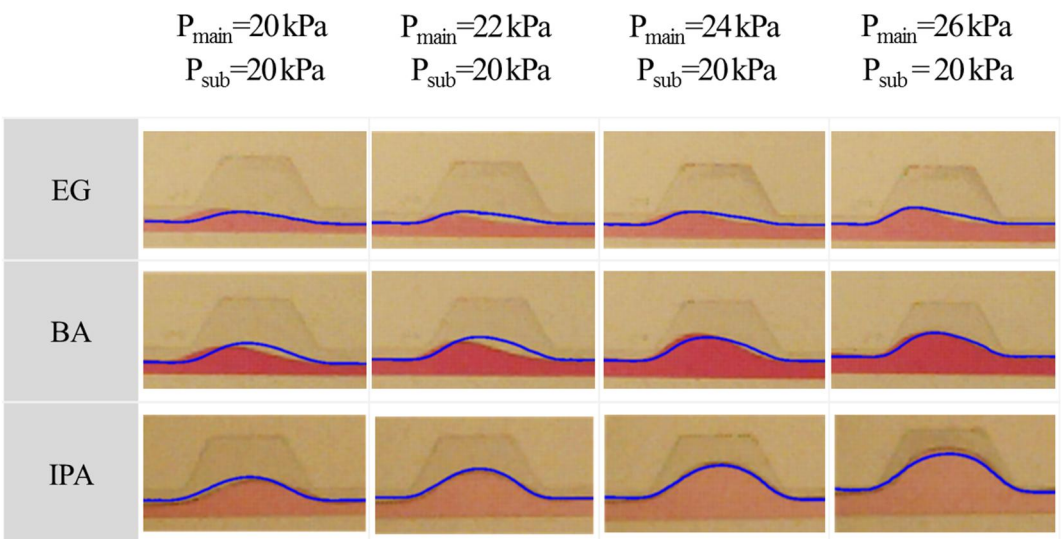

Fig. 2.5.1. Microscopic images of the gas-liquid interfaces for three liquids at different pressures. The simulated interfaces (blue curves) are superposed onto the experimental microscopic images for comparison.

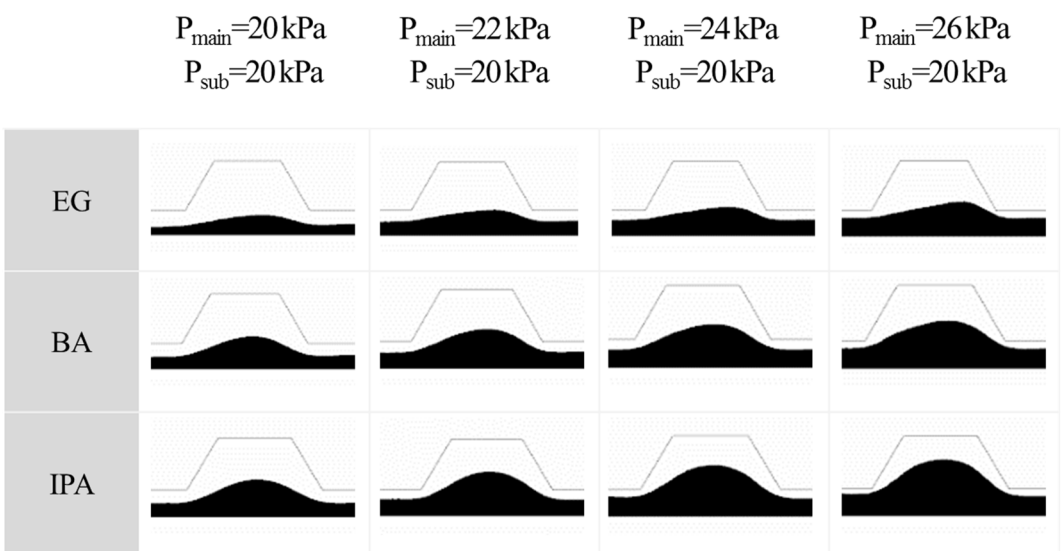

Fig. 2.5.2. Simulation results of the gas-liquid interfaces for three liquids at different pressures.

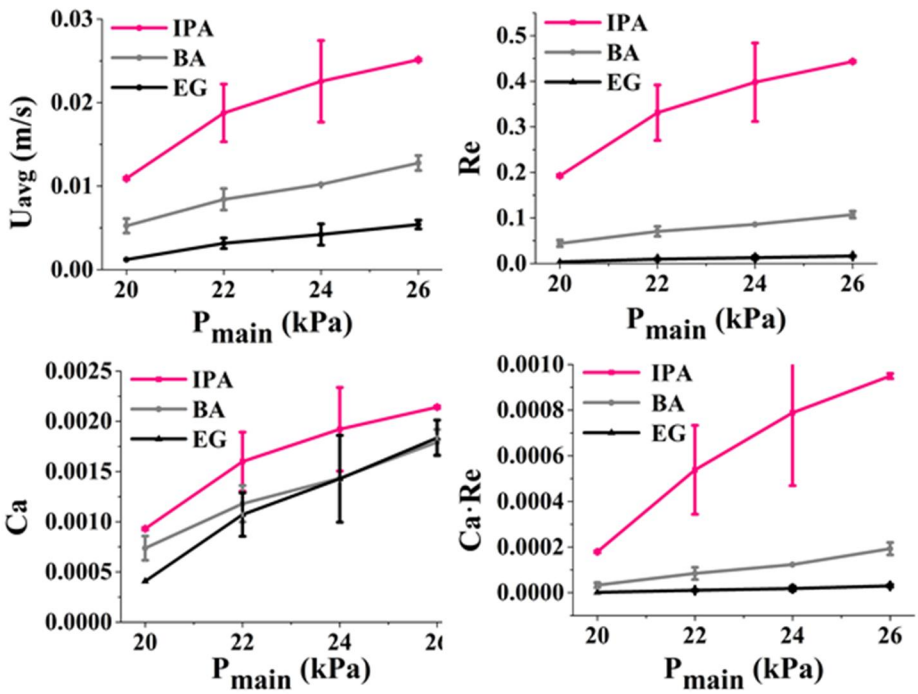

Fig. 2.5.3 (a) Measured average velocities, (b) Reynolds numbers, (c) capillary numbers, and (d) product values of capillary numbers and Reynolds numbers for three liquids with respect to pressures.

2.5.3. Characteristics of the tunable microlens

The hydrodynamic microlens formed by the streams of N_2 and IPA was characterized through optical evaluation. The tunability of the lens was analyzed using the ray-path in fluorescence images in the expanded range of the inlet pressure from 16 kPa to 26 kPa to see the available pressure range, as presented in Fig. 2.5.4. The focal length (f) was defined as the distance between the flat bottom line of the expansion chamber and the focal point. The focal length decreases with increasing P_{main} until P_{main} becomes 24 kPa. Therefore, it turns out that the proper pressure range for the focus tuning is between 16 kPa and 24 kPa. Fig. 2.5.5(a) shows the gray-scaled images of the unfocused beam and focused beam, and Fig. 2.5.5(b) presents the light intensity profiles at the positions indicated in the gray-scaled images. The light intensity is zero outside of the positions from -0.2 mm to 0.2 mm for the unfocused beam (A, B), which indicates that the apertures completely block the incident light.

The enhancement factor, defined as the ratio of the peak intensity of a focused beam (B′) to the intensity of an unfocused beam (B), is measured to be 4.07 [2]. The characteristics of the optofluidic lens obtained from the experimental and numerical results are illustrated in Fig. 2.5.6. The curvature (1/R) and the lens thickness (t) were determined by fitting a circle to the gas-liquid interface acquired from the experiment and simulation. The curvature has a maximum value at P_{main}=24 kPa, and then declines as the pressure increases because the lens interface approaches the wall of the expansion chamber at above 24 kPa (Fig. 2.5.7 and Fig. 2.5.8) [2,5]. The experimental results showed that the tunable focal length between 1.60 mm and 3.15 mm could be manipulated in the microfluidic device fabricated in this study, as presented in Fig. 2.5.6(c). A ray-tracing code was developed based on MATLAB®, and the curvature and lens thickness obtained from the simulation results were employed to predict the focal length numerically (Fig. 2.5.9). The overall trends of the experimental and simulation results were similar, but a slight discrepancy was observed in the case of the focal length at lower inlet pressure because aspherical microlens shape was obtained in the experiment unlike the spherical shape calculated in the simulation. The aspherical microlens leads to decrease in the refraction of light and then increase in the focal length (Fig. 2.5.7 - Fig. 2.5.10).

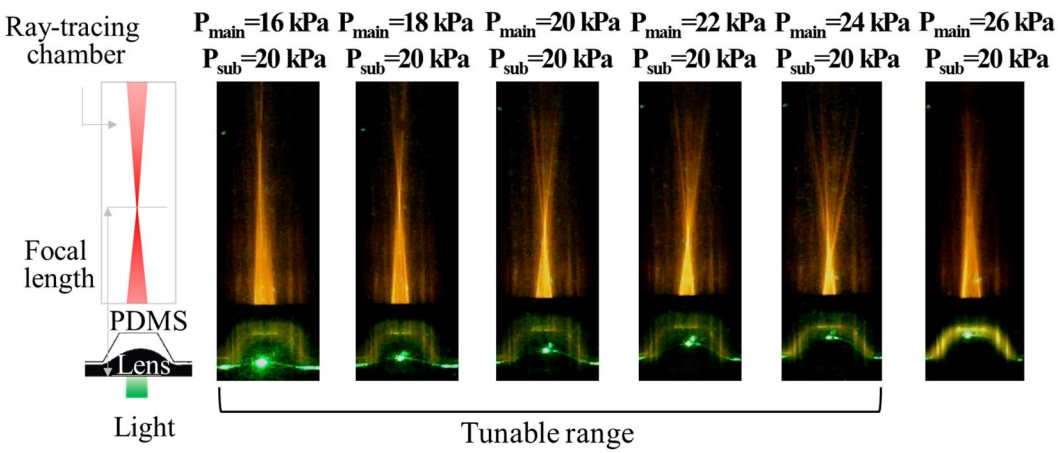

Fig. 2.5.4. Schematic illustration of the ray-path observation and fluorescence images of the ray paths at different pressures.

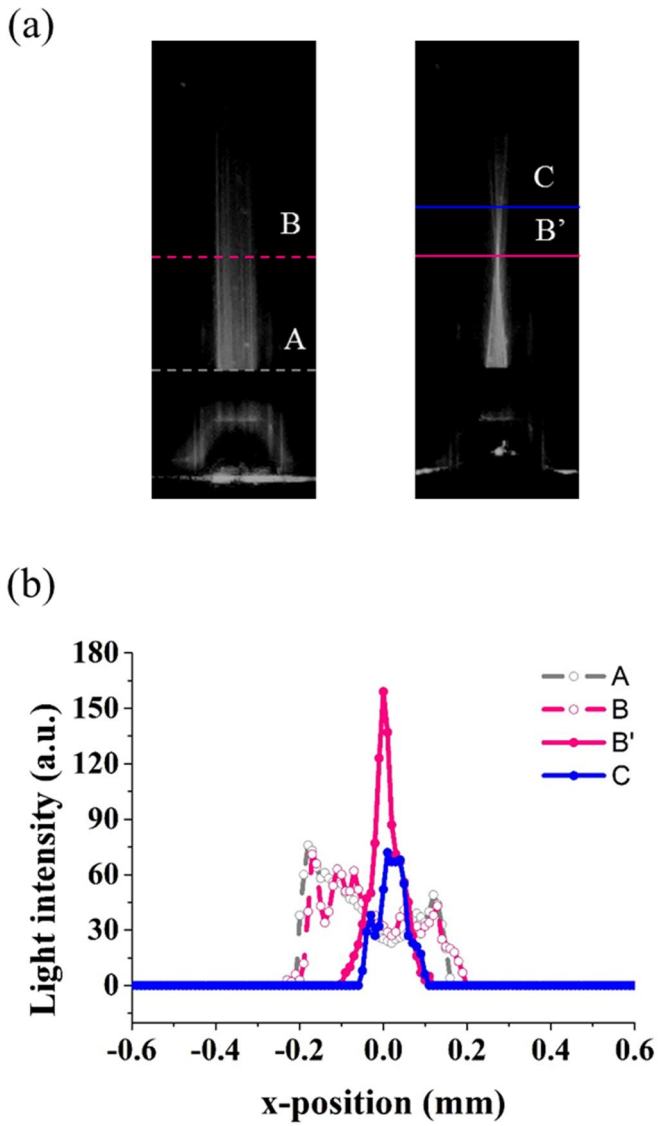

Fig. 2.5.5. Characterization of light intensity profile**.** (a) Gray-scaled images of ray paths. The pressures applied for the main stream and sub-stream were all 20 kPa for the focused beam. The dashed and solid lines indicate the positions where light intensity profiles were evaluated. (b) Light intensity profiles evaluated along the lines. The dashed lines (A and B) and solid lines (B' and C) indicate the light intensity profile for unfocused beam and focused beam, respectively.

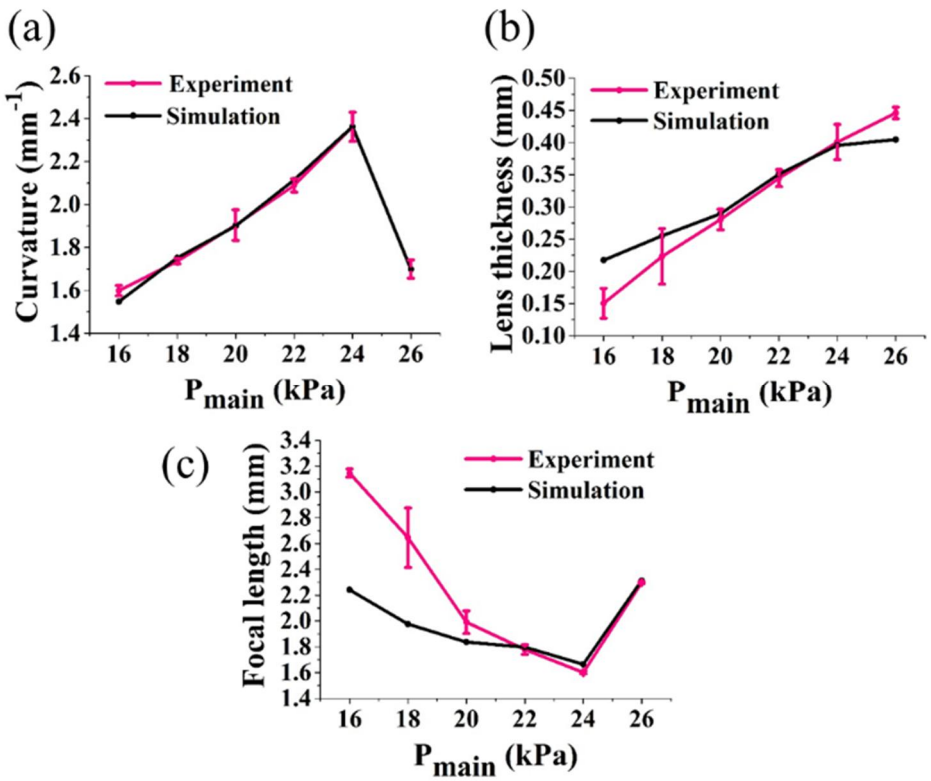

Fig. 2.5.6. Comparison of the lens characteristics obtained from simulation and experimental results: (a) curvatures, (b) lens thickness, and (c) focal lengths as a function of the pressure of mainstream.

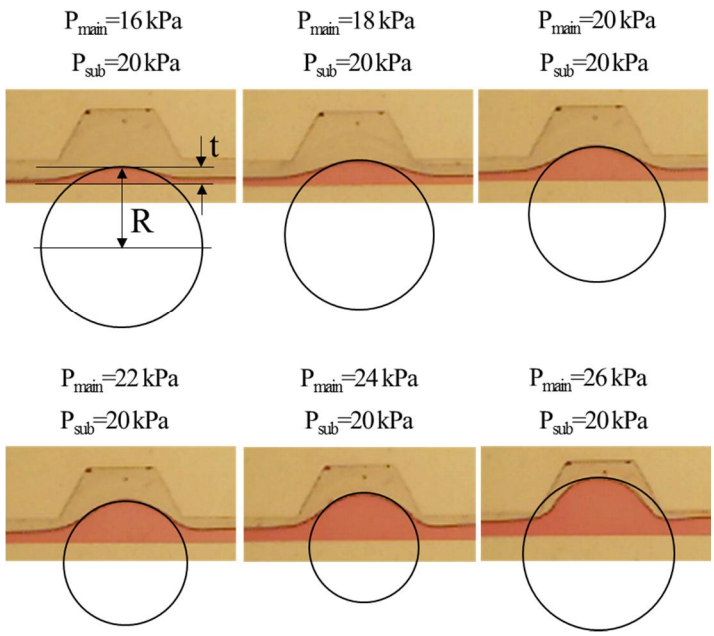

Fig. 2.5.7. Fitting of circles to the microlens interface obtained from experiment. Definitions of the radius of curvature (R) and the lens thickness (t) are also illustrated.

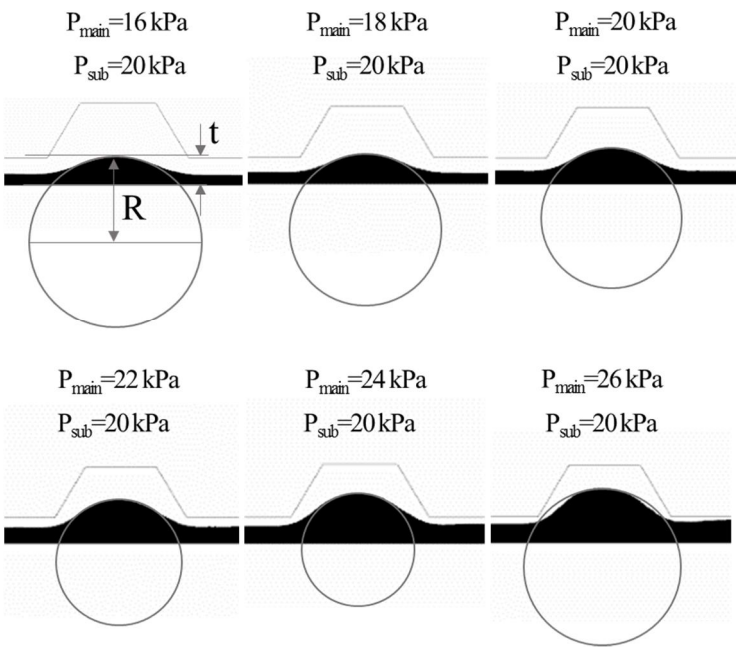

Fig. 2.5.8. Fitting of circles to the microlens interface obtained from simulation. The curvature has a maximum value when P_{main} is 24 kPa for both experimental and simulation results. Since the experimentally obtained lens surface is aspherical, the circles are primarily fitted to the apex of the lens. On the other hand, the numerically obtained lens surface is spherical in the region, and thus the circles fit well to the lens surface. The tendency of aspherical shape becomes strong, especially at low inlet pressure. Therefore, relatively large discrepancies are found in the pressure conditions.

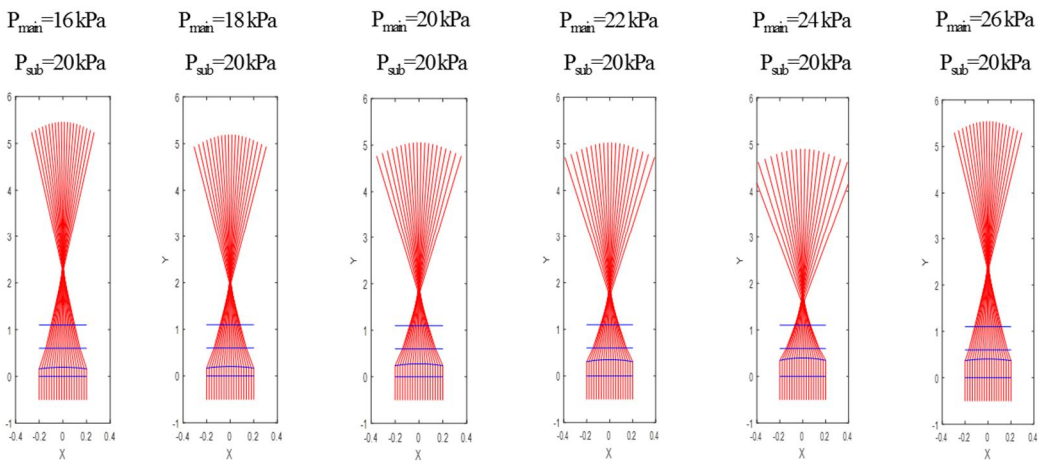

Fig. 2.5.9. Predicted ray-path at different pressure values. The first, second, third, and fourth blue lines from bottom to top indicate the bottom of the microlens, the surface of the microlens, the interface between the expansion chamber and PDMS, and the interface between PDMS and the ray-tracing chamber, respectively.

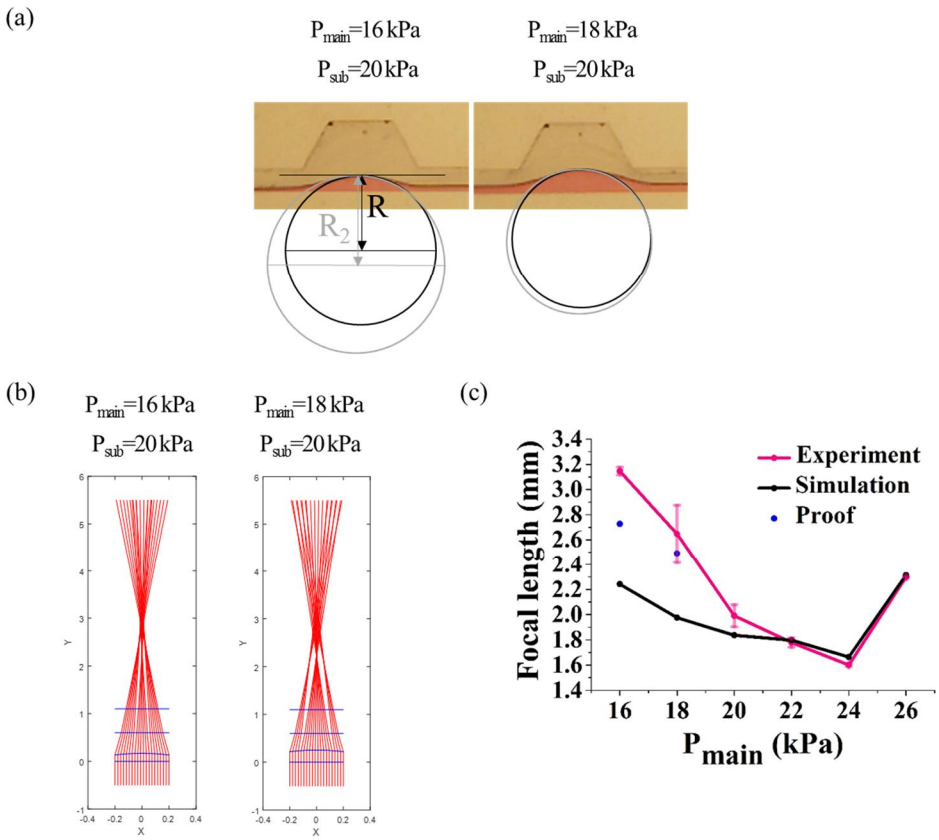

Fig. 2.5.10 Evidence for the aspherical microlens effect on the discrepancy in the case of the focal length between the experimental and simulation results. (a) Fitting of circles to the microlens interface obtained from experiment. Additional circles which have different curvature ($1/R_2$) from that of the original fitting circle (R) are added to show that the interface is aspherical. (b) Predicted ray-path from the fitting circles of Fig. 2.5.7(a) (one original and two additional circles) at each pressure value. The discontinuity in the ray-path is due to the non-smooth lens interface at the junction of the fitting circles. (c) Focal lengths as a function of the pressure of mainstream. The focal lengths predicted from Fig. 2.5.7(b) are plotted with blue dot marker, which are closer to the experimental results. This result proves that the discrepancy observed at lower inlet pressure was due to the aspherical microlens shape.

2.6. Summary

In the current study, various shapes of the microlens based on the gas-liquid interface were investigated from the experimental and numerical results, and the lens formation in the microfluidic device was analyzed by a theoretical model. The Stokes-Cahn-Hilliard equation is non-dimensionalized, and the effect of liquid properties on the lens shape was evaluated. The non-linearity of the surface tension needs to be considered for manipulating the gas-liquid flow in a controlled way in that the non-linear surface tension effect becomes dominant at the gas-liquid interface, especially in microfluidics (or optofluidics) [13]. Our theoretical analysis demonstrated that the interface shape of the lens was determined by the fluid properties as well as the inlet pressure applied to the microfluidic device. In addition, the microlens based on the gas-liquid interface has an advantage of a relatively short focal length due to the large distinction of the refractive indices across the interface, which is critical for the real application in optofluidics [14,15]. It is expected that this study will provide a way for manipulating the multiphasic microlens based on the comprehensive understanding on the lens formation within the microfluidic device.

2.7. References

1 Mao, X., Waldeisen, J. R., Juluri, B. K. & Huang, T. J. Hydrodynamically tunable optofluidic cylindrical microlens. *Lab on a Chip* **7**, 1303-1308 (2007).

2 Tang, S. K., Stan, C. A. & Whitesides, G. M. Dynamically reconfigurable liquid-core liquid-cladding lens in a microfluidic channel. *Lab on a Chip* **8**, 395-401 (2008).

3 Seow, Y. *et al.* Different curvatures of tunable liquid microlens via the control of laminar flow rate. *Applied Physics Letters* **93**, 084101 (2008).

4 Rosenauer, M. & Vellekoop, M. J. 3D fluidic lens shaping—a multiconvex hydrodynamically adjustable optofluidic microlens. *Lab on a Chip* **9**, 1040-1042 (2009).

5 Wee, D., Hwang, S., Song, Y. & Youn, J. Tunable optofluidic birefringent lens. *Soft matter* **12**, 3868-3876 (2016).

6 Dong, L. & Jiang, H. Tunable and movable liquid microlens in situ fabricated within microfluidic channels. *Applied Physics Letters* **91**, 041109 (2007).

7 Shi, J., Stratton, Z., Lin, S.-C. S., Huang, H. & Huang, T. J. Tunable optofluidic microlens through active pressure control of an air–liquid interface. *Microfluidics and Nanofluidics* **9**, 313-318 (2010).

8 Lea-Smith, D. J., Bombelli, P., Vasudevan, R. & Howe, C. J. Photosynthetic, respiratory and extracellular electron transport pathways in cyanobacteria. *Biochimica et Biophysica Acta (BBA)-Bioenergetics* **1857**, 247-255 (2016).

9 Tian, H., Shao, J., Ding, Y., Li, X. & Liu, H. Numerical characterization of electrohydrodynamic micro-or nanopatterning processes based on a phase-field formulation of liquid dielectrophoresis. *Langmuir* **29**, 4703-4714 (2013).

10 Lim, C. Y. & Lam, Y. C. Phase-field simulation of impingement and spreading of micro-sized droplet on heterogeneous surface. *Microfluidics and nanofluidics* **17**, 131-148 (2014).

11 Mondal, P. K., DasGupta, D. & Chakraborty, S. Interfacial dynamics of two immiscible fluids in spatially periodic porous media: The role of substrate wettability. *Physical Review E* **90**, 013003 (2014).

12 De Menech, M., Garstecki, P., Jousse, F. & Stone, H. Transition from squeezing to dripping in a microfluidic T-shaped junction. *journal of fluid mechanics* **595**, 141-161 (2008).

13 Fullana, J.-M., Ling, Y., Popinet, S. & Josserand, C. Droplet in micro-channels: A numerical approach using an adaptive two phase flow solver. *arXiv preprint arXiv:1507.04329* (2015).

14 Lin, P.-T., Chu, H.-Y., Lu, T.-W. & Lee, P.-T. Trapping particles using waveguide-coupled gold bowtie plasmonic tweezers. *Lab on a Chip* **14**, 4647-4652 (2014).

15 Berthelot, J. *et al.* Three-dimensional manipulation with scanning near-field optical nanotweezers. *Nat Nano* **9**, 295-299, doi:10.1038/nnano.2014.24 (2014).

Chapter 3.

Enhanced Plasmonic Tweezer

3.1. Introduction

Localized surface plasmon resonance (LSPR) is a nanoscale phenomenon arising from a strong coupling between light and metal nanoparticles. Once the incident light is coupled with the abundant free electrons in the metal nanoparticles, collective oscillations of the electrons are induced. This is well-known as localized surface plasmon[1,2]. Recently, the LSPR has emerged as a promising tool in several fields such as photovoltaics[3-5], photocatalysis, light emission, biomedical diagnosis and therapy, etc.[6] due to its photophysical characteristics including near-field enhancement[7], far-field scattering[8], hot electron generation and plasmonic heating[5].

A plasmonic optical tweezer (POT), one of the most promising applications of the LSPR, has been studied to overcome the limit of conventional optical tweezers induced by diffraction[9]. For conventional optical tweezers, the optical gradient force is a fundamental element for trapping objects. The force is generated by a tightly focused laser beam with a high numerical aperture objective. However, as the size of objects decreases, the gradient force diminishes by the third power of the size[10]. Therefore, a high power is required to trap small objects with a diameter smaller than about a few hundred nanometers, which inevitably causes the instability and damage of the trapped objects due to heat[11]. Meanwhile, previous studies about POT have taken advantage of near-field enhancement or plasmonic heating to establish power-efficient tweezer systems for trapping a single particle or multiple particles/cells rapidly and stably[12-20]. In general, those researches have fabricated gold nanodisks[12,20], gold nanoislands[13-15], gold nanobowties[16,18] and gold nanopyramids[17] as a plasmonic structure, and trapped and manipulated particle/particles or cells with much lower laser power than that used in conventional optical tweezers.

In this study, a new plasmonic tweezer was demonstrated by using the plasmonic heating effect. Hybrid nanostructure was fabricated depositing gold nanoparticles (AuNPs) on the zinc oxide nanorods (ZnONRs), which exhibited outstanding enhancement in the LSPR-induced plasmonic heating and subsequently the trapping performance. Unlike previous studies manipulating only the nanostructural geometry of gold, we introduced additional material, i.e., ZnO and tuned its geometry, thus intensifying the incident light energy for the light transmission to the gold nanoparticles. Even though Kotsifaki et al. demonstrated the enhanced plasmonic optical tweezer with a hybrid structure consisting of nanostructured silicon substrate coated with gold nanoparticles, the precise analysis about the origin of the enhancement was not performed[21]. In this regard, three dimensional (3D) numerical analysis was carried out to confirm the synergistic effect induced by our hybrid structure. Maximum temperatures due to the plasmonic heating and the near-field enhancement factors were predicted. After that, the enhanced plasmonic heating and multiple-trapping ability were experimentally verified by fabricating the hybrid plasmonic structure. Moreover, the additional synergistic effect of the hybrid structure on the trapping performance was observed and the trapping mechanism was also analyzed. It was indicated that the inertial force generated by natural convection of the medium and the thermophoretic force acted as dominant forces for trapping multiple particles. This is schematically described in Fig. 3.1.1.

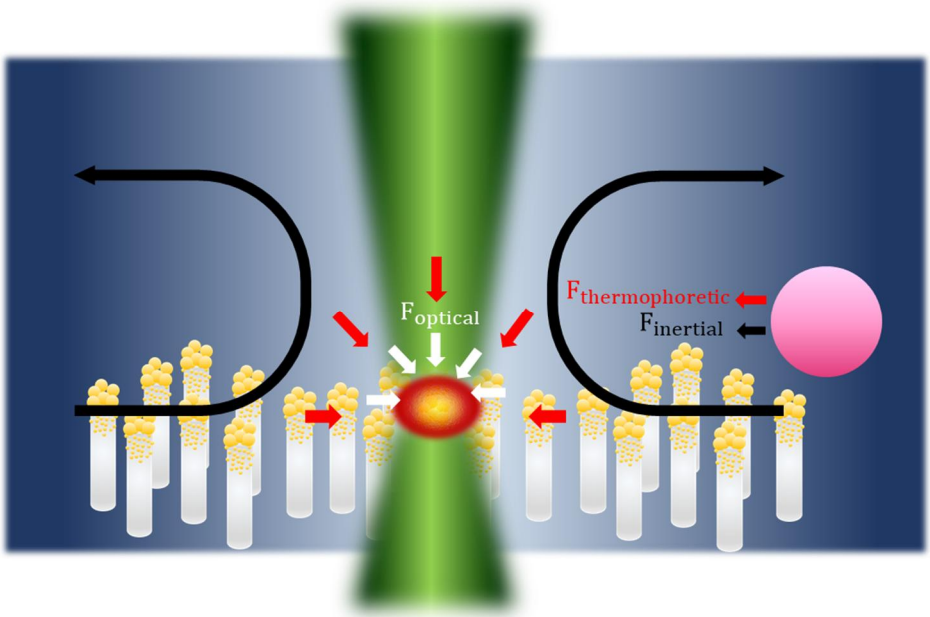

Figure 3.1.1. Schematic description. Working principle of the plasmonic tweezer proposed in this study. The scale of the arrows are not relevant to the magnitude of the forces.

3.2. Experimental section

3.2.1. Preparation of plasmonic substrate

The hybrid nanostructure was fabricated by using the hydrothermal growth of ZnONRs and the following photochemical reduction of AuNPs. Details on the processes are explained in literature[22,23]. Briefly, the hydrothermal growth was conducted in two steps, seeding and growth. First, a glass substrate was cleaned with acetone, DI water and isopropyl alcohol in order. For the seeding step, seed solution was prepared by dissolving zinc acetate ($Zn(C_2H_30_2)_2$) in ethanol (0.03 M). Then, the glass substrate was spin-coated with the seed solution three times at 1000 rpm for 10 s, followed by annealing at 250 °C for 20 min to remove residual solvent and form crystal seeds. For the growth step, the growth solution was prepared by dissolving zinc nitrate hexahydrate ($Zn(NO_3)_2 \cdot 6H_20$) and hexamethylenetetramine ($C_6H_{12}N_4$) in DI water (0.03 M). Then, the coated glass was immersed in the aqueous solution at 90 °C for 2 h and rinsed several times. After then, the photochemical reduction of AuNPs on the ZnONRs was conducted. The glass was immersed in chloroauric acid ($HAuCl_4$) aqueous solution (1 mM) and irradiated with an UV lamp (UVT series, DongSeo, Chungnam, Korea). The size of the AuNPs could be controlled by adjusting irradiation time. In other words, the longer irradiation time led to the larger size of the AuNPs due to the increased reduction time. Finally, three kinds of the ZnONRs/AuNPs samples were fabricated by controlling the irradiation time: 30 min (ZnO_Au_30 min), 1 h (ZnO_Au_1 h) and 3 h (ZnO_Au_3 h). Control samples, i.e., AuNIs were fabricated by thermal evaporation[14]. Gold film with a thickness of 8 nm was deposited on the glass by a thermal evaporation system (MHS-1800, Muhan). The base pressure was 2.0×10^{-5} Torr, and the deposition rate was 0.1 $\mathring{A}/s$. Thereafter, two different AuNIs samples were formed without (AuNIs_p) and with (AuNIs_a) annealing treatment of the Au film at 550 °C for 12 h. The morphologies and resonant wavelength of the samples were characterized with a scanning electron microscope (SEM, SU70, Hitachi, Tokyo, Japan) and a UV-VIS spectrophotometer (LAMBDA 25, PerkinElmer, Shanghai, China), respectively, as shown in Figs. 3.2.1 (a-f).

3.2.2. Experimental set-up

The optical set-up used for temperature measurement and particle trapping is schematically described in Fig. 3.2.2. The bright-field microscopy setup with a focused laser beam was built. A white light illuminated the overall sample. A linearly polarized 532 nm laser (Samba, Cobolt AB, Solna, Sweden) was used to measure the maximum temperature and temperature distribution around the plasmonic nanostructures, as well as to trap the polystyrene (PS) particles. All the experiments were implemented under various laser power conditions of 0.5 mW, 1 mW, 3 mW and 5 mW, which were modulated by neutral density (ND) filter. The observed images were collected using an objective lens with NA=0.60 (LUCPlanFLN 40x, Olympus, Seoul, Korea), and a web camera (SPC900NC/00, Philips) was used for the observation.

3.2.3. Temperature measurement

The temperature measurement was carried out based on the dependency between the fluorescence efficiency of Rhodamine B (RhB, 0.1 mM solution) and temperature[14,24]. The well-known formula, $\ln(I(T)/I(T_{ref})) = \beta(1/T - 1/T_{ref})$, was used for fitting, where $I(T)$ and $I(T_{ref})$ are the integral fluorescence intensity in the range of 550-700 nm at temperature T and the reference temperature (T_{ref} =20 °C), and β is the proportional constant, respectively. First, data for the calibration curve were obtained in the temperature range from 20 °C to 90 °C with an interval of 5 °C using a fluorometer (QM-4/2005SE, Photon Technology, Birmingham, NJ, USA). Measurement was repeated two or three times to get the average value of β through the subsequent curve fitting process by using the OriginPro (OriginLab Corp., Northampton, MA, USA). As a result, β =3034.7 K was acquired. Detailed results are provided in Fig. 3.2.3. Afterwards, the temperature field and maximum temperature above the samples were determined with the same formula. 20 μL of RhB solution was dropped on the plasmonic substrate and 532 nm laser beam was focused on the substrate to excite the solution. In this measurement, long-pass (LP) filter (E550lp, Chroma Technology Crop., Chicago, IL, USA) was used to

avoid the scattered green laser beam. The resultant fluorescent field image and the fluorescent spectrum of the RhB solution were recorded with a web camera and a spectrometer (SM-240 Spectrometer, Spectral products, Putnma, CT, USA).

3.2.4. Prticle trapping experiment

For the trapping experiments, 20 μL of aqueous suspension containing 1 μm PS particles (F8819, Fluospheres^{TM}, 0.0001 % w/v) or *E.coli* cells was dropped on the plasmonic substrate. 2.06 μm (FH-2040-2, Spherotech Inc., 0.0001 % w/v) and 6.27 μm (FP-6056-2, Spherotech Inc., 0.0001 % w/v) PS particles were also used in this experiment to observe the size effect of the particle on the thermophoretic behavior. In addition, the trapping experiment was carried out for 1 μm PS particles dispersed in 50 mM NaCl solution and 2.06 μm PS particles dispersed in 50 mM NaOH solution to verify the thermophoretic force through the electrolyte effect. The focal spot diameter was about 1.1 μm , which was measured using the Web Cam image. To obtain the bright field images during the trapping, band-pass (BP) filter (D490/40m, Chroma Technology Crop.) was used to remove the 532 nm laser beam and the fluorescent emission of the fluorescent PS particles.

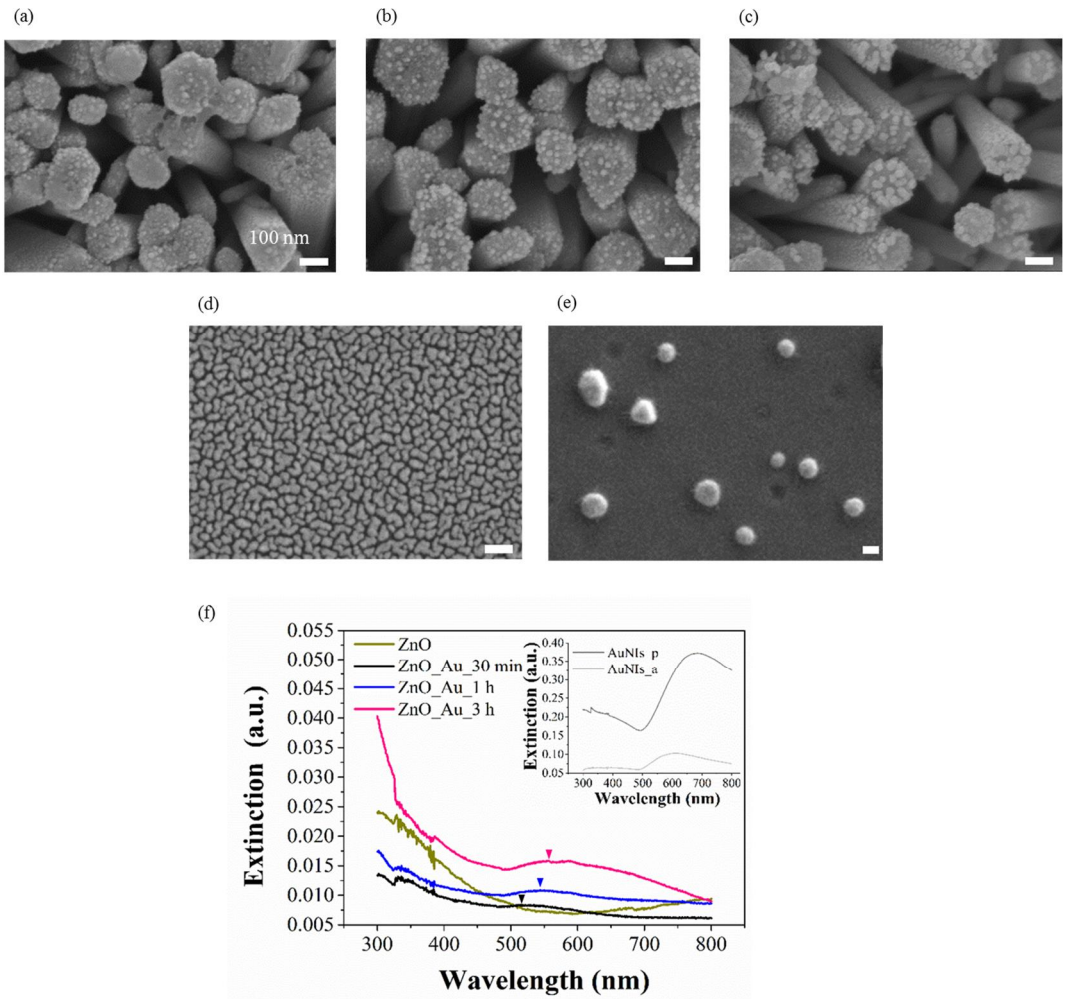

Figure 3.2.1 Characterization of the samples and experimental setup. SEM images of the fabricated plasmonic samples: (a) ZnO_Au_30 min, (b) ZnO_Au_1 h, (c) ZnO_Au_3 h, (d) AuNIs_p and (e) AuNIs_a. The scale bar implies 100 nm. (f) Extinction spectra of the fabricated plasmonic samples. The inset shows the spectra of the AuNIs samples.

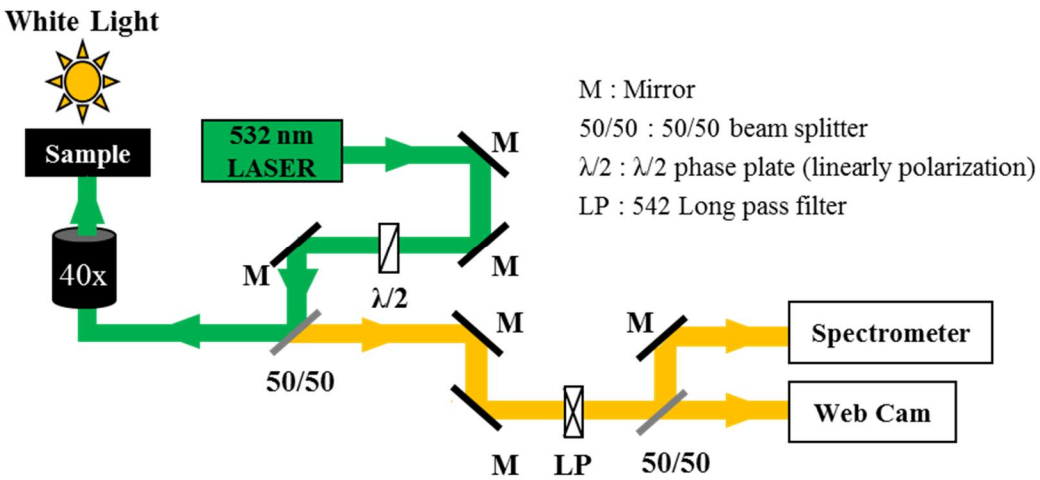

Figure 3.2.2. Experimental setup. Optical setup for the temperature measurement and particle trapping experiment.

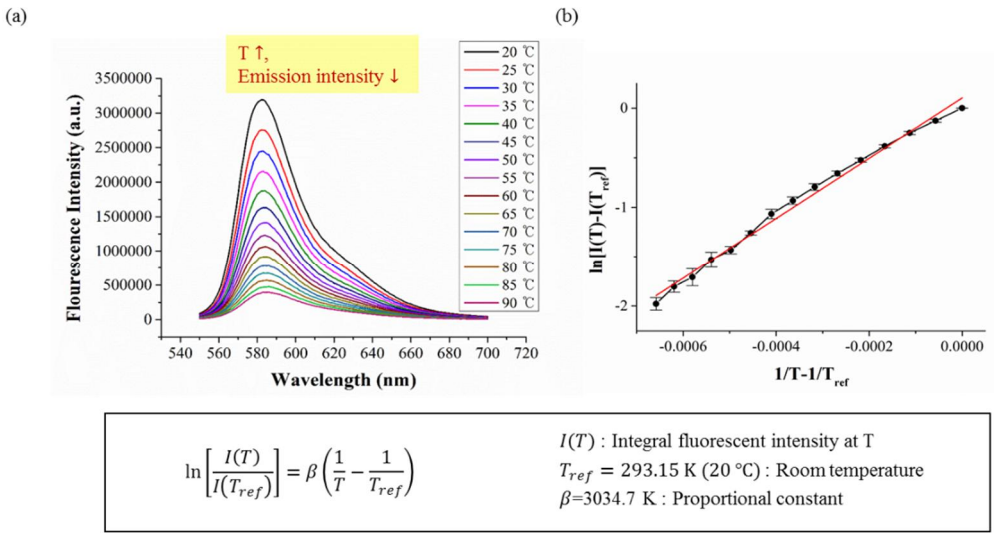

Figure 3.2.3. Temperature field measurement based on the fluorescent efficiency method. (a) Fluorescent spectra of Rhodamine B solution (0.1 mM) at different temperatures. (b) Curve fitting of the experiment data.

3.3. Numerical analysis

3D multiscale numerical simulation of electromagnetic field (EM) and coupled temperature-velocity fields (T-V) was carried out to understand the enhancement in LSPR of the hybrid plasmonic structure by using COMSOL Multiphysics®[16]. 3D meshes used for the simulation are described in Fig.3.3.1. Three different scaled domains were addressed: nanoscale, mesoscale and macroscale domains. The nanoscale domain consisted of ZnONRs and AuNPs, and water and glass were included in the mesoscale and macroscale domains. The usage of the mesoscale domain help to precisely calculate EM and T-V fields around the nanostructure. The dimensions of the geometries were determined based on SEM images and experimental conditions. The diameter (d_{NR}) and length (l_{NR}) of the ZnONR were 115 nm and 870 nm, respectively, and the distance between the ZnONRs (D_{NRs}) was a quarter of d_{NR}. Three different diameters of 10, 20, and 30 nm were considered for the AuNP in the analysis.

The diameter of the mesoscale domain (d_{Meso}) was $1.1\,\mu m$, and the lengths (l_{Water} and l_{Glass}) of water and glass regions were $2.3\,\mu m$ and $0.3\,\mu m$, respectively. The width (w) and depth (d) of the macroscale domain were 1 cm, and the heights (h_{Water} and h_{Glass}) of water and glass regions were 3 mm and 1 mm, respectively. To explain the the roles of ZnONRs, two control structures were also simulated. One structure was composed of only AuNPs with a diameter of 20 nm on the glass substrate, and the other structure consisted of only ZnONRs on the glass substrate.

The EM was first calculated in the mesoscale domain to obtain the near-field enhancement around the nanostructures and the heat power (Q) generated by the plasmonic heating of AuNPs.

$$\nabla \times (\nabla \times \mathbf{E}) - k_0^2 \varepsilon_r \mathbf{E} = 0 \tag{3-8}$$

where ∇ is the nabla operator, $\mathbf{E}$ is the total electric field, k_0 is the free space wavenumber, and ε_r is the complex relative permittivity. It was assumed that an x-polarized 532 nm Gaussian beam propagates in z-direction from the glass substrate and the diameter of focal spot was set to be $1.1\,\mu m$. The perfectly matched layer was taken

into account as a boundary condition to avoid the reflection of wave at the outer boundaries.

After the calculation of EM, the coupled T-V was solved in the macroscale domain to acquire temperature and velocity fields. The fields were modeled using the following time-dependent coupled momentum-energy equations.

$$\rho C_p \frac{\partial T}{\partial t} + \rho C_p \mathbf{u} \cdot \nabla T + \nabla \cdot (-k \nabla T) = Q \tag{3-2}$$

$$\rho_0 \frac{\partial \mathbf{u}}{\partial t} + \rho_0 (\mathbf{u} \cdot \nabla)\mathbf{u} = \nabla \cdot [-p\mathbf{I} + \mu(\nabla u + (\nabla u)^T)] + \mathbf{F} \tag{3-3}$$

$$\mathbf{F} = g\rho_0 \beta (T - T_0)\mathbf{z} \tag{3-4}$$

where ρ is the density of matter, C_p is the heat capacity, $\mathbf{u}$ is the flow velocity, T is the temperature, k is the thermal conductivity, Q is the heat source, ρ_0 is the density at room temperature (20 °C), p is the pressure, $\mathbf{I}$ is the identity tensor, μ is the dynamic viscosity, $\mathbf{F}$ is the volume force induced by the buoyancy in non-isothermal flow, g is the gravitational acceleration, β is the temperature-dependent thermal expansion coefficient of water and T_0 is the room temperature. The Boussinesq approximation was adopted for solving the buoyancy-driven natural convection, and Q was obtained from a volume integral of plasmonic heating around the AuNPs.[16] Temperature was fixed at 20 °C at all outer boundaries, and no-slip conditions were used on the surface of wall and at the outer boundaries.

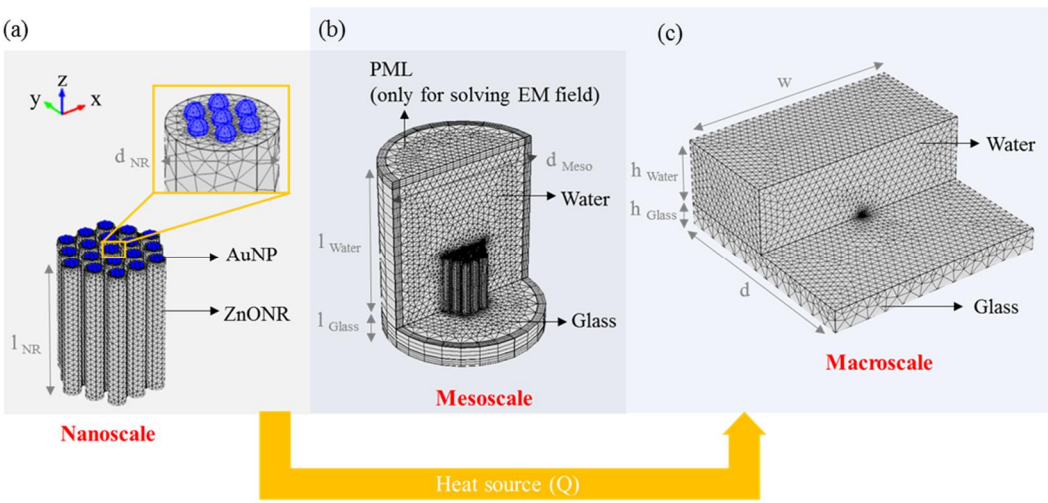

Figure 3.3.1. Geometries for numerical simulation. 3D meshes of the domains used for the multiscale simulation: (a) nanoscale, (b) mesoscale and (c) macroscale domains.

3.4. Results and discussion

3.4.1. Prediction and analysis of synergistic effects

Synergistic effect of the hybrid structure on the enhancement of LSPR is confirmed by numerical simulation. Two main characteristics, plasmonic heating effect and near-field enhancement, are investigated for the quantitative comparison between the LSPR phenomena of AuNPs and ZnONRs/AuNPs structures. The background electric field (E_0) is shown in the form of the Gaussian beam (Fig. 3.4.1(a)). Fig. 3.4.2(a) shows the temperature fields induced by the plasmonic heating, where the maximum temperature (T_{max}) of AuNPs and ZnONRs/AuNPs are about 32 °C and 52 °C , respectively. The electric fields are also compared as shown in Fig. 3.4.1(b). The maximum near-field enhancement factors ($|E_{max}/E_0|$) of AuNPs and ZnONRs/AuNPs are about 5 and 10.3, respectively. T_{max} of ZnONRs/AuNPs is increased by 61 %, and $|E_{max}/E_0|$ is increased by 51.5 % compared with those of AuNPs. Furthermore, ZnONRs/AuNPs can concentrate the heat generated around the nanostructures as seen in Fig. 3.4.2(a). The concentration of the heat is attributed to the thermal conductivity of ZnO higher than that of water, which means that the generated heat around AuNPs is transferred to ZnONR faster than to water. This gives much higher temperature gradient (∇T) around the ZnONRs/AuNPs than the AuNPs. In this regard, the temperature gradients along the x-direction ($\partial T/\partial x$) for AuNPs and ZnONRs/AuNPs are investigated at the same distance (500 nm) in the z-direction above the apex of the AuNPs in each structure (Fig. 3.4.2(b)). As a result, the superposed graphs clarify that the temperature gradient in the x-direction, $\partial T/\partial x$, has higher values for the ZnONRs/AuNPs. Since we detect the in-plane view of the particle motion during the particle trapping experiment, $\partial T/\partial x$ is evaluated in the Cartesian coordination system to compare the simulation result with the experimental result. Therefore, the temperature distribution around the ZnONRs/AuNPs indicates that the steep ∇T exists along the radial direction. These synergistic effects, i.e., significantly increased T_{max} and ∇T , are regarded as the main factor for enhancing the particle trapping performance of the plasmonic tweezer. Some of the recent studies achieved particle trapping from far-field by utilizing the plasmonic heating[12-16]. In these studies, the

plasmonic heating resulted in the buoyancy-driven natural convection of the particle dispersed medium as well as the thermophoretic motion of the particles. It is obvious that higher T_{max} and steeper ∇T contribute to larger particle motion by increasing both natural convection and thermophoresis, which may be explained by considering equations (3-4) and (3-5)[15].

$$v_T = -D_T \nabla T \tag{3-5}$$

where v_T is the particle drift velocity, D_T is the thermal diffusion coefficient and ∇T is the temperature gradient. Indeed, our simulation results confirm that the fluid velocity in ZnONRs/AuNPs by natural convection is much faster than that in AuNPs (Fig. 3.4.1(c)). Thus, the trapping velocity is increased due to the hybrid structure.

The role of the ZnONR for the enhancement of LSPR as well as the synergistic effect is investigated. Figs. 3.4.3(a) and (b) show the scattered electric field of the nanostructures with the poyning vectors. The poynting vector represents the directional energy flux of the electromagnetic field over the structures. The results convince that the larger energy of light is transferred to AuNPs at the interface between the AuNPs and the ZnONRs than between the AuNPs and the glass. The reason can be explained with the results in Fig. 3.4.3(c). It is revealed that the ZnONR guides and amplifies the incident light along the nanorod via leaky waveguide modes[25,26]. In other words, the light propagates not only internally but also externally along the nanorods with enhanced intensity as shown in the magnified view in the x-y plane in Fig. 3.4.3(c). The enhancement of the wave-guided light is explained with the material property of ZnO and the nanorod geometry. That is, the high dielectric constant of ZnO results in strong dipole scattering at the nanorod surface, and the rod geometry parallel to the optical axis of the Gaussian beam causes the efficient wave guiding of the dipole-scattered light. Moreover, the dipole coupling between the nanorods further enhances the light intensity. Since the ZnO doesn't absorb the light at the wavelength of 532 nm, it is an adequate material for guiding and transferring the light energy to AuNPs[25].

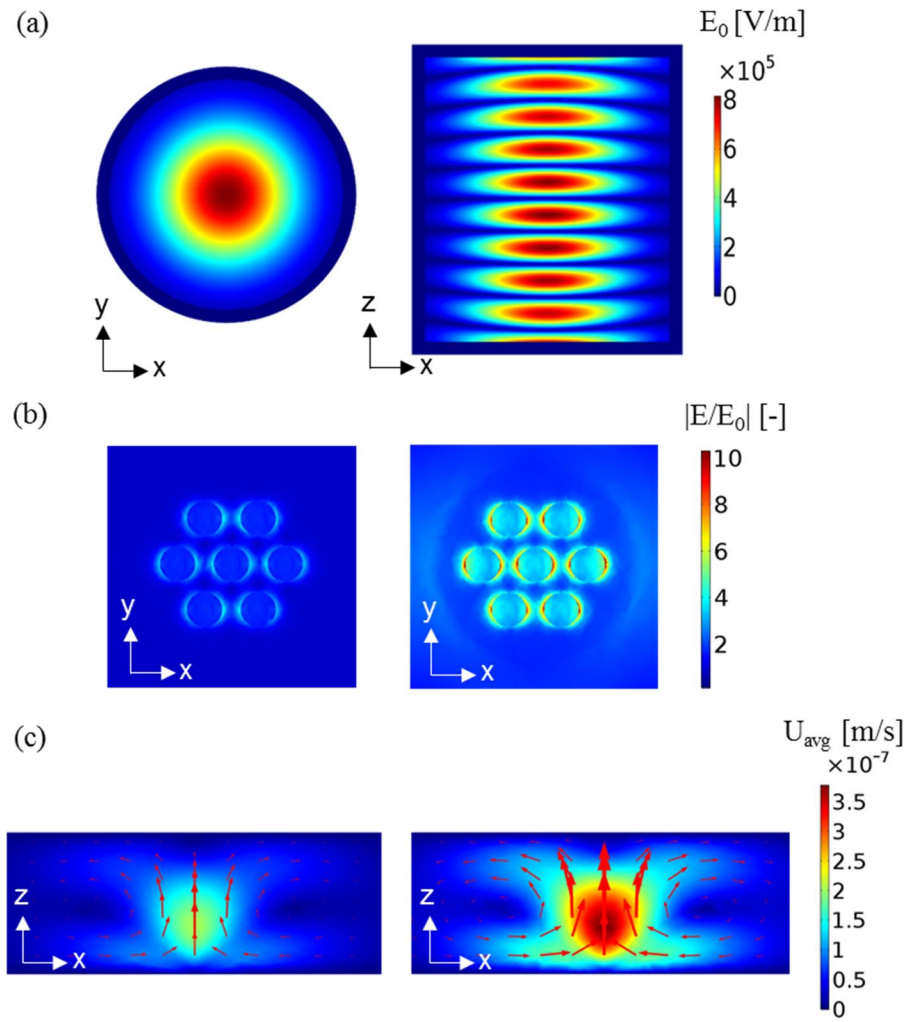

Figure 3.4.1. Simulated electric fields and velocity fields. (a) Background electric fields (E0) with a Gaussian distribution in the x-y plane (left) and x-z plane (right) views. Comparison of (b) enhancement distributions (|E/E0|) of the scattered electric fields at the same altitude of AuNPs and (c) the average velocity fields at y = 0 between AuNPs (left) and ZnONRs/AuNPs (right). The diameter of AuNP is 20 nm in (b) and (c). Scales of the red arrow in (c) are same for the comparison.

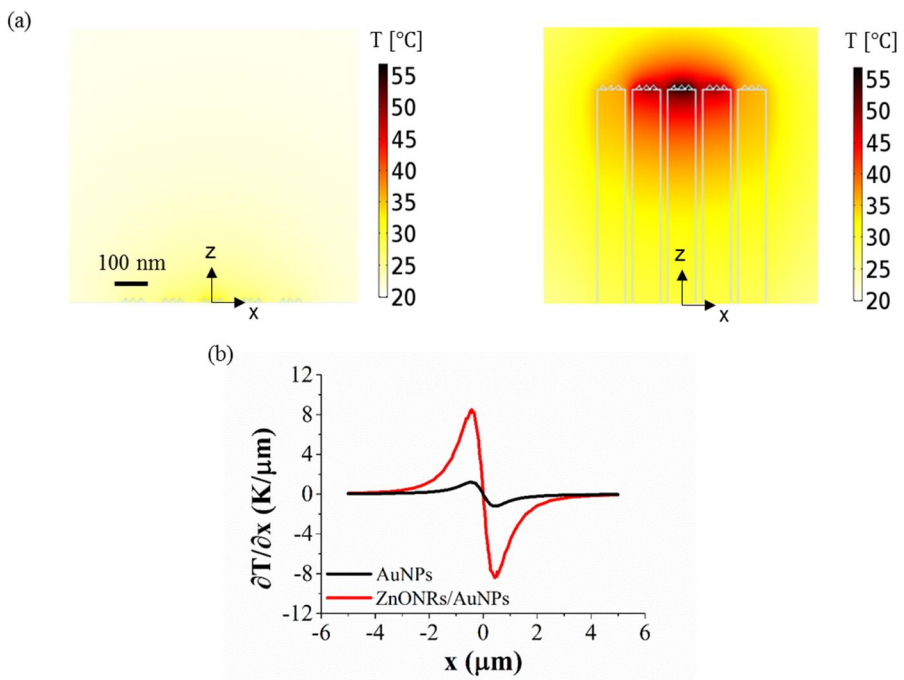

Figure 3.4.2. Comparison of the plasmonic heating effect between the AuNPs and the ZnONRs/AuNPs. (a) Simulated temperature fields around the AuNPs (left) and ZnONRs/AuNPs (right) at y = 0. (b) Simulated temperature gradient along the x-direction for the AuNPs (black line) and ZnONRs/AuNPs (red line).

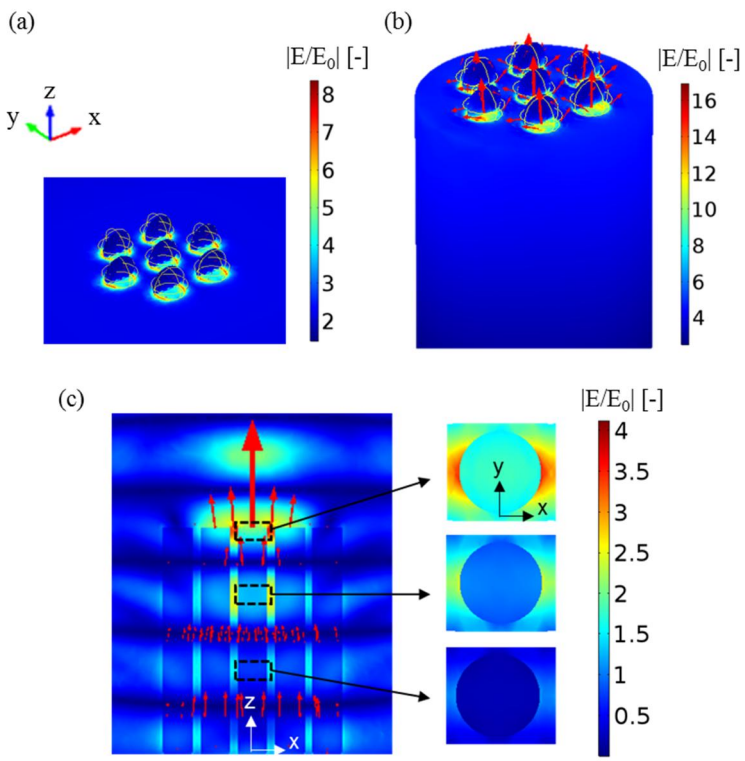

Figure 3.4.3. Simulation of the synergistic effect. Enhancement distribution of the scattered electric field with the poynting vectors for (a) AuNPs, (b) ZnONRs/AuNPs and (c) ZnONRs. The scales of the arrows for (a) and (b) are the same and that for (c) is magnified 50 times.

3.4.2. Characterization of plasmonic substrate

The SEM images shown in Figs. 3.2.1(a-c) confirm that the AuNPs are well-deposited on the surfaces of the ZnONRs. The average diameters of the AuNPs for the hybrid structure fabricated with 30 min, 1h, and 3h irradiation time are about 10 nm, 20 nm and 30 nm, respectively. The average diameter and length of the ZnONRs are 115 nm and 870 nm, respectively. These values were used for constructing the geometric model for numerical simulation. Additionally, Fig. 3.4.4 shows the morphology of the ZnONRs according to the number of spin coating of the seed layer. Fig. 3.4.5 predicts that the shorter distance between the ZnONRs leads to larger LSPR. As a result, spin-coating have been carried out 3 times to fabricate homogeneous and dense ZnONRs. The annealing treatment allows AuNIs to have larger size and lower density as shown in Fig 3.2.1(d, e). The resonance peaks of ZnO_Au_30 min, ZnO_Au_1 h and ZnO_Au_3 h, AuNIs_p and AuNIs_a are 515 nm, 544 nm, 555 nm, 611 nm and 684 nm, respectively.

3.4.3. Plasmonic heating

The plasmonic heating caused by the non-radiative decay of the excited LSPR entails a temperature increase around the metal nanostructure. This temperature increase depends on not only the physical properties of materials such as the imaginary part of the dielectric constant, but also the size of and the distance between the nanostructures. For instance, it is known that the temperature increase is proportional to the diameter of metal nanoparticles[27]. In Fig. 3.4.6(a), the measured T_{max} values at four different laser powers are demonstrated for each sample. T_{max} for ZnO_Au_30 min, ZnO_Au_1 h, ZnO_Au_3 h, AuNIs_p and AuNIs_a are 39.1 °C , 65.3 °C , 84.5, 54.1 °C and 32.5 °C , respectively, at a laser power of 1 mW. As the diameter of the AuNPs increases, the maximum temperature of the ZnONRs/AuNPs increases. This is consistent with the simulation results (Fig. 3.4.7). Since the distance between the AuNPs decreases as the diameter of the AuNPs increases in our system, the plasmonic coupling effect enhances the LSPR more largely as the diameter increases. For the ZnO_Au_1 h and ZnO_Au_3 h, bubbles are generated at P=5 mW due to the large amount of plasmonic heating. For this reason, the temperature

measurement is not allowed. The temperature distribution of the ZnO_Au_1 h sample is also obtained at P=1 mW (Fig 3.4.6(b)). The steep temperature gradient is generated around the focal spot located in the center of the image. To check the reliability of the numerical modeling, T_{max} obtained from the simulation is compared with the experimental results for the ZnONRs/AuNPs samples (Fig. 3.4.6(c)). While the predictions are in good agreement with the experimental results, a small discrepancy is generated due to the simplified geometry of the simulation.

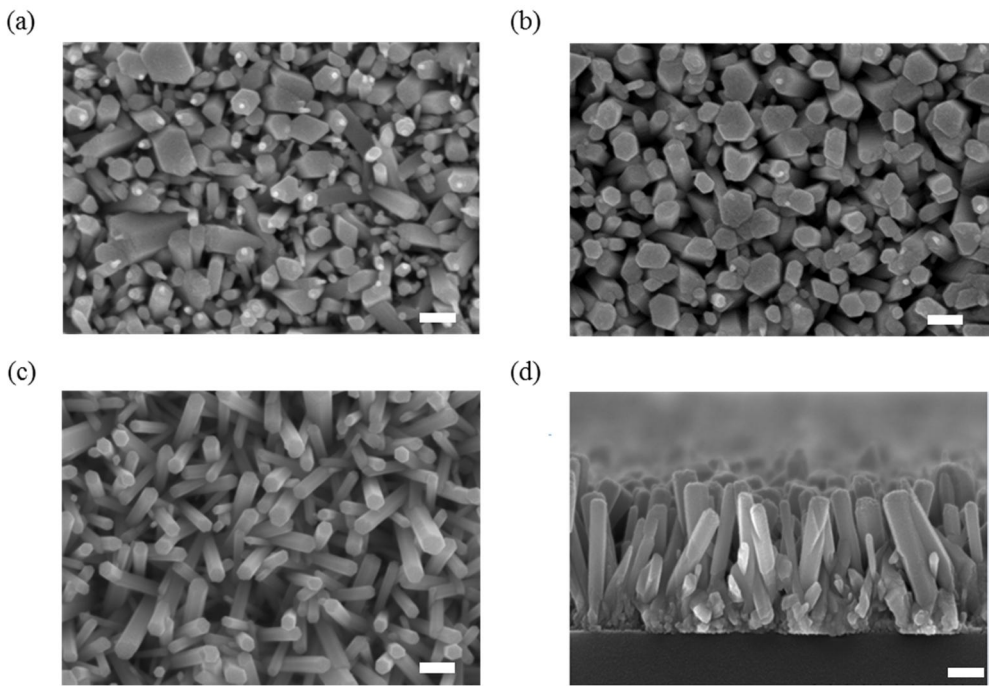

Figure 3.4.4. ZnONR morphology according to the number of spin coating of the seed layer. Top view of the SEM image of the hydrothermally grown ZnONRs by spin-coating of the seed layer (a) 1 time, (b) 2 times and (c) 3 times, respectively. (d) Side view of the SEM image of the hydrothermally grown ZnONRs by spin-coating of the seed layer 3 times. The scale bar is 100 nm.

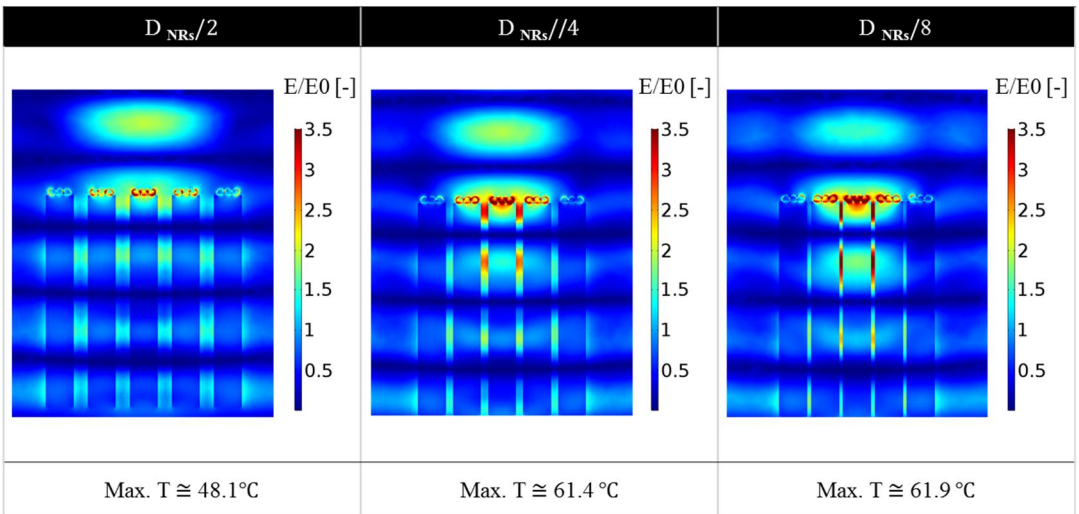

Figure 3.4.5. Distance effects of ZnONR on LSPR. Enhancement distributions (|E/E0|) of the scattered electric fields and maximum temperature according to the different distance between ZnONRs of AuNPs_ZnONRs structure. The diameter of AuNP is 30 nm.

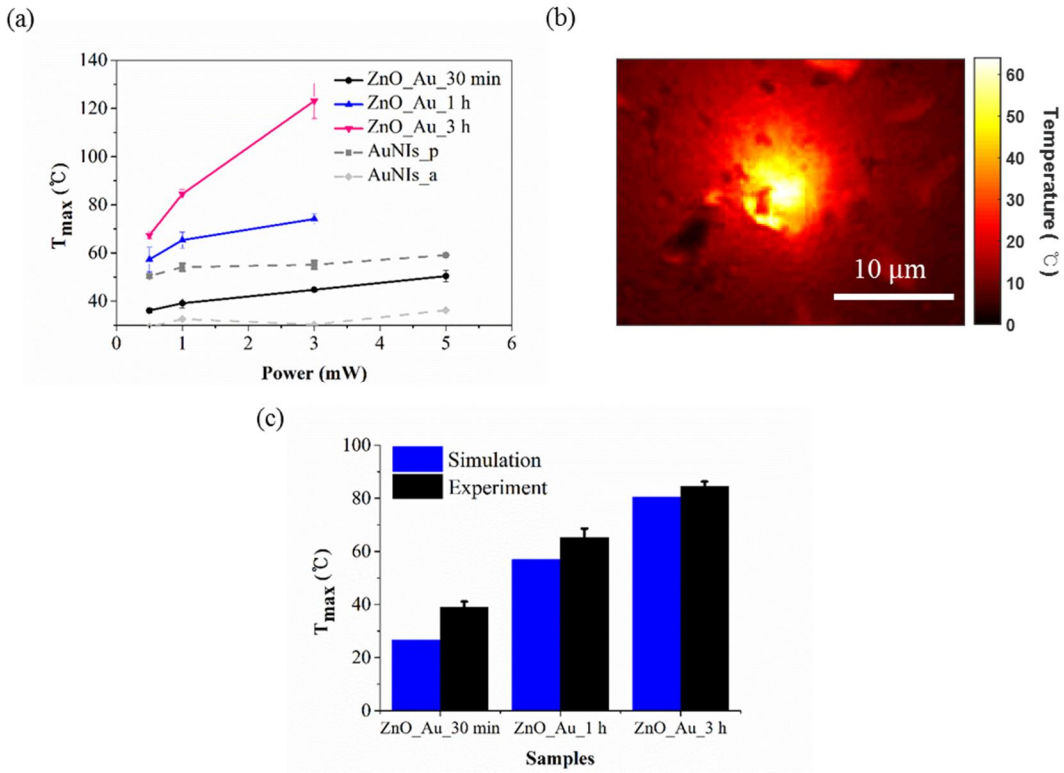

Figure 3.4.6. Temperature analysis. (a) Maximum temperatures of the samples measured at four different laser powers. (b) Temperature distribution over the surface of the ZnO_Au_1 h sample at P=1 mW. (c) Comparison of the maximum temperatures between the experimental and simulation results.

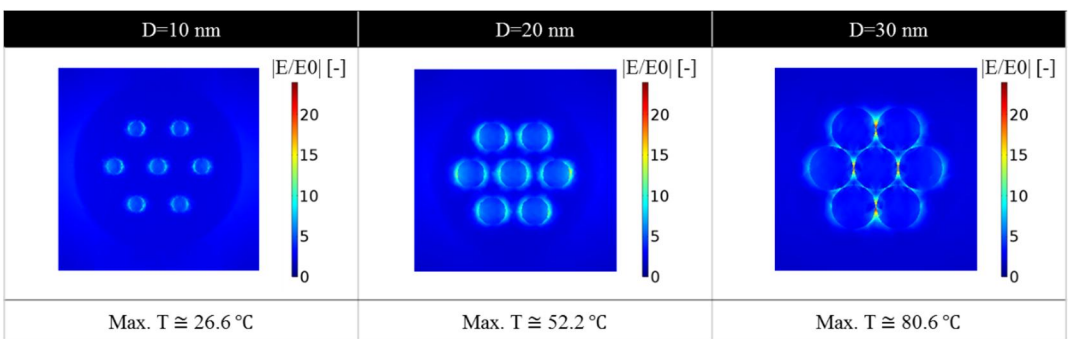

Figure 3.4.7. Size effects of AuNPs on LSPR. Enhancement distributions (|E/E0|) of the scattered electric fields and maximum temperature with respect to the different AuNP diameters of AuNPs_ZnONRs structure.

3.4.4. Enhanced particle trapping performance

The trapping abilities of the fabricated nanostructure samples are evaluated. Fig. 3.4.8 shows the successive images during the trapping experiment of 1 μm PS particles on the ZnO_Au_1h plasmonic substrate at P=1 mW. *E. coli* cells were also successfully trapped in the same conditions (Fig 3.4.9). Trapping velocities are compared quantitatively for different samples at P=1 mW (Fig. 3.4.10(a)) and with respect to the laser powers for ZnO_Au_1h (Fig. 3.4.10(b)). Although high T_{max} induces the fast trapping, there must be a limit due to the thermal-driven instability and bubble generation. In this respect, trapping PS particles is not feasible with ZnO_Au_3h at P=1 mW and with ZnO_Au_1h at P=3 mW. Because of the relatively high local temperature around the focal spot in those conditions, the particles in the trapping region undergo a vigorous Brownian motion in unstable state. On the other hand, the AuNIs_a cannot trap any particles, which is attributed to the low local temperature and temperature gradient. We also confirmed that bare ZnONRs could not trap any particles at all. Overall, the ZnO_Au_1h at P=1 mW demonstrates the best trapping performance in our system. Fig. 3.4.10(a) and Fig. 3.4.11 show that the particle trapping velocity is much faster on the ZnO_Au_1h substrate than on the ZnO_Au_30 min substrate at P=1 mW. As a result, we expect that the trapping efficiency would increase as AuNP diameter increases to around 20 nm due to the increased temperature gradient, but then the efficiency would decrease as the diameter reaches to 30 nm due to the thermally induced instable motion of the particles. For the same reason, the trapping efficiency would increase as the laser power increases to around 3 mW in the case of the ZnO_Au_1h sample. The stable particle trapping is possible on the ZnO_Au_1h, and the trapped particles can migrate to a different location stably by moving the laser beam to a different position

3.4.5. Verification of synergistic effects

Since the number density, shape and size of the Au nanostructures fabricated are quite different, direct comparison of T_{max}'s between the ZnONRs/AuNPs and AuNIs is not appropriate to look into the effect of the ZnONRs. Instead, the role of the ZnONRs can be inferred by comparing the trapping performances between the ZnO_Au_30 min and the AuNIs_p. Although the ZnO_Au_30 min generates less heat than the AuNIs_p (Fig. 3.4.6(a)), its trapping velocity is comparable with that of the AuNIs_p and even faster after 137 s as shown in Fig. 3.4.8(c). Furthermore, the ZnO_Au_30 min traps the particles at P=0.5 mW unlike the AuNIs_p. As aforementioned, far-field particle trapping performance is mainly affected by the natural convection of medium and the thermophoretic motion of particles. These motions are determined by the local temperature difference (or temperature gradient), but not by the maximum temperature itself. Therefore, the measured data imply that the ZnONRs concentrate the generated heat around the nanostructures and then generate higher temperature gradient around ZnO_Au_30 min than the control sample, AuNIs_p, as predicted in the simulation.

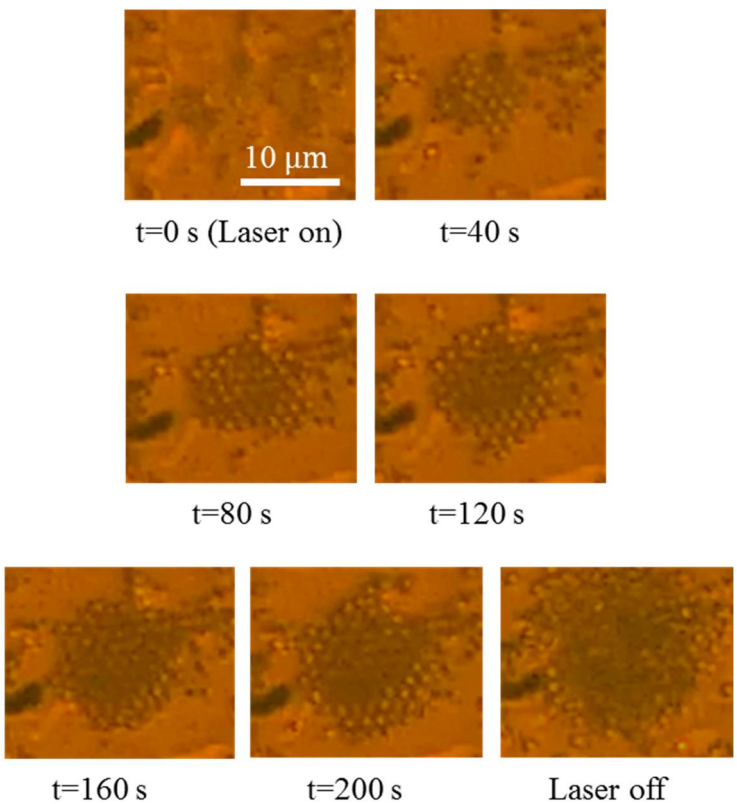

Figure 3.4.8. Particle trapping experiments. Successive images obtained in the trapping experiment with the 1 µm PS particles on the ZnO_Au_1 h sample at P=1 mW.

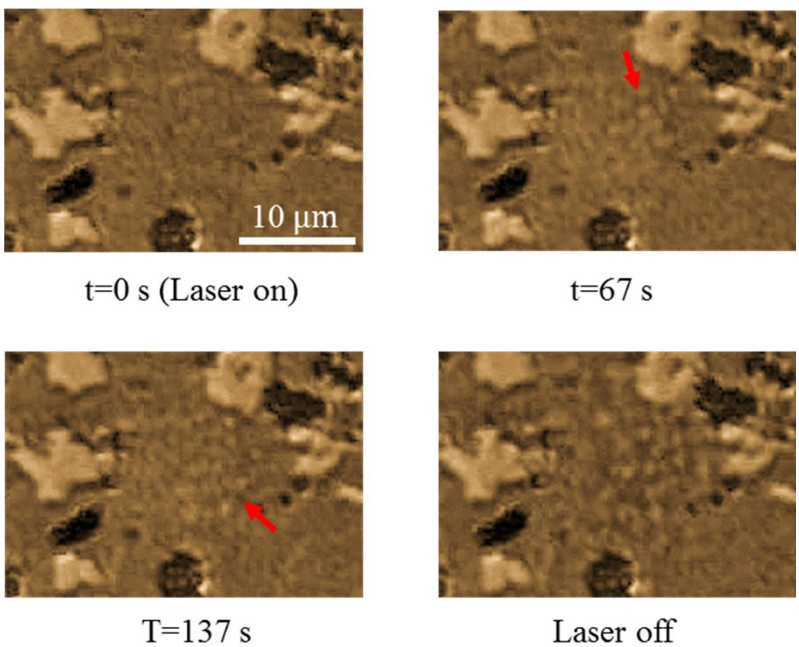

Figure 3.4.9. Particle trapping experiments. Successive images obtained in the trapping experiment with the *E. coli* cells on the ZnO_Au_1 h sample at P=1 mW. The red arrows indicate the trapped cells.

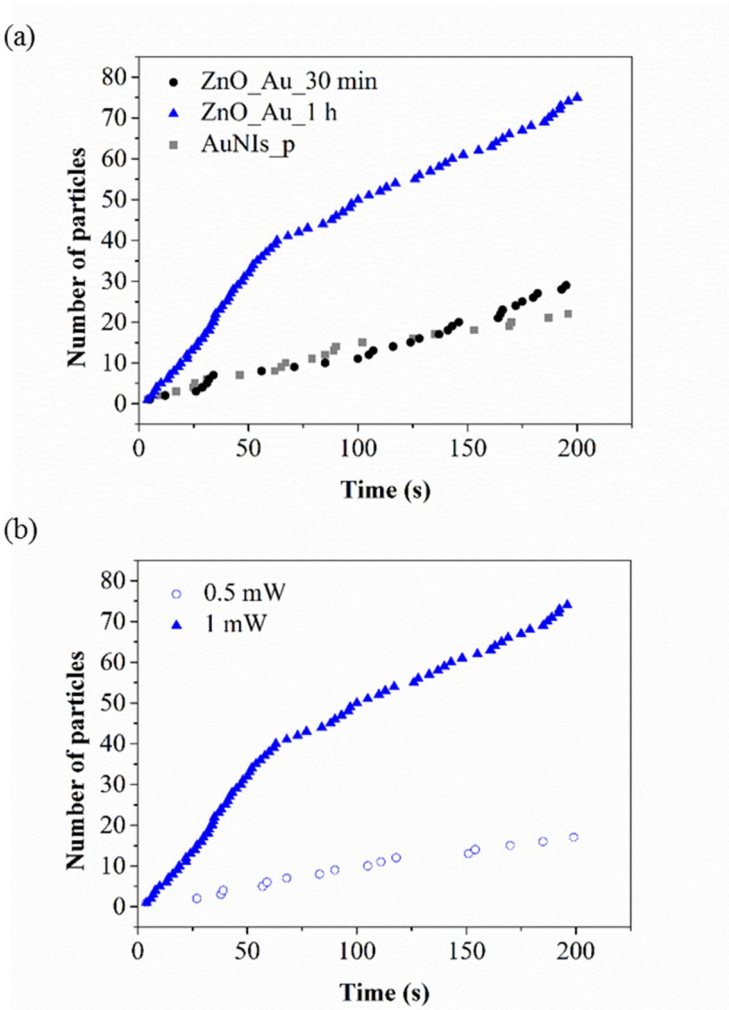

Figure 3.4.10. Particle trapping experiments. Number of the trapped PS particles with respect to (a) the three different samples and (b) the two different laser power conditions with the ZnO_Au_1 h sample.

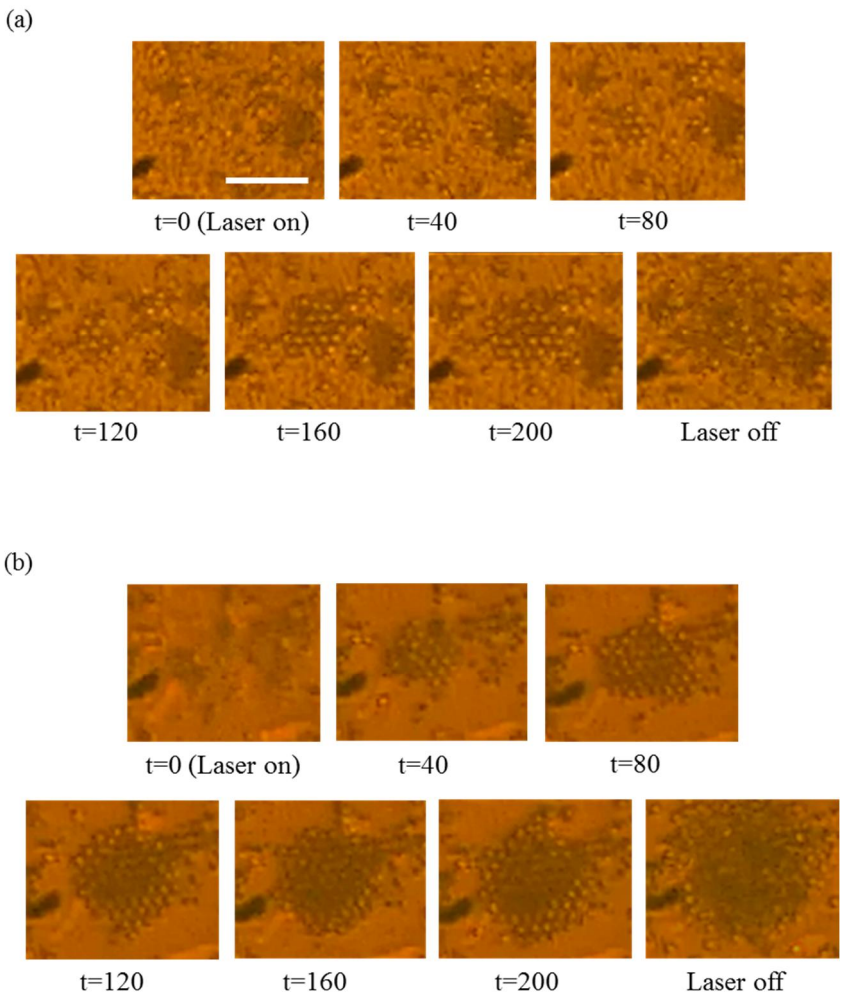

Figure 3.4.11. Particle trapping experiments. Successive image frames of trapping experiment of 1 μm PS particles on (a) ZnO_Au_30 min and (b) ZnO_Au_1h samples.

3.4.6. Analysis of trapping forces

The driving forces exerted on the objects during the trapping are analyzed in more detail. In fact, the optical gradient force is meaningful only in the near-field that is typically limited to sub-μm scale.[15] This force decays exponentially from the surface of the LSPR nanostructures, and the trapping region is far away the focal spot as seen in Fig. 3.4.8 and Fig. 3.4.9. Therefore, additional major forces other than the optical gradient force should exist for the particle trapping. Moreover, the experimental results showed that the particles are forced toward the focal spot from the far-field where only the temperature gradient exists. For this reason, we consider the inertial force and the thermophoretic force. The former is induced by the buoyancy-driven natural convection of the medium (DI water), and the latter is generated due to the non-equilibrium state of thermodynamics. It should be noted that the nature of the thermophoretic force is still controversial.[28] The average velocity and acceleration fields in the x-direction are obtained from the numerical simulation in order to estimate the inertial force (Figs. 3.4.12(a) and (b)). Since the density of PS particles is similar to that of DI water and the particle size is very small, we presume that the particles are stably suspended in the water. It is also assumed that the inertial force imposed on the particle is identical to the force exerted on the same volume of water. Hence, the arrows in the figures can be interpreted as the inertial forces driving the particles along the stream line of the natural convection, which eventually moves the particles out of the hot region. Subsequently, the thermophoretic force is explored by examining the particle size effect and the electrolyte effect on the thermophoretic behavior, which are well observed elsewhere as well[15,29,30]. Equation (3-5) demonstrates that the thermophoretic behavior is determined by the Soret coefficient (S_T), which has the relation of $S_T = D_T/D$, where D is the Brownian diffusion coefficient[29]. Moreover, the dependence of S_T on the particle size[30,31] and electrolyte[32-34] is explained in the literature. Table. 1 shows the calculated average velocity and acceleration along the r-direction from the successive images of the experimental result with respect to the particle size. Although the inertial force accelerates the particles dispersed right above the substrate towards the focal spot as shown in Fig 3.4.12(b), the particles are decelerated in the case of the $2.06\,\mu m$ PS particles. On the other hand, the $1\,\mu m$ PS particles exhibit opposite

behaviors. Furthermore, the 2.06 μm PS particles are not trapped when they reach the vicinity of the focal spot. Instead, they left away from the hot region following the convective flow. The 6.27 μm PS particles showed the same behavior as the 2.06 μm PS particles. This implies that the third force, other than the optical force and the inertial force, is acting due to the heat distribution, which changes the direction of the force depending on the particle size.

For further validation of the thermophoretic force, the trapping experiments are additionally conducted with the particles dispersed in two different electrolytes including NaCl and NaOH solution as shown in Figs. 3.4.13(a) and (b). As a result, the 1 μm PS particles dispersed in NaCl show thermophobic behavior and are not trapped. On the other hand, the 1 μm and 2.06 μm PS particles dispersed in NaOH show thermophilic behaviors and are trapped stably. This different electrolyte effect is based on the difference in the diffusion velocity between the anions and the cations of each electrolyte under temperature gradient[32,33]. The electrolyte effect arises from the macroscopic polarization of the electrolyte ions under the temperature gradient. Na^+ tends to accumulate in colder region relative to Cl^-, whereas Na^+ tends to accumulate in hotter region relative to OH^-. Therefore, those electrolytes generate opposite macroscopic electric field under the temperature gradient for each case. The PS particles we used are negatively charged, thus lots of movable cations screen the charged particle surface in the double layer. Eventually, the thermally driven electric field provokes the accumulation of cations in the double layer toward the negative source of the macroscopic electric field, and the particles experience relative motion toward the positive source. Overall, the electrolyte effect changes the Soret coefficient of the object as demonstrated in the references.[32,33]

The trapping mechanism of our system suggests that the inertial force in the far-field assists the thermophoretic force to trap the 1 μm PS particles more rapidly. However, the thermophoretic force traps the objects stably against the inertial force around the laser-focused hot region after all.

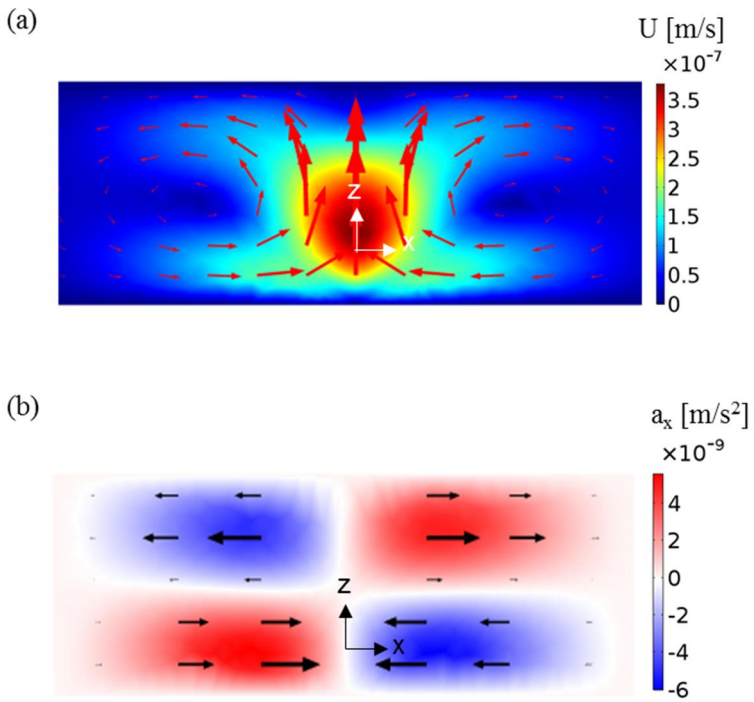

Figure 3.4.12. Analysis of trapping force. Simulation of (a) average velocity field and (b) x component of the acceleration field of water at y = 0. The arrows are the vector quantities indicating the relative magnitudes and directions of the fields at each position.

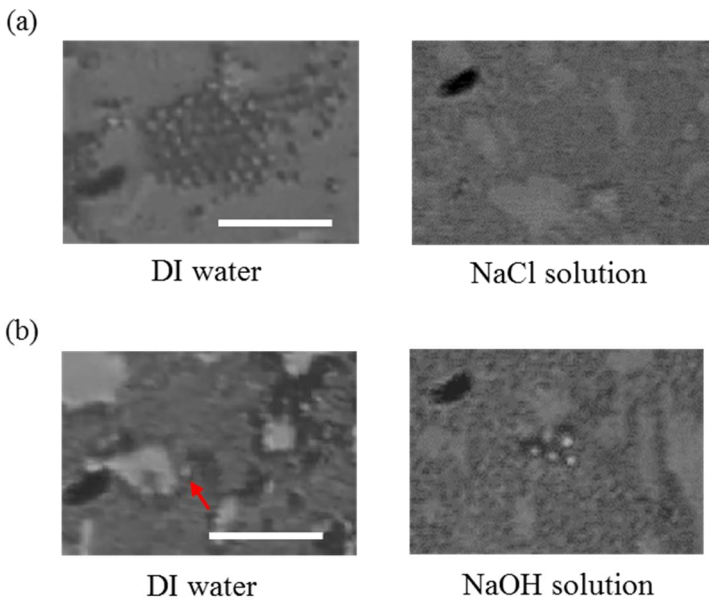

Figure 3.4.13. Analysis of trapping force. Images captured during the trapping experiment of (a) the 1 μm and (b) 2.06 μm PS particles dispersed in DI water (left) and electrolyte solution (right). The red arrow indicate a particle leaving away from the focal spot.

	D = 1 μm (trapped)			D = 2.06 μm (not trapped)		
r (μm)	12.7	9.0	5.6	18.4	12.7	8.4
Avg. v (μm/s)	-1.033	-1.896	-2.469	-0.494	-0.435	-0.306
Avg. a_p ($\mu m/s^2$)	-0.082	-0.345	-0.589	-0.001	0.011	0.013

Table 3.4.1. Average trapping velocity and acceleration along the r-direction for 1 μm and 2.06 μm PS particles. The successive images of trapping experiments with the ZnO_Au_1 h sample at P=1 mW are analyzed to calculate the average trapping velocities (Avg. v) and the average accelerations (Avg. a_p) of the particles. r = 0 at the center of the laser beam.

3.5. Summary

Material and structural effects of the metal-dielectric hybrid nanostructure on the plasmonic tweezer were investigated using the numerical and experimental methods. The AuNPs decorated ZnONRs structure was used as the plasmonic nanostructure based on the numerical modeling. The synergistic effects induced by the hybrid nanostructure were confirmed through the simulation. When the structure is excited by the incident light, the ZnONRs transfer the light energy to the AuNPs located on the top surface of the ZnONRs via leaky wave guide modes along the nanorods, dipole scattering, and dipole coupling between the nanorods. Then AuNPs are eventually excited by more intense light than original light, and generate outstanding enhancement of LSPR. The ZnONRs not only boosted LSPR but also concentrated the generated heat around the nanostructures. The plasmonic substrate containing ZnONRs/AuNPs demonstrated the plasmonic tweezer performance enhanced by the synergistic effects. It is expected that this study will provide a useful way for designing plasmonic structure to fabricate a power-efficient device with high performance in LSPR related fields such as photovoltaics, photocatalysis, light emission and biomedical diagnosis, etc.

3.6. References

1 Jensen, T. R., Malinsky, M. D., Haynes, C. L. & Van Duyne, R. P. Nanosphere lithography: tunable localized surface plasmon resonance spectra of silver nanoparticles. *The Journal of Physical Chemistry B* **104**, 10549-10556 (2000).

2 Chen, X.-J., Cabello, G., Wu, D.-Y. & Tian, Z.-Q. Surface-enhanced Raman spectroscopy toward application in plasmonic photocatalysis on metal nanostructures. *Journal of Photochemistry and Photobiology C: Photochemistry Reviews* **21**, 54-80 (2014).

3 Yu, P. *et al.* Giant Optical Pathlength Enhancement in Plasmonic Thin Film Solar Cells Using Core-shell Nanoparticles. *Journal of Physics D: Applied Physics* (2018).

4 Wang, J., Jia, S., Cao, Y., Wang, W. & Yu, P. Design principles for nanoparticle plasmon-enhanced organic solar cells. *Nanoscale research letters* **13**, 211 (2018).

5 Yu, P. *et al.* Effects of plasmonic metal core-dielectric shell nanoparticles on the broadband light absorption enhancement in thin film solar cells. *Scientific reports* **7**, 7696 (2017).

6 West, P. R. *et al.* Searching for better plasmonic materials. *Laser & Photonics Reviews* **4**, 795-808 (2010).

7 Tang, Y., Huang, Y., Qv, L. & Fang, Y. Electromagnetic Energy Redistribution in Coupled Chiral Particle Chain-Film System. *Nanoscale research letters* **13**, 194 (2018).

8 Wang, W. *et al.* Size-dependent longitudinal plasmon resonance wavelength and extraordinary scattering properties of Au nanobipyramids. *Nanotechnology* (2018).

9 Huang, J.-S. & Yang, Y.-T. Origin and future of plasmonic optical tweezers. *Nanomaterials* **5**, 1048-1065 (2015).

10 Juan, M. L., Gordon, R., Pang, Y., Eftekhari, F. & Quidant, R. Self-induced back-action optical trapping of dielectric nanoparticles. *Nature Physics* **5**, 915 (2009).

11 Mestres, P., Berthelot, J., Aćimović, S. S. & Quidant, R. Unraveling the optomechanical nature of plasmonic trapping. *Light: Science & Applications* **5**,

e16092 (2016).

12 Ndukaife, J. C. *et al.* Photothermal heating enabled by plasmonic nanostructures for electrokinetic manipulation and sorting of particles. *ACS nano* **8**, 9035-9043 (2014).

13 Kang, Z., Chen, J., Wu, S.-Y. & Ho, H.-P. Plasmonic absorption activated trapping and assembling of colloidal crystals with non-resonant continuous gold films. *RSC Advances* **5**, 105409-105415 (2015).

14 Kang, Z. *et al.* Trapping and assembling of particles and live cells on large-scale random gold nano-island substrates. *Scientific reports* **5**, 9978 (2015).

15 Chen, J., Kang, Z., Kong, S. K. & Ho, H.-P. Plasmonic random nanostructures on fiber tip for trapping live cells and colloidal particles. *Optics letters* **40**, 3926-3929 (2015).

16 Roxworthy, B. J., Bhuiya, A. M., Vanka, S. P. & Toussaint Jr, K. C. Understanding and controlling plasmon-induced convection. *Nature communications* **5**, 3173 (2014).

17 Tsuboi, Y. *et al.* Optical trapping of quantum dots based on gap-mode-excitation of localized surface plasmon. *The Journal of Physical Chemistry Letters* **1**, 2327-2333 (2010).

18 Roxworthy, B. J. *et al.* Application of plasmonic bowtie nanoantenna arrays for optical trapping, stacking, and sorting. *Nano letters* **12**, 796-801 (2012).

19 Shoji, T. & Tsuboi, Y. Plasmonic optical tweezers toward molecular manipulation: tailoring plasmonic nanostructure, light source, and resonant trapping. *The journal of physical chemistry letters* **5**, 2957-2967 (2014).

20 Ndukaife, J. C. *et al.* Long-range and rapid transport of individual nano-objects by a hybrid electrothermoplasmonic nanotweezer. *Nature nanotechnology* **11**, 53 (2016).

21 Kotsifaki, D. G., Kandyla, M. & Lagoudakis, P. G. Plasmon enhanced optical tweezers with gold-coated black silicon. *Scientific reports* **6**, 26275 (2016).

22 Wu, M. *et al.* In situ growth of matchlike ZnO/Au plasmonic heterostructure for enhanced photoelectrochemical water splitting. *ACS applied materials & interfaces* **6**, 15052-15060 (2014).

23 Kim, H. M., Youn, J. R. & Song, Y. S. Hydrodynamic fabrication of structurally gradient ZnO nanorods. *Nanotechnology* **27**, 085704 (2016).

24 Lemoine, F., Antoine, Y., Wolff, M. & Lebouche, M. Simultaneous temperature and 2D velocity measurements in a turbulent heated jet using combined laser-induced fluorescence and LDA. *Experiments in fluids* **26**, 315-323 (1999).

25 Mangalgiri, G. M., Manley, P., Riedel, W. & Schmid, M. Dielectric Nanorod Scattering and its Influence on Material Interfaces. *Scientific reports* **7**, 4311 (2017).

26 Gwo, S., Chen, H.-Y., Lin, M.-H., Sun, L. & Li, X. Nanomanipulation and controlled self-assembly of metal nanoparticles and nanocrystals for plasmonics. *Chemical Society Reviews* **45**, 5672-5716 (2016).

27 Govorov, A. O. & Richardson, H. H. Generating heat with metal nanoparticles. *Nano today* **2**, 30-38 (2007).

28 Rusconi, R., Isa, L. & Piazza, R. Thermal-lensing measurement of particle thermophoresis in aqueous dispersions. *JOSA B* **21**, 605-616 (2004).

29 Chen, J. *et al.* Thermal gradient induced tweezers for the manipulation of particles and cells. *Scientific reports* **6**, 35814 (2016).

30 Helden, L., Eichhorn, R. & Bechinger, C. Direct measurement of thermophoretic forces. *Soft matter* **11**, 2379-2386 (2015).

31 Putnam, S. A., Cahill, D. G. & Wong, G. C. Temperature dependence of thermodiffusion in aqueous suspensions of charged nanoparticles. *Langmuir* **23**, 9221-9228 (2007).

32 Würger, A. Thermal non-equilibrium transport in colloids. *Reports on Progress in Physics* **73**, 126601 (2010).

33 Vigolo, D., Buzzaccaro, S. & Piazza, R. Thermophoresis and thermoelectricity in surfactant solutions. *Langmuir* **26**, 7792-7801 (2010).

34 Eslahian, K. A., Majee, A., Maskos, M. & Würger, A. Specific salt effects on thermophoresis of charged colloids. *Soft Matter* **10**, 1931-1936 (2014).

Chapter 4.

Plasmon-enhanced Light Harvesting System

4.1. Introduction

We are facing a major energy crisis due to the decline in the amount of fossil fuels. In this situation, solar energy has been used as an alternative energy source which is environmentally sustainable. Especially, biological photovoltaics (BPV) so-called "living solar cell" has emerged as a promising technology for producing electricity from the photosynthetic organisms that convert solar energy to chemical energy by photosynthesis. Cyanobacteria, one of the photosynthetic organisms, has the same electron transport chain as the plant. They produce electrons using water, light, and carbon dioxide, and emit electrons to the outside through a type IV pili which is highly conductive[1]. In BPV, the electrons generated from the photosynthetic bacteria can be transferred to the anode and then the cathode through an external electrical circuit, thus electricity can be generated. At the same time, the hydrogens secreted from cells pass through the proton exchange membrane (PEM) and move to the anode chamber, where the two electrons are combined with the protons and oxygen to convert water at the cathode.

The advantages of BPV have been reported for the following reasons: (1) BPV produces electricity during both light and dark period, while photovoltaics (PV) produce electricity only during light period[2]. (2) BPV produces power from solar energy using only water as an electron source, while microbial fuel cell (MFC) use heterotrophic bacteria to produce the chemical energy stored in organic matter[3]. (3) BPV can directly harness the photosynthesis which has a high quantum efficiency. (4) BPV relies on living organisms as self-healing which is different from other (semi-)PV. (5) The cost of producing a micro solar cell could be low since photosynthetic bacteria are abundant and

environmental friendliness. Therefore, BPV has inherently promising technology for renewable energy generation.

To increase the solar energy conversion efficiency, most of current researches are focused on setting the cells physically close to the electrode by gravity. Bombelli *et al*.[4] allowed the cells to be settled on the electrode for 12h to facilitate biofilm for reducing electrochemical potential losses. In addition, Bombelli *et al*.[5] developed a microfluidic device-based BPV that operate without any membrane or mediator. They permitted cells to settle on the anode for 24h after injection, which resulted in high power density above 100 mW/m^2. Moreover, Sekar *et al*. designed the cells to be immobilized on a carbon nanotube (CNT) modified electrode for the purpose of enhancing the direct electron transfer[6]. However, these approaches have the disadvantage of being time consuming. Therefore, a different strategy is required for the improvement of the BPV performance.

In a recent research, a combined system of MFC and PV has been developed[7]. Qian *et al*. reported a solar-assisted microbial photoelectrochemical system which consisted of hematite nanowire-arrayed photoelectrode, and *Shewanella oneidensis* MR-1. The increased photocurrent was attributed to both the MR-1 cells and photoanode. The MR-1 cells generated electricity by consuming organic matter, and the hematite photoanode produced electrons by water splitting. Moreover, cells thrived on the surface of the electrode and the morphology of the cells was stable. Meanwhile, our previous work[3] reported the improved power generation system by combining BPV and nanoparticle. Boosted power efficiency of BPV was achieved by only using light and water through a long electron transfer conduit to the electrode.

Recently, enhanced cultivation methods of photosynthetic organisms were reported by utilizing the wavelength specific back scattering from the metal nanoparticles due to the localized surface plasmon resonance (LSPR) effect[8,9] or by shifting the UV-A radiation to blue light by fluorescent material[10]. LSPR is the localized resonant oscillation of plasmon arose from a strong coupling between light and the abundant free electrons in the metal nanoparticle, which has a considerable potential in energy issue due to its characteristic decay mechanisms that include the far-field scattering effect[11]. Anyhow, those two approaches have a common purpose in the way of enhancing the specific wavelength range of the light source which is the favorable spectral region for the photosynthetic

organisms growth.

In this respect, a great strategy can be established to further improve the performance of the combined BPV-PV system. That strategy is to fully exploit the broadband wavelength (300-700 nm) of the light, including to enhance the favorable spectral region (390-500 nm and 600-700 nm) for photosynthesis of cells, for generating the electrical energy with high efficiency. This broadband electricity production is expected to be feasible by introducing a photoelectrode made of a plasmonic hybrid nanostructure (semiconductor/metal).

Zinc oxide nanorods (ZnONRs) have recently got great attention as complementary structure in solar cells for increasing the light harvesting efficiency, due to the high light scattering effect in the visible wavelength range (390-700 nm) and thus the longer effective optical path length[12,13]. Moreover, ZnONRs is the preferred electrode for solar cells due to a wide and direct bandgap and high carrier mobilities[14]. Meanwhile, plasmonic-enhanced photovoltaic cells have been also actively studied to improve the energy conversion efficiency by using metal nanoparticles such as gold nanoparticles (AuNPs) and silver nanoparticles (AgNPs)[15,16]. As mentioned above, LSPR can be decayed via characteristic decay mechanism such as near-field enhancement, far-field scattering, hot-electron injection (or plasmonic induced charge separation, PICS), plasmon-induced resonant energy transfer (PIRET) and plasmonic heating. In the sense, plasmonic-enhanced BPV-PV (ZnONRs/metal NPs/Cells) can take advantage of PICS, far-field scattering and near-field enhancement aided by the hybrid nanostructure, for increasing the current production.

In this study, an anomalously enhanced bioinorganic photovoltaic cell was successfully demonstrated based on the broadband multiplex living solar cell (ZnONRs/AuNPs/Cells) system, by making the best use of the hybrid nanostructure (ZnONRs/AuNPs) as an electric energy boosting photoanode. In our system, electrons were generated in multiple paths including (i) the photosynthesis of the cells (390-500 nm, 600-700 nm) (ii) intraband transition in AuNPs due to the LSPR (around 520 nm), and interband transition in (iii) ZnONRs (below 364 nm) in the almost full spectral range of the light source (300-800 nm), which led to the highly efficient system (Fig. 4.1.1). Furthermore, the photosynthetic activities of the cells were extremely enhanced with the effect of the

strong far-field scattering from ITO/ZnONRs and ITO/ZnONRs/AuNPs, compared to bare ITO anode. The far-field scattering effects of the nanostructures were confirmed both by conducting 3D numerical analysis of electromagnetic field and by measuring the scattered light for the three different anode structures. It is noteworthy that the introduced novel broadband multiplex living solar cell would enable to enhance solar energy harvesting efficiency.

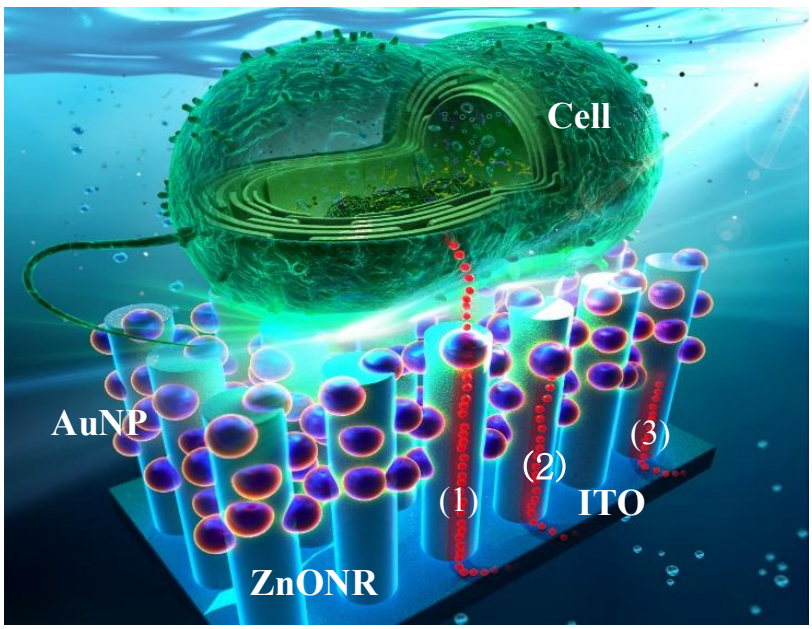

Figure 4.1.1. Schematic illustration of the broadband multifunctional living solar cell proposed in this study. Photocurrents are generated from multiple mechanism simultaneously : (1) the photosynthesis of the cell, (2) hot-electron generation from AuNPs (PICS), and (3) interband transition in ZnONRs.

4.2. Experimental Section

4.2.1. Preparation of plasmonic anodes

ITO/ZnONRs anode was fabricated by using the hydrothermal growth of ZnONRs on the ITO glass and then ITO/ZnONRs/AuNPs anode was fabricated by the following photochemical reduction of AuNPs on the surfaces of ZnONRs of ITO/ZnONRs anode. Details on the processes are explained in literature[17,18]. Briefly, the hydrothermal growth was conducted in two steps, seeding and growth. First, a glass substrate was cleaned with acetone, DI water and isopropyl alcohol in order. For the seeding step, seed solution (zinc acetate ($Zn(C_2H_3O_2)_2$) dissolved in ethanol, 0.03 M) was spin-coated on the ITO glass three times at 2000 rpm for 10 s, followed by annealing at 250 °C for 20 min to remove residual solvent and form crystal seeds. For the growth step, the seed-coated ITO glass was immersed in the growth solution (zinc nitrate hexahydrate ($Zn(NO_3)_2 \cdot 6H_2O$) and hexamethylenetetramine ($C_6H_{12}N_4$) dissolved in DI water, 0.03 M) at 90 °C for 2 h and rinsed several times. Then, for the photochemical reduction, ITO/ZnONRs was immersed in chloroauric acid ($HAuCl_4$) aqueous solution (3 mM) and irradiated with an UV lamp (UVT series, DongSeo, Chungnam, Korea) for 2 h.

4.2.2. Preparation of cell solution and MEA

A wild-type strain of *Synechocystis* sp. PCC 6803 (subsequently called *Synechocystis*) was grown on 1% BG-11 agar plate buffered with 0.3% (w/v) sodium thiosulphate ($Na_2S_2O_3$) at 28 °C for 2 weeks. Then, the cells were re-suspended in 1% BG-11 freshwater solution (C3061, Sigma Aldrich). *Synechocystis* is well known as a coccoid cyanobacterium (Fig. 4.2.1). The cell is a rod-shaped, and its size generally varies from 1 to 3 μm.

The Nafion 117 membrane (274674, Sigma Aldrich) was stored in 0.5 M hydrogen peroxide (H_2O_2) at 80 °C for 1h, then soaked with 80 °C DI water. It was stored in 0.5 M sulfuric acid (H_2SO_4) at 80 °C for 1 h, and rinsed with 80 °C DI water. Platinum was

sputtered onto the carbon cathode about 200 nm thick to introduce high catalytic activity. After then, the membrane and Pt-coated electrode were bonded to form a membrane electrode assembly (MEA) through the hot pressing process at 125 °C under the pressure of 5 MPa for 80 s.

4.2.3. Device assembly

The device consisted of three parts such as the photoanode, an anodic chamber, and the MEA as shown in the schematic image (Fig. 4.2.2). The size of the anodic chamber was 11 mm × 11 mm × 5 mm, and the photoanode was located at the bottom of the anodic chamber. The MEA was located between the anodic chamber and cathodic cover, and all the components were joined by bolts. The external electrical circuit was connected to the joined device to complete the circuit. Then, the anodic chamber was filled with the cell solution through a flexible tube (Tygon E-3603, ACF00001, Saint Gobain, Tokyo, Japan) connected to the sidewall of the chamber. In order to prevent drying, the flexible tubes were kept clamped throughout all experiments.

4.2.4. Electrochemical characterization

All electrochemical experiments were carried out at the room temperature using a potentiostat (VersaStat3, Princeton Applied Research, USA). The amperometric response was measured with the resistance of 510 Ω as a function of time under the alternative light and dark conditions.

A 150 W lamp (KLS 150H-RC-150E, Kwangwoo, Korea) was used as the light source for stimulating the photosynthetic activity of cells. The lamp provided the full spectrum of the visible light with strong intensity as shown in Fig. 4.2.3. The intensity of the light source was characterized using an integrating sphere (Labsphere Co., North Sutton, NH, USA) with 6 inch diameter monochromator (Acton Research Co., Acton, MA) that is attached to a photomultiplier tube (Hamamatsu Photonics K.K., Japan).

4.2.5. Angle-dependent light scattering measurement

Fig. 4.2.4 illustrates an experimental set-up of the angle-dependent light scattering measurement. The sample, the halogen lamp, and optical instruments were fixed on a motorized rotation stage. In this configuration, ZnONRs were vertically oriented on the sample substrate toward a detector of a spectrometer. The edge of the sample was illuminated using the halogen lamp, an aperture, a convex lens, and a slit. The spectrum of the light scattered by the sample was measured by the spectrometer (Maya 2000, Ocean Optics Inc.) with automatic rotation of the stage.

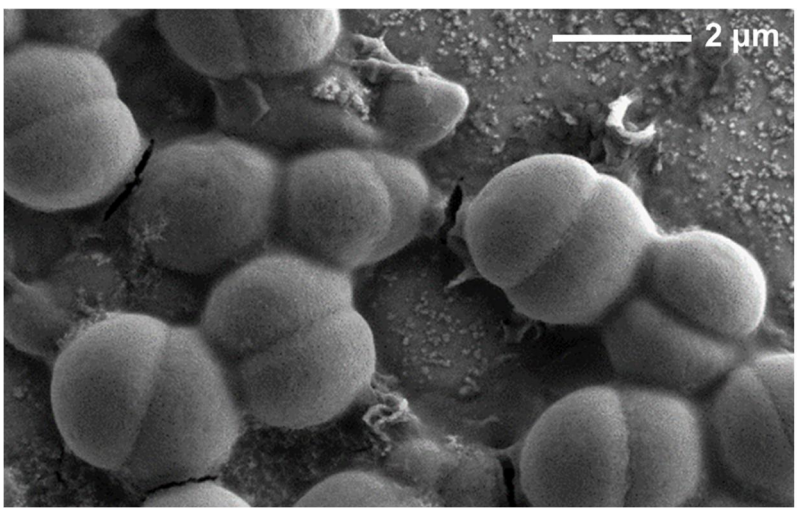

Figure 4.2.1. Characterization of the cell. Scanning electron microscopy (SEM) of Synechocystis sp. PCC 6803 showing two-partially fused spherical lobes in shape, about 1 to 3 µm in diameter. The scale bar denotes a length of 2 µm.

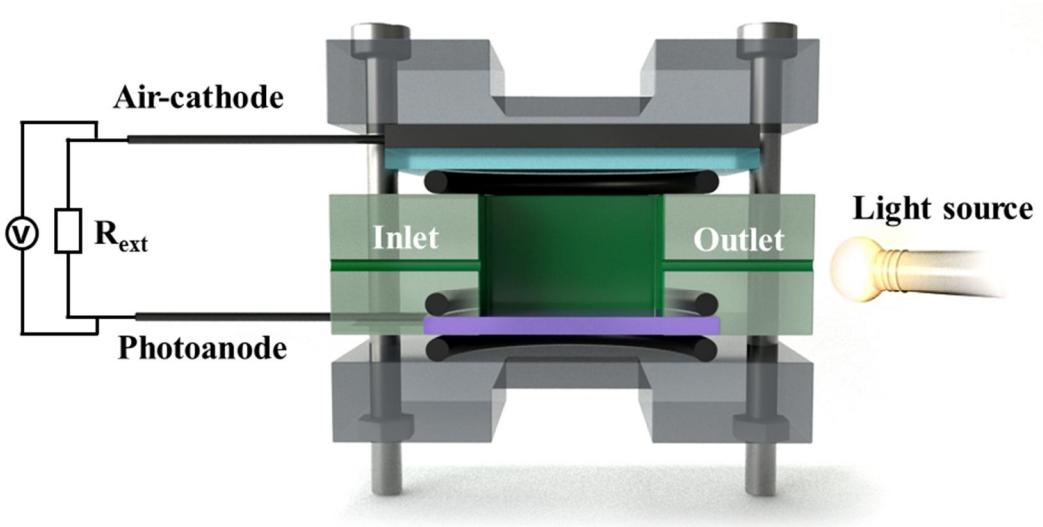

Figure 4.2.2. Schematic image of the device. The device is consist of three parts: a photoanode, an anodic chamber, and a MEA. The light is irradiated to the side of the anodic chamber with a intensity of 48.75 W/m^2.

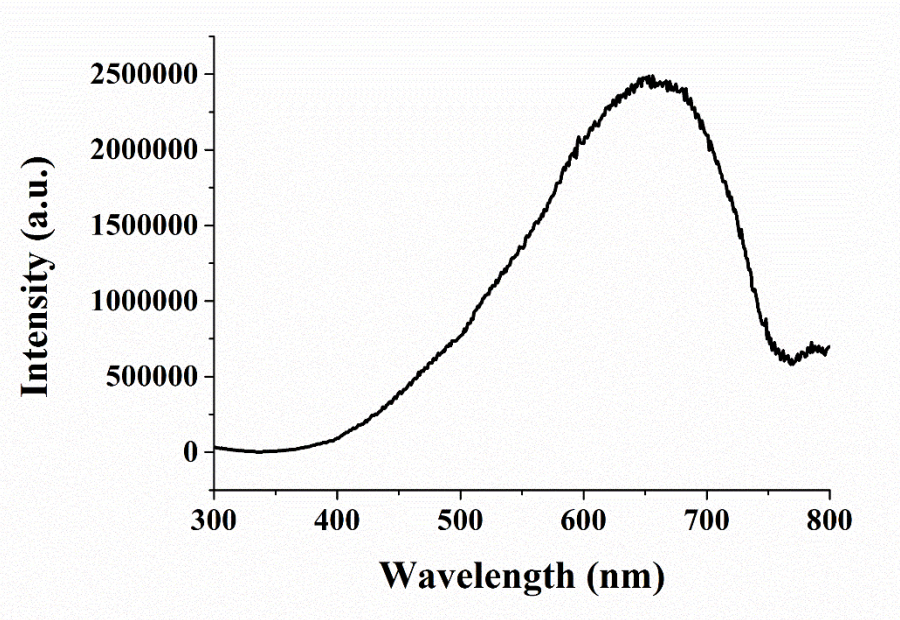

Figure 4.2.3. Irradiance spectrums of the halogen lamp used in this study. The light source provided a full spectrum of visible light for natural photosynthesis of Synechocystis sp. PCC 6803

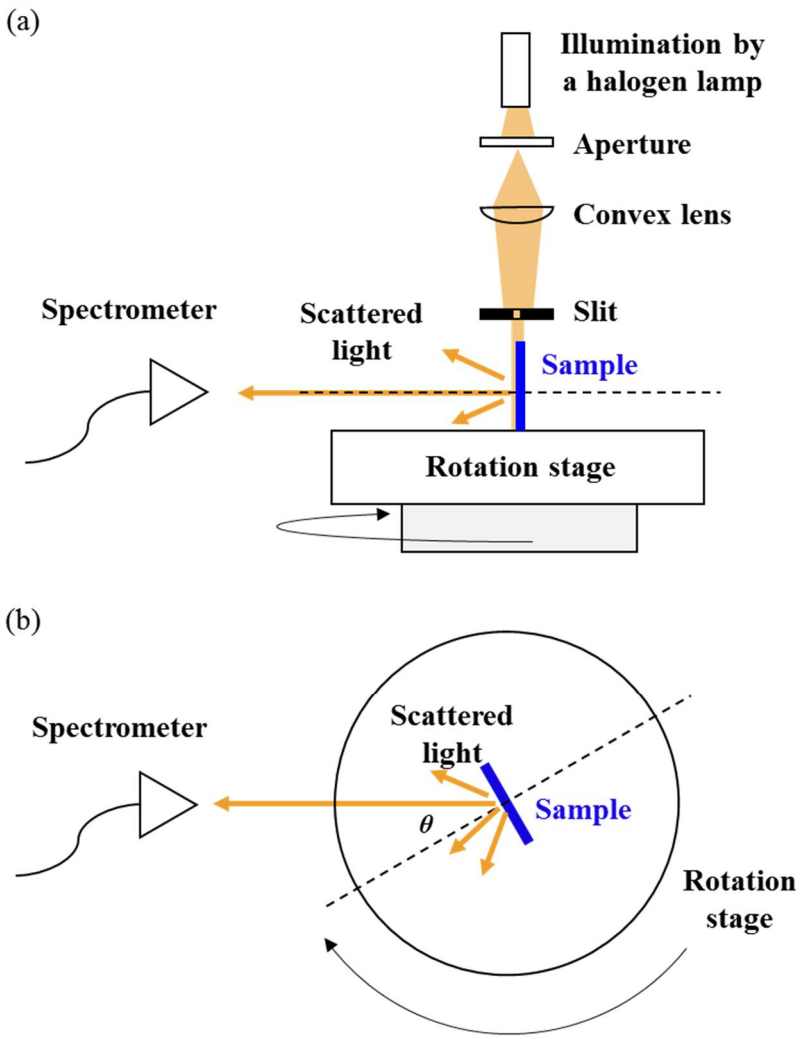

Figure 4.2.4. Schematic illustration of far-field scattering measurement. The schematic images show (a) side view and (b) top view of the optical set-up, respectively. The scattered light was detected by the spectrometer with respect to the rotating angles.

4.3. Numerical method

3D numerical simulation of electromagnetic field (EM) was carried out with simplified geometry to understand the enhancement in photocatalytic activities of the cells by using COMSOL multiphysics®[19]. 3D meshes used for the simulation are described in Fig. 4.3.1. The domain consists of ITO glass, ZnONRs and AuNPs, and water. For comparison, ITO glass with ZnONRs and bare ITO structures were also considered. The dimensions of the geometries were determined based on SEM images. The thickness of ITO is 200 nm. The diameter (d_{NR}) and length (l_{NR}) of the ZnONR were 80 nm and 800 nm, respectively, and the distance between the ZnONRs (D_{NR}) was set to same as d_{NR}. The diameters of AuNP is 30 nm.

The EM was calculated to obtain the far-field scattering distributions and the corresponding polar plots for the three different structures.

$$\nabla \times (\nabla \times \mathbf{E}) - k_0^2 \varepsilon_r \mathbf{E} = 0 \tag{4-9}$$

where ∇ is the nabla operator, $\mathbf{E}$ is the total electric field, k_0 is the free space wavenumber, and ε_r is the complex relative permittivity. It was assumed that an x-polarized 600 nm plane wave propagates in y-direction from y=0 plane. Periodic boundary condition was used in $\pm$x direction to consider a large number of nanostructures. Except for the periodic boundaries, the perfectly matched layer (PML) was taken into account as the boundary condition to avoid the reflection of wave at the outer boundaries.

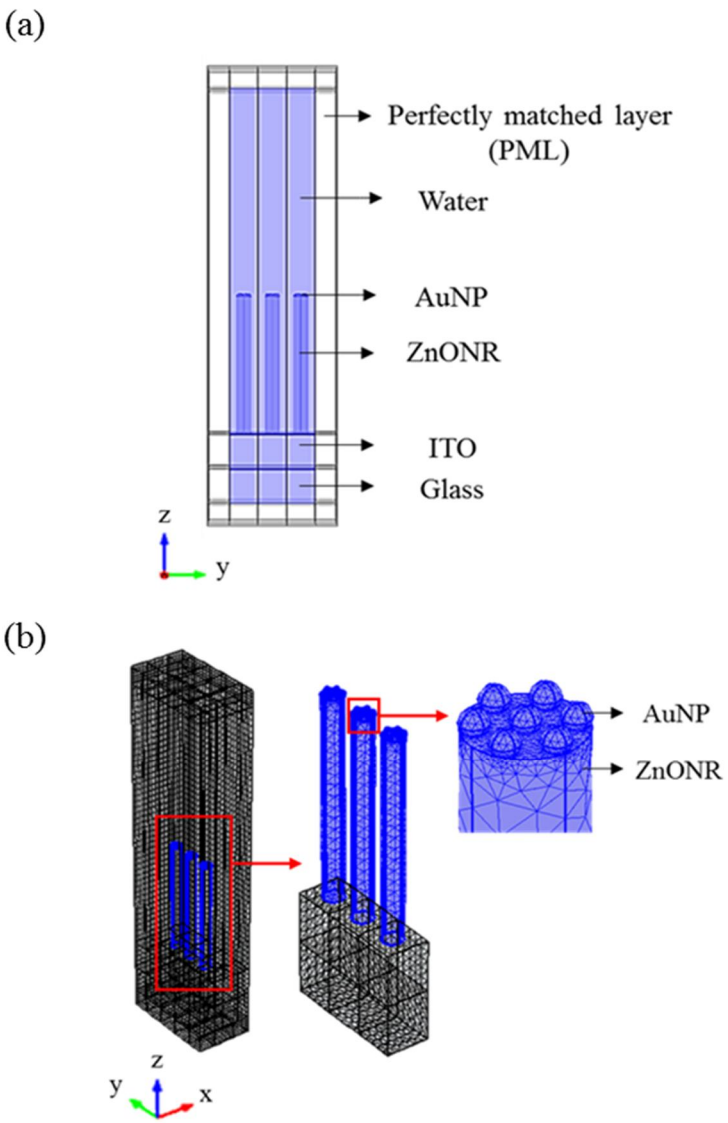

Figure 4.3.1. Geometries for numerical simulation. (a) Geometry and (b) meshes for the numerical simulation

4.4. Results and discussion

4.4.1. Characterization of the plasmonic anodes

The cross-section view of the SEM images for the fabricated ZnONRs and ZnONRs/AuNPs on the ITO glass are shown in Fig. 4.4.1 (a) and (b), respectively. The AuNPs are well-deposited on the surfaces of the ZnONRs, and the average diameter of the AuNPs is about 30 nm. The average diameter and length of the ZnONRs are about 80 nm and 800 nm, respectively. These values were used for constructing the geometric model for the numerical simulation. Absorption spectra of the photoanodes shown in Fig. 4.4.2(a) indicate that ZnONRs absorb great amount of the UV-region light due to their large band gap (3.4 eV)[17] and that AuNPs absorb great amount of the light around the resonance peak of 520 nm due to the LSPR phenomenon.

The X-ray diffraction patterns of pristine ZnONRs and ZnONRs decorated with AuNPs are shown in Fig. 4.4.2(b). The measurements were carried out to obtain the 2θ diffraction angle scans between 20° and 80° for multilayer structures deposited on ITO glass. It can be clearly seen that all diffraction peaks in the samples correspond to the standard diffraction of a hexagonal ZnO crystal (JCPDS 79-0206). The XRD patterns of corresponding ZnONRs exhibit reflection peaks at 31.66° (100), 34.46° (002), 36.37° (101), 47.67° (102) and 62.91° (103). For the ZnONRs/AuNPs, additional peaks corresponding to face-centred cubic Au structure ((1 1 1) and (2 0 0)) are clearly observed at 2θ = 38.25 and 45.34° [20,21]. From the XRD pattern, it can be inferred that the (002) peak for the microcrystallites of the ZnO grows preponderantly, which indicates ZnONRs preferred anisotropic growth along the [001] direction of the ITO substrate[22,23]. The crystallite size of AuNP was calculated from the broadening of XRD peak by using the Scherrer equation, and the diameter was about 30.89 nm. The result was in agreement with the SEM data.

The photoelectrochemical behaviors of the aforementioned two samples were also characterized under the alternate light–dark conditions as shown in Fig. 4.4.3. For the measurements, the electrodes were assembled in order as described in Fig. 4.2.3. It apparently demonstrates that the photo-induced currents drastically increase when the

light is on. The photocurrent behaviors are exhibited in three steps[24-26] : (i) The photo-induced currents increase drastically upon illumination due to the separation and quick transfer of photoinduced charges. (ii) The photo-induced currents decrease rapidly by the recombination of the photoinduced charges. (iii) The photo-induced currents reach a steady state where the balance between the generation and the recombination of the photogenerated charges is achieved. ZnONRs/AuNPs electrode shows enhanced amperometric response compared to ZnONRs electrode, which suggests that AuNPs increase the photoelectrochemical properties of ZnONRs under the light.

The enhanced photocurrent of ITO/ZnONRs/AuNPs electrode could be attributed to the increased visible light-harvesting efficiency via LSPR effect. In other words, this effect can be ascribed to the additional electrons injected from AuNPs to ZnONRs in the visible light region. The additional electrons can be generated in Au by two ways: (i) the intraband excitation (LSPR-induced hot electrons or Landau damping) in the conduction band, and (ii) the interband excitation from the d-band to the conduction band[27]. Intraband excitation occurs around the LSPR resonant wavelength and the efficient interband excitation generally needs the absorption of photon with energy above 2.4 eV (517 nm)[28]. When ZnO is in contact with Au, Schottky junction is formed at the interface. Typical Schottky barrier at ZnO-Au interface is only about 0.9 eV, which is similar to the light energy with wavelength of ~1377 nm[29]. In the meantime, the LSPR-induced energetic electrons from Au have the sum energy of Fermi level and the incident photon[30]. Therefore, the electrons with higher energy than the Schottky barrier can be effectively separated from Au and be injected into the conduction band of the ZnO, which is called PICS[31]. The main contribution to the additional electrons is due to the LSPR-induced hot electrons, owing to the large energy difference between the d-band and the Fermi level (2.3 eV for Au) which requires much higher photon energy for interband excitation to overcome the Schottky barrier[32]. Moreover, plasmon-induced resonant energy transfer (PIRET) can produce the additional electrons as well, by transferring the excited LSPR energy from AuNPs to the semiconductor. In other words, LSPR decays by exciting e^--h^+ pairs in the semiconductor when the LSPR resonance band overlaps with the band edge of the semiconductor[30].

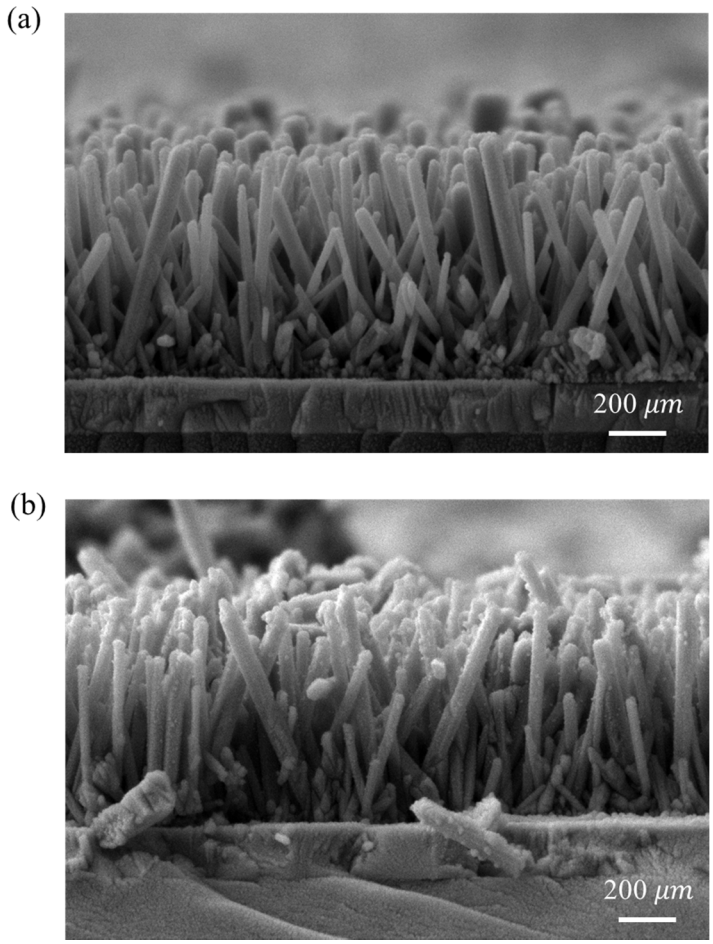

Figure 4.4.1. Characterization of the photoanode. SEM images of the fabricated (a) ZnONRs, and (b) ZnONRs/AuNPs.

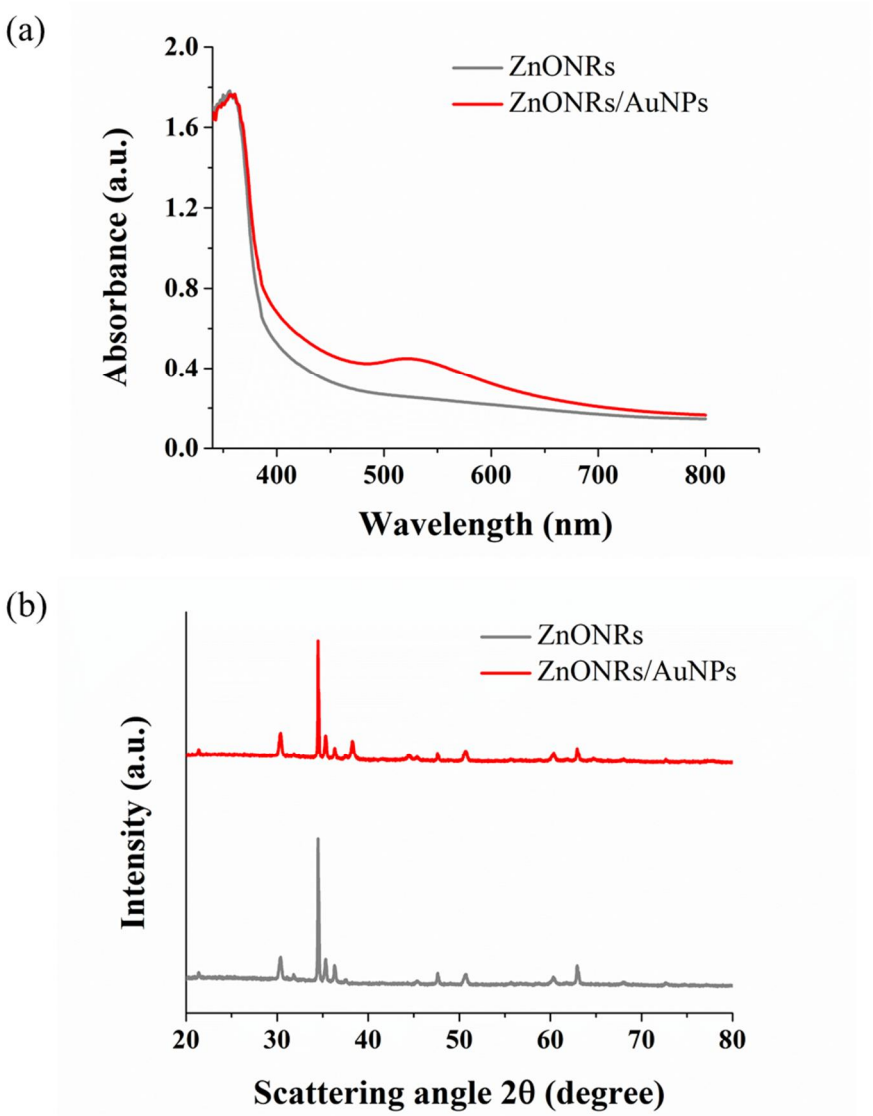

Figure 4.4.2. Characterization of the photoanode. (a) Absorption spectrum of the photoelectrodes: ZnONRs and ZnONRs/AuNPs. (b) X-ray powder diffraction (XRD) curves of the ZnONRs and ZnONRs/AuNPs grown on an ITO substrate.

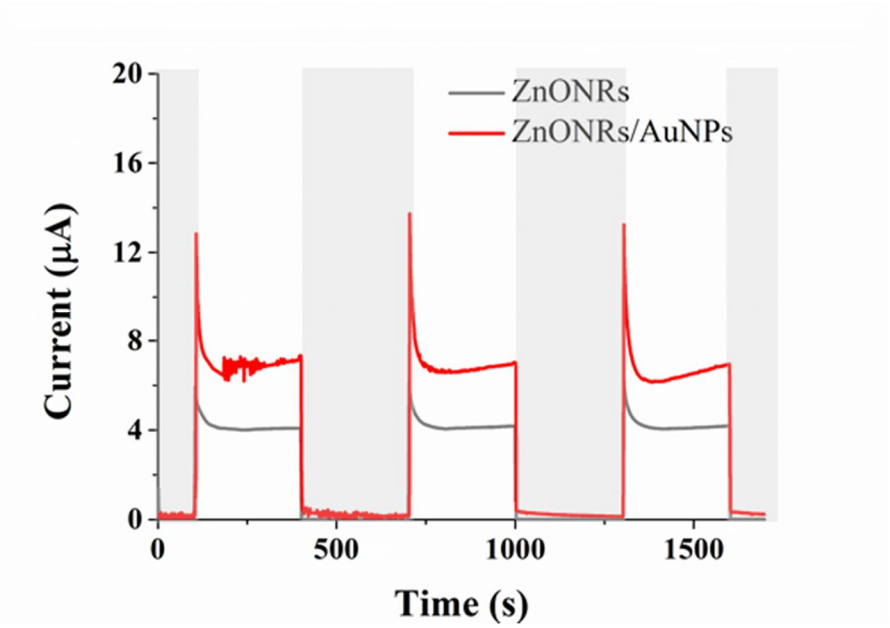

Figure 4.4.3. Electrochemical properties of fabricated photoanodes. Cyclic photo-response of the photoanode measured with a 510 Ω resistance in DI water. The light irradiation started when 100 s elapsed, and the measurement was made for 300s light/dark interval.

4.4.2. Living solar cell performance

For the photo-response measurements, a device loaded with *Synechocystis* was operated at the resistance of 510 Ω under the alternative light and dark conditions. Three different photoanodes were used and a bare ITO glass was firstly examined as a control to demonstrate the photo-activity of the *Synechocystis* (Fig. 4.4.4). During light–dark cycles, the dependence of the light on the electricity generation is displayed, suggesting that *Synechocystis* is capable of transporting electrons to exterior without any mediator. In contrast to PV, *Synechocystis* provide current during dark period as well, so-called 'dark current'[4]. The average dark and photo-response currents are about 426.4 nA and 264.4 nA, respectively. That is, *Synechocystis* enables sustainable current generation in both dark and light condition. Moreover, the intensity of the light source is appropriate for the *Synechocystis* to produce current, resulting from the stable current generation during alternative light and dark conditions.

Then, the abilities to generate electricity of the three different photoanodes are compared in Fig. 4.4.5. Distinct differences in current generation are observed for each the condition. In particular, there is a considerable difference depending on the presence of the cells. The obtained photo-induced currents without cells were about 6.4 and 4.3 μA for ZnONRs/AuNPs and ZnONRs electrodes, respectively. In the presence of cells, the photo-response current was achieved about 1.28 and 7.3 for ZnONRs/AuNPs and ZnONRs electrodes, respectively. It is apparently demonstrated that the hybrid structure provides benign spectral regions for *Synechocystis* to improve the current generation during photosynthesis.

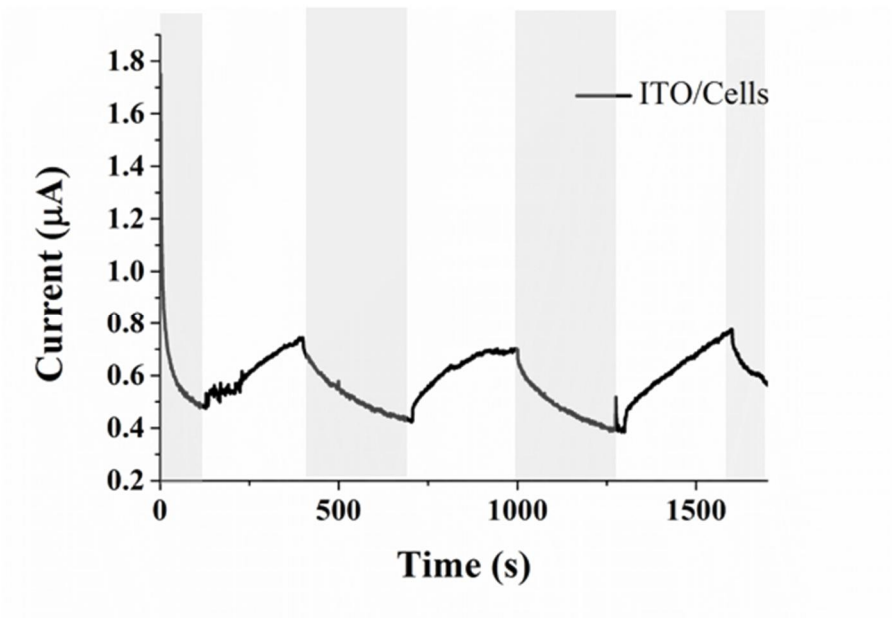

Figure 4.4.4. Bio-photoelectrochemical behavior of the bio-photovoltaic device loaded with *Synechocystis* sp.. Cyclic photo-response of the cyanobacteria flow cell measured with a 510 Ω resistance. The light irradiation started when 100 s elapsed, and the measurement was made for every 300s light/dark interval.

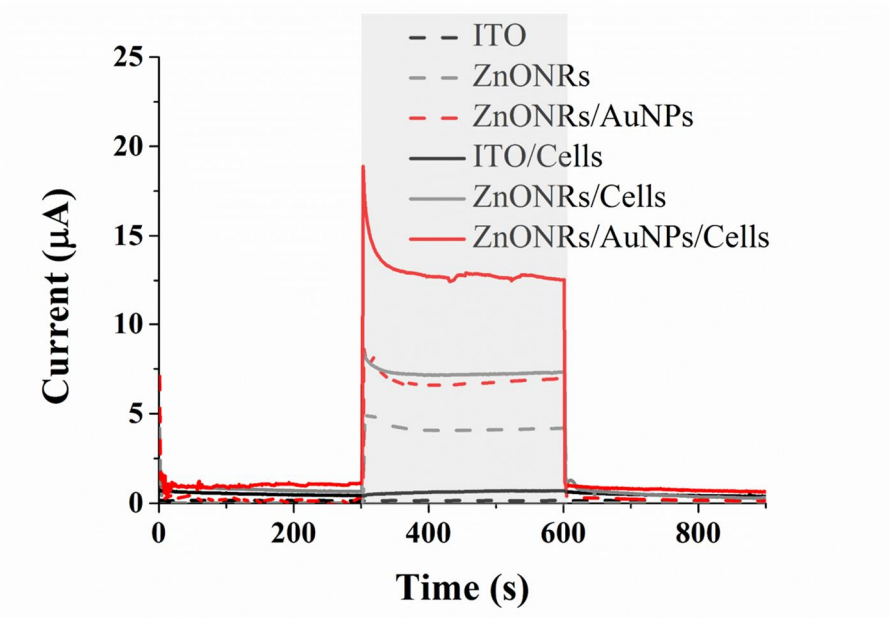

Figure 4.4.5. Bio-photoelectrochemical behavior of the electrochemical cell. Cyclic photo-response of the cyanobacteria flow cell measured with a 510 Ω resistance. The light irradiation started when 300 s elapsed, and the measurement was made under a 300 s light – 300 s dark cycle.

4.4.3. Working mechanism of plasmon-enhanced living solar cell

As mentioned above, the electrons were generated in multiple paths in our broadband multiplex living solar cell. The paths include the photosynthesis of the cells, LSPR-induced hot electron injection and interband transition in ZnONRs. The possible electron flows are represented with the arrows in a schematic energy band diagram (Fig. 4.4.6), where the midpoint redox potential of ferredoxin of the *Synechocystis* sp. and the typical energy levels of Au, ZnO and ITO were used for the energy band structure[29,33]. With the irradiation, the photogenerated electrons in the cells can be injected into AuNPs or into ZnONRs directly. Meanwhile, the LSPR-induced hot carriers in AuNPs with higher energy than Schottky barrier height can be injected into the conduction band of ZnONRs and be separated efficiently through the PICS. The other path is through the direct interband excitation of valence electrons in ZnONRs. Therefore, all the electrons generated from cells and photoelectrode can be subsequently transferred to the external circuit.

The one of the main reasons for the power enhancement is pigment accumulation of photosynthetic organisms due to photoanode. *Synechocystis* have two elemental chlorophyll (Chl) pigments, mainly chlorophyll a (Chl a) and chlorophyll b (Chl b). In general, Chl a is located in Photosystem I and Photosystem II, while Chl b located within the antenna complex[9]. Chl a absorbs the violet blue - blue wavelengths of light (*ca.* 390 - 450 nm) and orange to far-red (*ca.* 600 - 700 nm), whereas Chl b absorbs violet blue to green blue light (*ca.* 390 - 500 nm) and yellow to red light (*ca.* 600 nm - 680 nm).

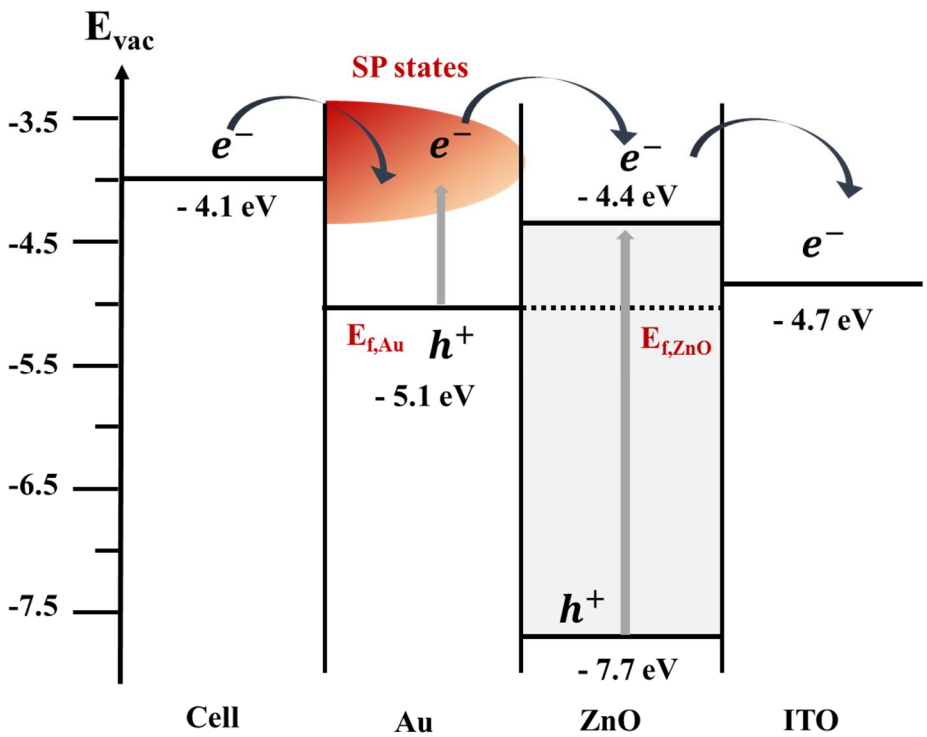

Figure 4.4.6. Photo-electrochemical performance of the broadband multifunctional living solar cell. Schematic energy band diagrams of the photoanode complex for electron transfer. The arrows in the figure indicate possible flow of electrons.

4.4.4. Broadband multiplex living solar cell

In the meantime, the working spectral range of the light source is different for each path due to the different origin of the photogenerated electrons. The schematic diagram in Fig. 4.4.7 exhibits the working mechanisms with respect to the wavelength. As expected with the strategy, our combined system is being activated at almost full spectrum of the light source including ultraviolet and visible ranges by utilizing both biophotovoltaic and photovoltaic effects simultaneously. To sum up the diagram, *Synechocysti*s is actively working at the two favorable visible regions (390 - 500 nm and 600 - 700 nm) due to the two elemental chlorophyll (Chl) pigments. The photosynthetic activity is exceptionally enhanced, aided by the light trapping and the far-field scattering throughout the suspended cells by the hybrid plasmonic photoanode. Moreover, ZnONRs and AuNPs harvest the light energy at the ultraviolet region (below 364nm) and the *Synechocysti*s-inactive visible region (around 520 nm) through the interband excitation and the Landau damping of LSPR, respectively.

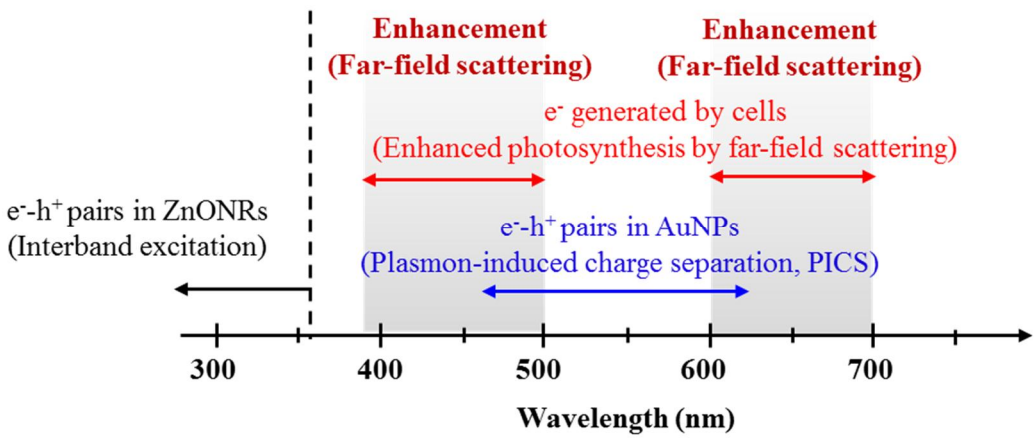

Figure 4.4.7. Broadband multifunctional living solar cell. The schematic diagram describing the working mechanisms of the hybrid plasmonic photoanode for the electron generation with respect to the wavelength.

4.4.5. Far-field scattering effect

4.4.5.1. Structural effect

Generally, ZnONRs demonstrate the high light scattering effect in the full visible wavelength range (390 – 700 nm) due to its high dielectric constant and AuNPs also give the far-field scattering effect. In this regard, the nanostructured photoanode can provide the enhanced light energy in the favorable spectral regions for Synechocystis to boost the current generation with the photosynthesis. Therefore, the far-field scattering effects by the nanostructures were investigated (Fig. 4.4.8). Figure. 4.4.8 shows the numerically obtained enhancement distribution of the scattered electric fields (E/E0) for the three different simplified structures of the photoanodes. The results convince that the far-field scattering is increasing in the order of ITO, ZnONRs and ZnONRs/AuNPs, which is coincident well with the photo-electrochemical performance of the device. Since the cells are located around the top of the photoanode in the system, the increased light scattering toward the far-field in the positive z-direction can definitely improve the photosynthetic activity of the cells by trapping the transmitted light through the cells. More intuitive comparison for the far-field scattering effect are shown in Fig. 4.4.9(a) and 4.4.9(b), which show the polar plot of the far-field scattering by each photoanode obtained with the simulation and measurement, respectively, when the wavelength is 600 nm. Both results reveal that ZnONRs basically highly enhance the light scattering in the positive z-direction and AuNPs further enhance the scattering as one of the LSPR decay mechanism. Meanwhile, bare ITO show almost negligible scattering effect compared to ITO/ZnONRs and ITO/ZnONRs/AuNPs. For this reason, the hybrid plasmonic photoanode (ITO/ZnONRs/AuNPs) manifested the best performance in the photocurrent generation. The discrepancy between the results of the simulation and measurement is arose from the simplified and ordered simulation geometry compared to the rather disordered real nanostructure. The scattering tendencies with respect to the wavelength were also measured to certainly confirm the working spectral range of the photoanodes for the light trapping (Fig. 4.4.10). Fig. 4.4.10 verifies that the two nanostructured photoanodes are beneficial to the far-field scattering in the overall spectral range contrary to the bare ITO. For the further investigation, the whole spectra of the scattered light by the photoanodes

were plotted as well (Fig. 4.4.11(a)). Since the amount of scattering is directly affected by the light source intensity, the measured scattering intensity was divided by the light source intensity for the fair comparison between ZnONRs and ZnONRs/AuNPs (Fig. 4.4.11(b)). The results show that ZnONRs acts as the great scatterer in the full visible wavelength range and AuNPs further amplify the light scattering of the incident light over the whole wavelength, especially over the preferential spectral region for the photosynthesis of the cell, as expected. Those scattering effects can be basically explained with the Mie scattering by the ZnONRs and AuNPs, and the further enhancement of scattering by ZnONRs/AuNPs compared to ZnONRs can be explained with LSPR-induced far-field scattering by AuNPs. In the meantime, the intensity of the scattered light by the bare ITO is extremely low like the noise level, so the result is not plotted.

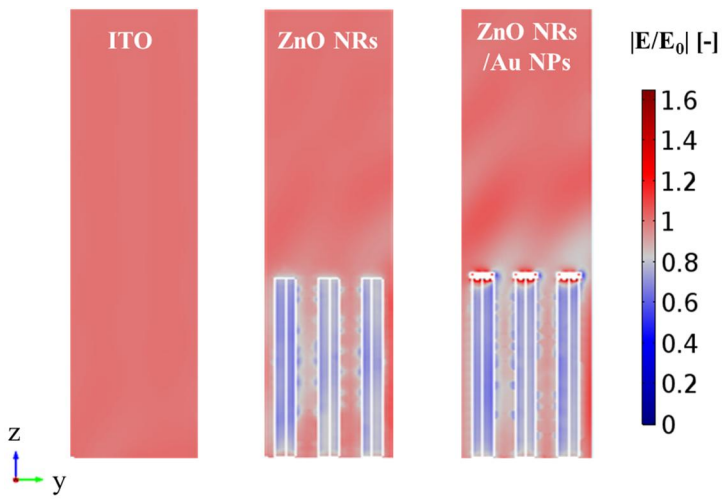

Fig 4.4.8. The effect of the hybrid structure. The enhancement distribution of the scattered electric field for each electrode structure.

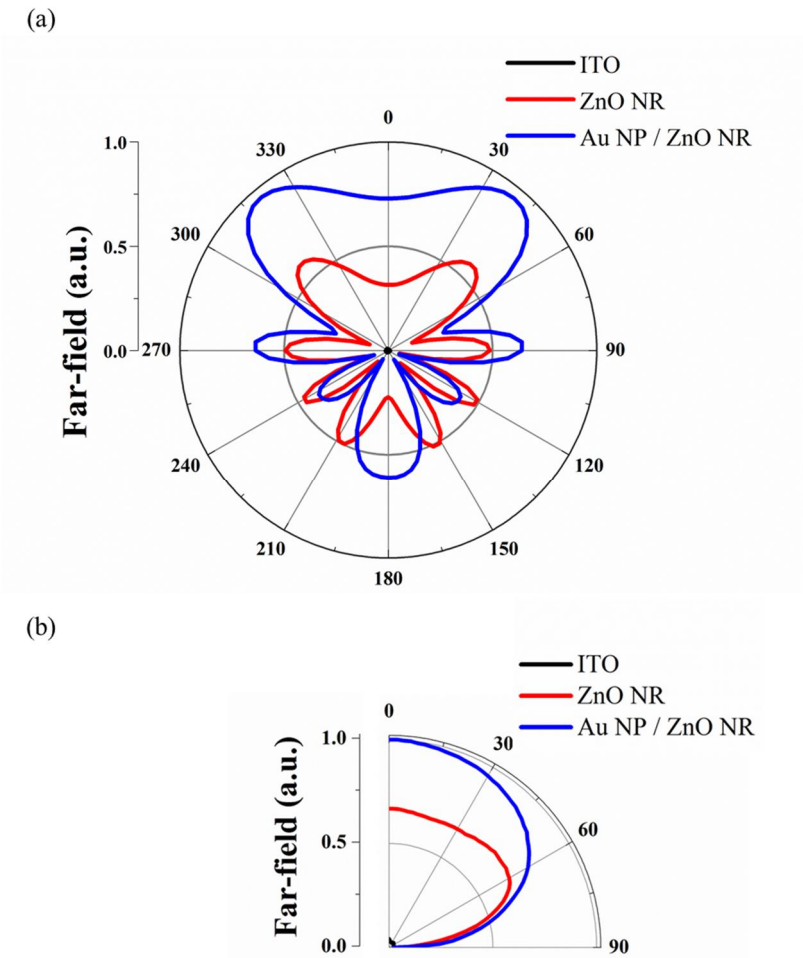

Fig 4.4.9. The effect of the hybrid structure. The polar plot of far-field scattering pattern in the xz-plane (y = 0) with respect to the three different electrode structures obtained from (a) simulation and (b) measurement.

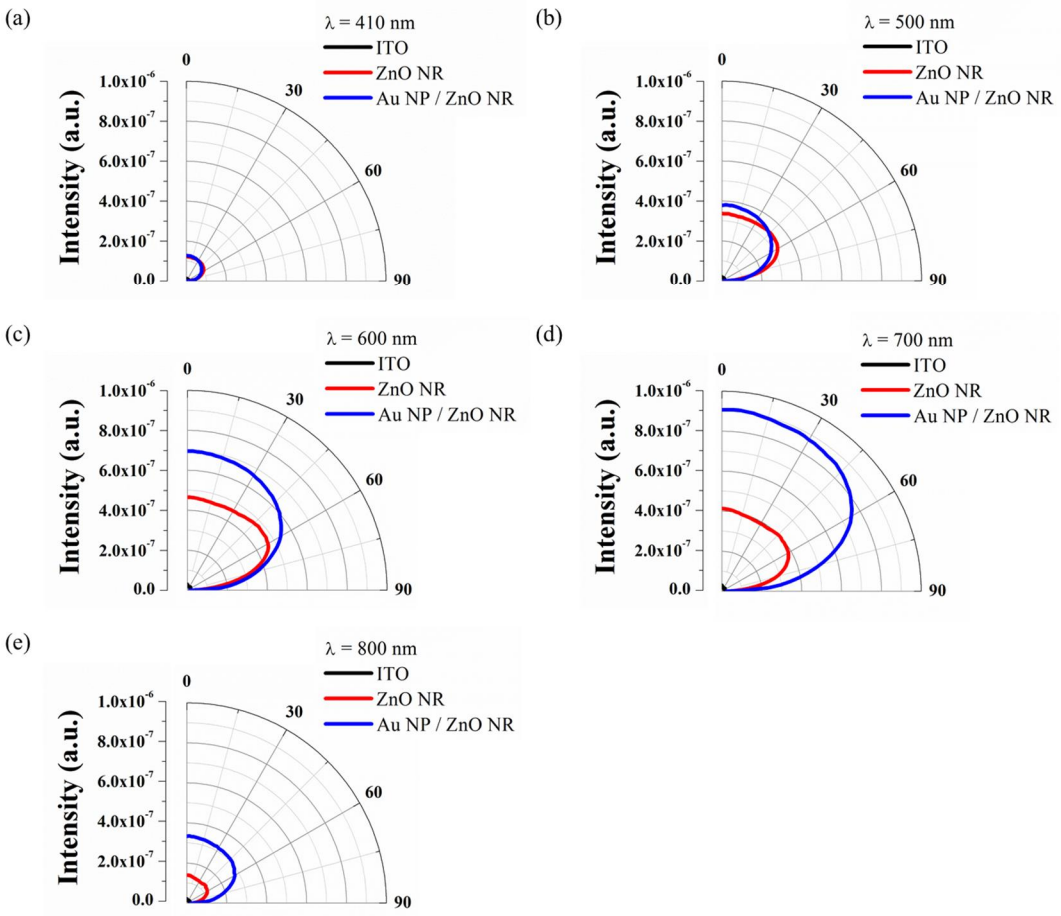

Fig 4.4.10. Polar plots with respect to structure and wavelength. Scattered light intensity by three different photoanode structures at the wavelength of (a) 410 nm, (b) 500 nm, (c) 600 nm, (d) 700 nm and (e) 800 nm respectively.

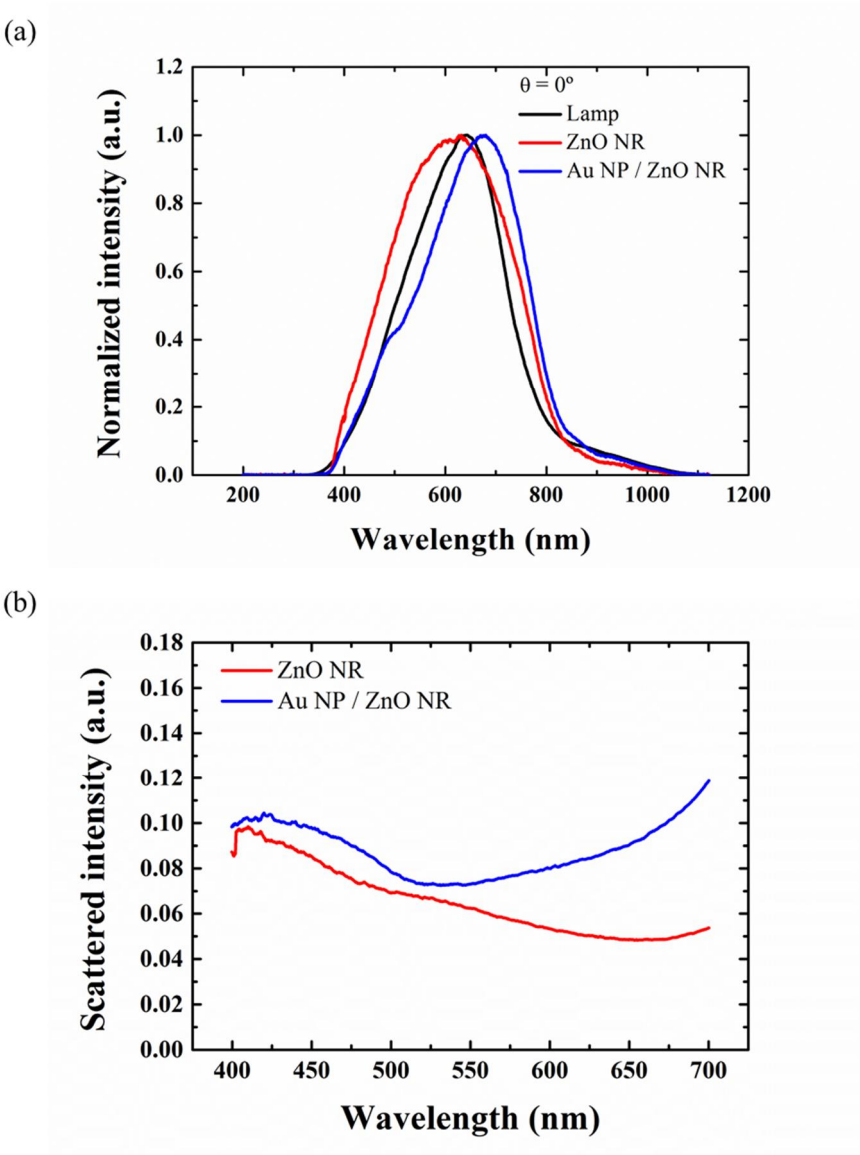

Fig 4.4.11. Far-field scattering effect depending on the wavelength. (a) Normalized intensity of the halogen lamp (black), and the scattered light by ZnONRs (red) and ZnONRs/AuNPs (blue) with respect to the wavelength. Notice that both ZnONRs and ZnONRs/AuNPs show far-field scattering effect in the full range of the light source. (b) Comparison of the scattered light intensity by ZnONRs/AuNPs and ZnONRs with respect to the wavelength. The light intensity was obtained by dividing each scattered light intensity by the halogen lamp intensity at each wavelength.

4.4.5.2. Size effect of AuNPs

Furthermore, the dependence of AuNP diameter (d) on the far-field scattering was numerically predicted (Fig. 4.4.12 and Fig. 4.4.13). AuNP geometries for the increased size reflected the mechanism of our fabricating method, photochemical reduction, which was based on the nucleation and growth of Au^0 on the surface of the ZnONR. The results predict that the far-field scattering cross-section increases as the diameter of AuNP increases, because the optical cross-section of AuNP increases. Therefore, it can be expected that the performance of the broadband multiplex living solar cell would increase with the increased diameter of AuNP unless AuNP gets bulky film. However, far-field scattering efficiency graph had a dip with d = 30 nm and was the highest with d = 10 nm. This is due to the relatively very small surface area in the case of d = 10 nm, even though the actual scattering cross-section is the lowest for the case.

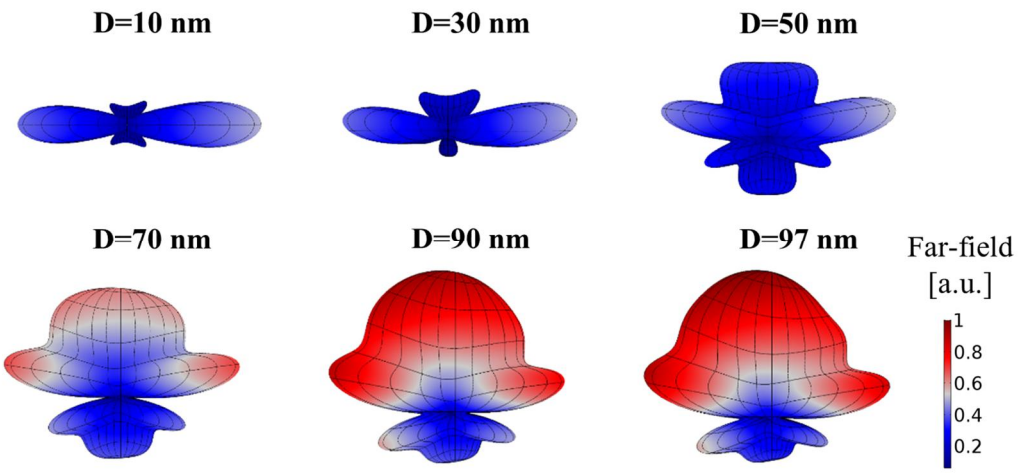

Fig 4.4.12. The size effect of AuNP. 3D plot of far-field scattering pattern with respect to the six different diameters of AuNP.

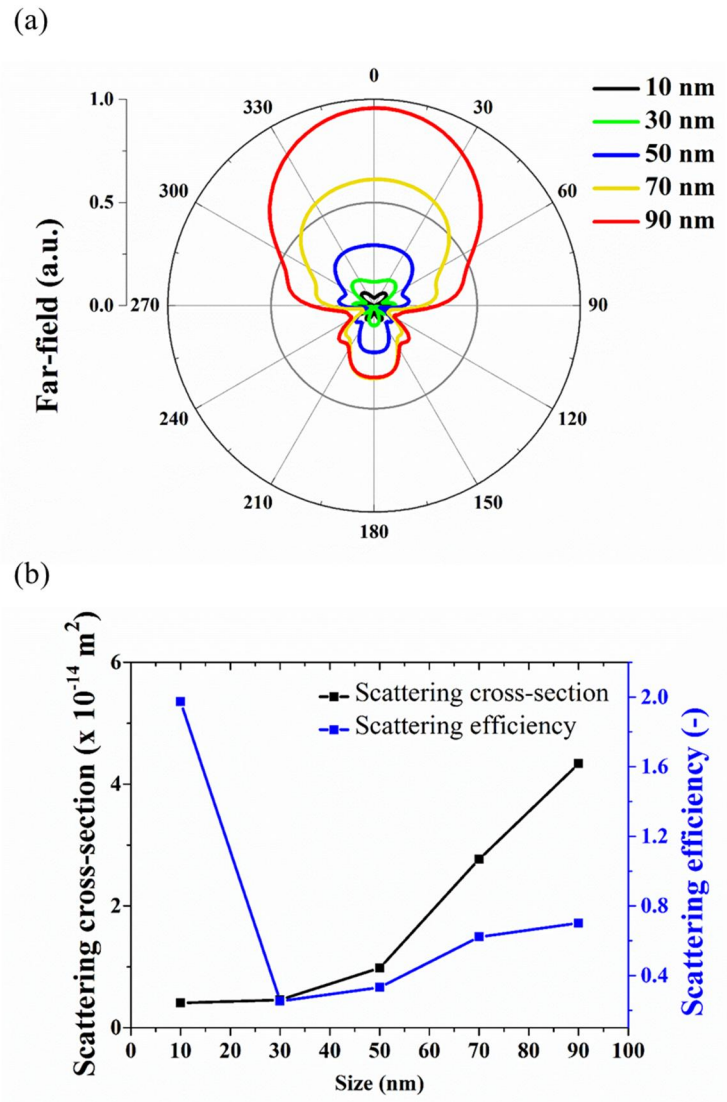

Fig 4.4.13. The size effect of AuNP. (a) Polar plot of far-field scattering pattern, and (b) far-field scattering cross-section and far-field scattering efficiency with respect to the six different diameters of AuNP.

4.5. Summary

In this study, we suggest a novel light harvester that consists of *Synechocystis* and ZnONRs/AuNPs. The robust photoactivity of *Synechocystis* was achieved with bi-functional electrode containing ZnONRs/AuNPs by accumulating favorable spectral region for the photosynthesis. In our system, the performance of living solar cell was extensively enlarged by both biophotovoltaic and photovoltaic effects. In accordance with the experimental results, the simulation results observed that ZnONRs enhanced the light scattering in the positive z-direction where the cell is placed. In addition, AuNPs further lift the far-field scattering aided by the LSPR effect. Moreover, the viability test confirmed that cell is viable onto the electrode even after operation. This unprecedented hybrid system would enable to introduce a new pathway of enhanced performance of the biophotovoltaics.

4.6. References

1 Lea-Smith, D. J., Bombelli, P., Vasudevan, R. & Howe, C. J. Photosynthetic, respiratory and extracellular electron transport pathways in cyanobacteria. *Biochimica et Biophysica Acta (BBA)-Bioenergetics* **1857**, 247-255 (2016).

2 Saar, K. L. *et al.* Enhancing power density of biophotovoltaics by decoupling storage and power delivery. *Nature Energy* **3**, 75 (2018).

3 Min Jung Kim, Seoung Jai Bai, Jae Ryoun Youn & Young Seok Song. Anomalous power enhancement of biophotovoltaic cell. *Journal of Power Sources* **412**, 201-310, doi:10.1016/j.jpowsour.2018.11.056 (2019).

4 Bombelli, P. *et al.* Surface morphology and surface energy of anode materials influence power outputs in a multi-channel mediatorless bio-photovoltaic (BPV) system. *Physical Chemistry Chemical Physics* **14**, 12221-12229 (2012).

5 Bombelli, P., Müller, T., Herling, T. W., Howe, C. J. & Knowles, T. P. A High Power-Density, Mediator-Free, Microfluidic Biophotovoltaic Device for Cyanobacterial Cells. *Advanced energy materials* **5**, 1401299 (2015).

6 Sekar, N., Umasankar, Y. & Ramasamy, R. P. Photocurrent generation by immobilized cyanobacteria via direct electron transport in photo-bioelectrochemical cells. *Physical Chemistry Chemical Physics* **16**, 7862-7871 (2014).

7 Qian, F. *et al.* Photoenhanced electrochemical interaction between Shewanella and a hematite nanowire photoanode. *Nano letters* **14**, 3688-3693 (2014).

8 Ooms, M. D., Jeyaram, Y. & Sinton, D. Wavelength-selective plasmonics for enhanced cultivation of microalgae. *Applied Physics Letters* **106**, 063902 (2015).

9 Eroglu, E., Eggers, P. K., Winslade, M., Smith, S. M. & Raston, C. L. Enhanced accumulation of microalgal pigments using metal nanoparticle solutions as light filtering devices. *Green Chemistry* **15**, 3155-3159 (2013).

10 Amrei, H. D., Ranjbar, R., Rastegar, S., Nasernejad, B. & Nejadebrahim, A. Using fluorescent material for enhancing microalgae growth rate in photobioreactors. *Journal of applied phycology* **27**, 67-74 (2015).

11 Zhang, N., Han, C., Fu, X. & Xu, Y.-J. Function-Oriented Engineering of Metal-

Based Nanohybrids for Photoredox Catalysis: Exerting Plasmonic Effect and Beyond. *Chem* (2018).

12 Gao, R. *et al.* A ZnO nanorod layer with a superior light-scattering effect for dye-sensitized solar cells. *RSC Advances* **3**, 18537-18543 (2013).

13 Strano, V. *et al.* Low-cost high-haze films based on ZnO nanorods for light scattering in thin c-Si solar cells. *Applied Physics Letters* **106**, 013901 (2015).

14 Ty, J. T. D. & Yanagi, H. Electrochemical deposition of zinc oxide nanorods for hybrid solar cells. *Japanese Journal of Applied Physics* **54**, 04DK05 (2015).

15 Clavero, C. Plasmon-induced hot-electron generation at nanoparticle/metal-oxide interfaces for photovoltaic and photocatalytic devices. *Nature Photonics* **8**, 95 (2014).

16 Mubeen, S. *et al.* On the plasmonic photovoltaic. *ACS nano* **8**, 6066-6073 (2014).

17 Wu, M. *et al.* In situ growth of matchlike ZnO/Au plasmonic heterostructure for enhanced photoelectrochemical water splitting. *ACS applied materials & interfaces* **6**, 15052-15060 (2014).

18 Kim, H. M., Youn, J. R. & Song, Y. S. Hydrodynamic fabrication of structurally gradient ZnO nanorods. *Nanotechnology* **27**, 085704 (2016).

19 Roxworthy, B. J., Bhuiya, A. M., Vanka, S. P. & Toussaint Jr, K. C. Understanding and controlling plasmon-induced convection. *Nature communications* **5**, 3173 (2014).

20 Perumal, V. *et al.* 'Spotted Nanoflowers': Gold-seeded Zinc Oxide Nanohybrid for Selective Bio-capture. *Scientific reports* **5**, 12231 (2015).

21 Guo, J. *et al.* High-performance gas sensor based on ZnO nanowires functionalized by Au nanoparticles. *Sensors and Actuators B: Chemical* **199**, 339-345 (2014).

22 Kahraman, S. *et al.* Characteristics of ZnO thin films doped by various elements. *Journal of Crystal Growth* **363**, 86-92 (2013).

23 Wang, X. *et al.* Facile synthesis and optical properties of polymer-laced ZnO-Au hybrid nanoparticles. *Nanoscale research letters* **9**, 109 (2014).

24 Kang, Z. *et al.* Self-powered photoelectrochemical biosensing platform based on Au NPs@ ZnO nanorods array. *Nano Research* **9**, 344-352 (2016).

25 Kang, Z. *et al.* Electronic structure engineering of Cu 2 O film/ZnO nanorods array all-oxide pn heterostructure for enhanced photoelectrochemical property and self-powered biosensing application. *Scientific reports* **5**, 7882 (2015).

26 Wang, M. *et al.* p–n Heterojunction photoelectrodes composed of Cu 2 O-loaded TiO 2 nanotube arrays with enhanced photoelectrochemical and photoelectrocatalytic activities. *Energy & Environmental Science* **6**, 1211-1220 (2013).

27 Jia, C. *et al.* Interface-Engineered Plasmonics in Metal/Semiconductor Heterostructures. *Advanced Energy Materials* **6**, 1600431 (2016).

28 Reineck, P., Brick, D., Mulvaney, P. & Bach, U. Plasmonic hot electron solar cells: the effect of nanoparticle size on quantum efficiency. *The journal of physical chemistry letters* **7**, 4137-4141 (2016).

29 Bora, T., Kyaw, H. H., Sarkar, S., Pal, S. K. & Dutta, J. Highly efficient ZnO/Au Schottky barrier dye-sensitized solar cells: Role of gold nanoparticles on the charge-transfer process. *Beilstein journal of nanotechnology* **2**, 681 (2011).

30 Cushing, S. K. & Wu, N. Plasmon-enhanced solar energy harvesting. *The Electrochemical Society Interface* **22**, 63-67 (2013).

31 Tatsuma, T., Nishi, H. & Ishida, T. Plasmon-induced charge separation: chemistry and wide applications. *Chemical science* **8**, 3325-3337 (2017).

32 Wu, L., Kim, G. M., Nishi, H. & Tatsuma, T. Plasmonic Photovoltaic Cells with Dual-Functional Gold, Silver, and Copper Half-Shell Arrays. *Langmuir* **33**, 8976-8981 (2017).

33 Bottin, H. & Lagoutte, B. Ferrodoxin and flavodoxin from the cyanobacterium Synechocystis sp PCC 6803. *Biochimica et Biophysica Acta (BBA)-Bioenergetics* **1101**, 48-56 (1992).

Korean Abstract

광유체역학은 광학과 미세유체역학을 기반으로 한 학문으로써 각 분야의 장점 및 특징을 유기적으로 활용해 광학요소 및 유체시스템을 보다 유연하게 구성할 수 있는 장점을 가지고 있다. 즉, 미세유체시스템을 이용해 광학기능을 하는 요소를 다양하게 구현하거나 광학시스템과 결합된 미세유체시스템 내에서 극소량의 유체 및 유체 기반 샘플을 조작하고 처리하는 것을 가능하게 한다. 예를 들어, 변형이 가능한 유체는 마이크로 렌즈, 도파관 등과 같은 광학 시스템을 쉽게 재구성할 수 있게 하는 장점을 가지고 있는데, 이는 단순히 서로 다른 성질을 가진 유체 물질로 변경하거나 또는 유체의 계면 모양을 변형시킴으로써 가능하다. 한편, 광학 시스템에 연결된 미세유체 시스템은 극소량의 샘플만을 이용해 효율적인 분석을 할 수 있게 하는 편리한 기반을 제공한다. 이러한 관점에서 광유체역학 활용을 위한 연구가 활발히 진행되고 있고, 이 시스템을 이용한 다양한 광학 요소 구성, 생물학적 분석, 에너지 하베스팅, 화학적 센싱 등의 응용들이 많이 제안되었다.

본 논문의 2장에서는 기체-액체 계면의 형태를 수력학적으로 조절함으로써 광유체역학 기반 다초점 마이크로 렌즈를 구현하였다. 또한 렌즈의 특성을 결정하는 기체-액체 계면 형성과 관련된 물리적 현상을 수치해석 및 이론적 분석을 통해 조사하였다. 안정된 다상 계면을 형성시키기 위해 관련 이론을 이해하는 것은 본 연구에서 제안하는 마이크로 렌즈 구축에 있어서 매우 중요한 요소였다. 결론적으로 기체-액체 계면에서의 비선형적 표면장력효과가 렌즈 모양에 많은 영향을 미치는 것을 알 수 있었고, 이 표면장력 효과는 렌즈를 구성하기 위해 사용한 유체의 성질에 의해 결정되었다. 뿐만 아니라 제안된 마이크로 렌즈는 기체와 액체 계면에 기반하고 있으므로, 이 두 유체의 큰 굴절률 차이를 활용해 액체-액체 기반 마이크로 렌즈와 비교하여 상대적으로 짧은 초점 거리를 형성시킬 수 있다는 장점을 지니고 있다. 이와 같이 짧은 초점 거리를 형성하는 마이크로 렌즈는 앞으로 나아가 더욱 소형화된 광유체역학 시스템을 구현하는데 있어 기여를 할 수 있을 것으로 기대된다.

3장에서는 금속-유전물질로 이루어진 하이브리드 플라즈모닉 기판을 설계하고 제작함으로써 향상된 플라즈모닉 집게를 제안하였다. 실험적으로는 폴리스타이렌 입자와 E.coli 세포를 잡고 조작해보았다. 이 시스템에서 플라즈모닉 집게의 성능을 향상시키기 위해 국소표면플라즈몬공명현상 (LSPR)을 활용하였는데, 이는 국소 표면의 근접장의 에너지를 증폭시키기 위한 도구로서 많은 관심을 받고 있는 광학적 현상이다. 본 연구에서는 이 LSPR현상에 의해 유도된 열발생 효과를 이용해 효율적으로 입자 및 세포를 잡는 미세 광유체 시스템을 구현하였다. 또한 궁극적으로 이 시스템의 효율을 높인 하이브리드 플라즈모닉 구조체의 시너지 효과를 분석 및 입증하기 위해 수치해석 및 실험적 분석을 진행했다. 하이브리드 구조체 도입은 금나노 입자의 LSPR 현상을 더 강화시키기 위한 것이었고, 단순히 아연 산화물 나노막대기와 결합된 금나노 입자 구조체를 제작함으로써 향상된 결과를 얻을 수 있었다. 결론적으로, 아연산화물 나노막대기가 입사된 빛보다 더 증폭된 빛을 표면에 부착된 금 나노입자에 전달하는 역할을 하였고 그 결과로 플라즈모닉 집게의 성능을 월등히 증가시켜주었다. 이와 같이 향상된 플라즈모닉 기판 제안과 그 배경에 대한 심도 깊은 분석은 앞으로 광유체 시스템에 기반한 효율적인 생화학적 분석 플랫폼을 구축하는데 있어서 많은 도움을 줄 수 있을 것으로 예상된다.

4장에서는 플라즈모닉 현상에 의해 향상된 빛 에너지 하베스팅 시스템을 구현하였는데, 이를 위해 하이브리드 플라즈모닉 광전극을 본 연구에서 구현한 바이오 기반 광전지 시스템의 음극으로 활용하였다. 해당 시스템에서 태양에너지 전환은 Synechocystis sp. 세포의 광합성 현상과 하이브리드 플라즈모닉 음극 (ZnONRs/AuNPs) 구조체의 광여기, 광산란 그리고 플라즈모닉 현상에 기초한다. 또한 본 시스템은 전기 생산을 위해 매우 소량의 세포 용액(수마이크로 리터)을 필요로 한다. 뿐만 아니라 사용된 플라즈모닉 음극은 광원의 넓은 스펙트럼 영역에서 빛 에너지 하베스팅을 가능하게 하는데, 이는 플라즈모닉 구조체가 LSPR에 의해 유도된 현상으로 인해 자체적으로 전자를 생성할 뿐만 아니라 세포의 광합성 활동을 훨씬 더 향상시켜주는 것으로부터 기여된다. 결과적으로 플라즈모닉 현상에 의해 향상된 바이오 기반 광전지 시

스템을 이용했을 때 획기적인 파워 향상을 얻을 수 있었으며, 음극으로 단순히 ITO glass를 사용한 시스템과 비교했을 때 약 17.3 배에 해당하는 파워를 얻었다. 이러한 관점에서 본 연구에서 제안된 플라즈모닉 음극 플랫폼은 앞으로 광유체 시스템에 기반한 효율적인 에너지 하베스팅 시스템을 구현하는데 있어 기여할 수 있을 것으로 기대된다.

주요어: 광유체역학, 미세유체역학, 플라즈모닉스, 국소표면플라즈몬공명, 다초점 마이크로렌즈, 플라즈모닉 집게, 플라즈모닉 음극, 수치해석

학번: 2014-21429